

NORTHWESTERN UNIVERSITY

Imaging Small, Discrete Scatterers Through Aberrating Media Using DORT with
Synthetic Wavelengths

A THESIS

SUBMITTED TO THE GRADUATE SCHOOL
IN PARTIAL FULFILLMENT OF THE REQUIREMENTS

for the degree

MASTER OF SCIENCE

Electrical Engineering

By

Michael Joseph S. Lee

EVANSTON, ILLINOIS

September 2023

Abstract

The ability to image through aberrating or scattering media is a useful ability. However, doing so is a challenging task. The presence of scattering and/or some other form of aberration can distort images, making it difficult to ascertain what is behind the aberrating medium. Furthermore, one might only have limited knowledge of the aberrating medium, which makes the task even harder. The problem of imaging through aberrating medium is, in essence, an inverse problem: given some set of measurements, ascertain how scatterers of electromagnetic radiation are arranged in or behind an aberrating medium.

In this thesis, two techniques/ideas are used together in order to image small, discrete scatterers behind an aberrating medium. The first is the DORT technique, a technique that utilizes the singular value decomposition of a transfer (e.g. transmission) matrix and where numerical backpropagation can be utilized to perform imaging. The second is the idea of synthetic wavelengths, which allows one to effectively use a longer wavelength, thus mitigating the effects of certain aberrations. Simulated experimental results from MATLAB experiments and a modified version of the Holotorch library, a Fourier optics library, are given to support the proposed imaging method.

Additionally, this thesis derives, in detail, a set of equations for describing the results of performing DORT. For the case of taking the singular value decomposition of a transfer matrix, these equations are more general and complete than what is found in certain pieces of existing literature.

Acknowledgments

Throughout my time in graduate school and before, many people have had a positive impact on me. Friends, mentors, professors, acquaintances, and others have all affected me for the better. As my memory is imperfect, I cannot possibly acknowledge everyone explicitly—and some people and entities are part of my private life and shall remain unlisted. Regardless, there are a number of people whom I would like to explicitly thank. In no particular order, I shall list these people.

I would like to thank Dr. Oliver Strides Cossairt for advising me. He gave guidance on what to pursue as I was working on my research project and gave me advice at times. I would also like to thank Dr. Jack Tumblin for his words of support as I was writing my thesis. Writing my thesis was not easy for me, and his kind words were helpful. Additionally, I am thankful to Dr. Florian Willomitzer, who helped develop the idea of synthetic wavelengths, an idea which I used in my thesis. I am thankful to Dr. Emma Alexander, who has given me advice on multiple occasions. Furthermore, I am thankful to Dr. Alan Varteres Sahakian, who has been supportive of me throughout my time at Northwestern.

I am also thankful to Jipeng Sun for being a peer mentor to me. He wrote a conference paper with me—the aforementioned conference paper is given in Appendix D—and gave me advice when it came to writing my thesis. Jipeng gave me guidance and generally looked out for me. He also introduced me to and helped me network with other graduate students.

I am thankful to my committee members: Dr. Oliver Strides Cossairt, Dr. Jack Tumblin, Dr. Florian Willomitzer, Dr. Emma Alexander, and Dr. Alan Varteres Sahakian. Being

on a thesis committee takes time and effort, and I am appreciative that the members of my committee were willing to give me that time and effort.

I would also like to thank all those who have provided support to me during my time in graduate school whom I have not mentioned. Various people have provided their support to me in various ways, both big and small. I am thankful to these unnamed people.

More broadly, I am thankful to all those who have had a positive impact on me. Whether it be a friendly conversation, an opportune smile, or some other positive action towards me, I am appreciative.

Finally, I am thankful to my mother who supported me throughout my life and all throughout graduate school. I am not sure where I would be without her. Her positive influence and support for me is much appreciated!

Preface

This thesis documents the work that I, Michael Joseph S. Lee, did during the 2022-2023 school year for my master's degree in electrical engineering. This work is primarily in the realm of optics and computational optics. The focus of this work is imaging through aberrating media using the DORT technique augmented with synthetic wavelengths.

List of Abbreviations

DORT Decomposition of the time-reversal operator (a technique)

SLM Spatial light modulator

SVD Singular value decomposition

List of Symbols

$\mathbf{H}(\lambda)$	The transfer matrix
$\mathbf{U}(\lambda)$	The \mathbf{U} matrix obtained from taking the singular value decomposition of $\mathbf{H}(\lambda)$
$\mathbf{\Sigma}(\lambda)$	The $\mathbf{\Sigma}$ matrix obtained from taking the singular value decomposition of $\mathbf{H}(\lambda)$
$\mathbf{V}(\lambda)$	The \mathbf{V} matrix obtained from taking the singular value decomposition of $\mathbf{V}(\lambda)$
$\mathbf{F}(\lambda)$	A matrix describing propagation from transmitting transducers to scatterers
$\mathbf{S}(\lambda)$	A matrix describing scattering off of scatterers
$\mathbf{B}(\lambda)$	A matrix describing propagation from scatterers to receiving transducers
$G(\vec{\mathbf{r}}, \vec{\mathbf{r}}_{source}; \omega)$	Green's function with observation point $\vec{\mathbf{r}}$ and source point $\vec{\mathbf{r}}_{source}$ (function of ω)
$G(\vec{\mathbf{r}}, \vec{\mathbf{r}}_{source}; \lambda)$	Green's function with observation point $\vec{\mathbf{r}}$ and source point $\vec{\mathbf{r}}_{source}$ (function of λ)
k	Wavenumber
n	Refractive index
Λ	Synthetic wavelength
λ	Wavelength in free space
ω	Angular frequency

Glossary

backpropagation Replying or retransmitting fields.

DORT A technique that gives data that can be used to image and/or selectively focus on scatterers.

eigenstructure demixing See Section 3.5 for this definition.

eigenstructure mixing See Section 3.5 for this definition.

Green's function An impulse response for a linear differential operator.

ideally-resolved See Section 3.4 for this definition.

numerical backpropagation Replying or retransmitting fields in computation or simulation.

transfer matrix A matrix relating a set of transmitted signals to a set of received signals in the frequency domain.

well-resolved See Section 3.4 for this definition.

To my mother, who loved and supported me all throughout
my graduate school journey.

Table of Contents

Abstract	iii
Acknowledgments	v
Preface	vii
List of Abbreviations	ix
List of Symbols	xi
Glossary	xiii
Dedication	xiv
Table of Contents	xv
List of Figures	xx
List of Tables	xxii
Online Availability	xxiii
1 Introduction	1
1.1 Introductory remarks	1
1.2 Existing work	2
1.3 Contributions	3

1.4 Notation	3
1.5 Outline of this thesis	4
2 General Background	5
2.1 Introduction	5
2.2 Phase retrieval	5
2.3 Transfer matrices	6
2.3.1 Introduction and definition	6
2.3.2 Measuring transfer matrices in the optical domain	8
3 DORT Background	13
3.1 Introduction	13
3.2 A quick demonstration of DORT	15
3.3 Transfer matrix model assumed by DORT	18
3.4 Ideally-resolved and well-resolved assumptions	20
3.5 Eigenstructure mixing and demixing	24
4 DORT Equations	27
5 Synthetic Wavelengths Background	31
6 DORT and Synthetic Wavelengths Investigation	35
6.1 Introduction	35
6.2 Main idea and conclusions	35
6.3 DORT and synthetic wavelengths derivation	37
6.3.1 Defining a DORT model	37
6.3.2 Obtaining synthetic singular vectors	40
6.3.3 Backpropagating synthetic singular vectors	42
7 MATLAB Simulations	47

7.1	Introduction	47
7.2	Outline of the chapter	47
7.3	Assumptions behind the simulations	48
7.4	Computing the transfer matrix	49
7.5	Performing DORT	51
7.6	Backpropagating fields	52
7.6.1	Backpropagating arbitrary fields	52
7.6.2	DORT and backpropagation	53
7.6.3	Backpropagating at synthetic wavelengths	54
7.7	Imaging experiment with DORT at single wavelengths	55
7.8	Imaging experiment with DORT and synthetic wavelengths	59
7.9	Aberrated path length imaging experiment	61
7.10	A note on eigenstructure mixing	64
7.11	Summary and observations	65
8	Imaging Through Aberrating Media Simulation	67
8.1	Introduction	67
8.2	Outline of the chapter	68
8.3	Holotorch model used when obtaining the transfer matrix	68
8.3.1	Optical system overview	68
8.3.2	Optical system model details	69
8.4	More information on various model components	77
8.4.1	Aberrating layer model	77
8.4.2	Discussion on the aberrating layer model	79
8.4.3	Scatterer model	80
8.4.4	Discussion on the scatterer model	81
8.5	Measuring the transfer matrix in simulation	81
8.6	Holotorch DORT experiments	84

8.6.1	Non-synthetic wavelength case	84
8.6.2	Synthetic wavelengths case	88
8.6.3	Some additional comments	93
8.7	Simulation limitations	96
8.8	Other potential limitations	97
8.9	Summary and observations	99
9	Conclusion and Future Work	101
9.1	Conclusion	101
9.2	Future work	102
References		105
A	Miscellaneous Appendix Sections	111
A.1	Green's function for the Helmholtz equation	111
A.2	Fields resulting from transmitting from transmitters	112
B	Derivation of the DORT Equations	115
B.1	Derivation assumptions	115
B.1.1	Basic assumptions	115
B.1.2	An additional assumption	116
B.2	Rewriting various matrices/matrix products in different forms	117
B.2.1	Part 1	118
B.2.2	Part 2	119
B.3	Some setup	123
B.3.1	Eigenvalues and eigenvectors for matrices	123
B.3.2	Relating singular values to eigenvalues	125
B.4	Deriving expressions for the singular vectors	126
B.4.1	Deriving an expression for the right-singular vectors	126

B.4.2	Deriving an expression for the left-singular vectors	129
B.4.3	Equation validity in terms of singular values	130
B.5	Deriving an expression for the singular values	131
B.5.1	Case 1	133
B.5.2	Case 2	134
B.5.3	Combining cases	135
B.6	Obtaining constraints on singular vector phase terms	136
B.7	Summary of results	138
C	Theorems and Proofs	141
D	COSI Conference Paper	147
Vita		151

List of Figures

2.1	Transfer matrix illustration	8
2.2	General setup for recovering a transmission (transfer) matrix	10
3.1	Imaging scatterers in the near-field with DORT and backpropagation . . .	16
3.2	Detecting scatterers in the far-field with DORT and backpropagation . . .	17
3.3	The transfer matrix \mathbf{H} decomposed into a product of three matrices	19
7.1	Selective focusing on scatterers with DORT at a non-synthetic wavelength ($\lambda = 1200 \text{ nm}$)	57
7.2	Selective focusing on scatterers with DORT at a non-synthetic wavelength ($\lambda \approx 1214.57 \text{ nm}$)	58
7.3	Selective focusing on scatterers with DORT using a synthetic wavelength ($\Lambda = 0.10 \text{ mm}$)	60
7.4	Demonstration showing how backpropagating singular vectors from DORT can fail to create images in the presence of path length variations	62
7.5	Demonstration showing how backpropagating synthetic singular vectors from DORT can create images despite path length variations	63
8.1	Simulated experimental setup used for measuring the transfer matrix used in Chapter 8	69
8.2	Block diagram of the simulated system in Holotorch	70
8.3	Random thickness screen model from Section 7.1.1 of [5]	77
8.4	SLM output patterns from right-singular vectors	83
8.5	Diagram illustrating backpropagation to the scatterer plane	86
8.6	Block diagram of non-synthetic wavelength backpropagation	87
8.7	Scatterer plane fields from backpropagated right-singular vectors (non-synthetic wavelength case)	87
8.8	Field maximums in plots in Figure 8.7	88
8.9	Block diagram of synthetic wavelength backpropagation	90
8.10	Diagram illustrating synthetic field generation and synthetic field backpropagation	91
8.11	Synthetic fields before backpropagation	91
8.12	Scatterer plane fields from backpropagated right-singular vectors (synthetic wavelength case)	92
8.13	Field maximums in plots in Figure 8.12	92

8.14 Results of backpropagating non-synthetic singular vectors with the aberrating layer being modeled	95
--	----

List of Tables

1	Items and corresponding code locations	xxv
---	--	-----

Online Availability

The code used in this thesis has been made publicly available. See <https://github.com/mich-lee/michael-joseph-s-lee-ms-thesis> for the code.^{1,2} Read the `README.md` file in the root of that repository for more information on the code. Additionally, a copy of this thesis, the accompanying thesis defense presentation, and the conference presentation for the accepted conference paper given in Appendix Section D are available online in the repository at <https://github.com/mich-lee/michael-joseph-s-lee-ms-thesis>. Read the `README.md` file in the root of that repository for more information on the copy of this thesis, the accompanying thesis defense presentation, and the conference presentation.³

The work in this thesis makes use of a modified version [1] of the Holotorch library [2], which is a Fourier optics library. The Holotorch library can be found at <https://github.com/facebookresearch/holotorch>. The modified version of Holotorch was forked from Commit cf1a80b3172684520b266cf03f9ba0163b5c1826 in Holotorch. This commit can be found at <https://github.com/facebookresearch/holotorch/commit/cf1a80b3172684520b266cf03f9ba0163b5c1826>. The modified version of Holotorch can be

¹Specifically, the code used for the demonstrations in Section 3.2 and the experiments in Chapters 7 and 8 is published online.

²This is covered in the `README.md` file of the repository at <https://github.com/mich-lee/michael-joseph-s-lee-ms-thesis>, but it may be worth mentioning that the code is actually spread out over three repositories: <https://github.com/mich-lee/michael-joseph-s-lee-ms-thesis>, <https://github.com/mich-lee/SW-DORT-Research-Code>, and <https://github.com/mich-lee/holofork>. See the aforementioned `README.md` at the root of the repository at <https://github.com/mich-lee/michael-joseph-s-lee-ms-thesis> for more information.

³This is covered in the `README.md` file of the repository at <https://github.com/mich-lee/michael-joseph-s-lee-ms-thesis>, but it may be worth mentioning that exact transcripts of what was said during the thesis defense presentation and conference presentation can be found in the presenter's notes in the corresponding PowerPoint presentations in the aforementioned GitHub repository.

found at <https://github.com/mich-lee/holofork> .

Table 1 on page xxv lists various parts of this thesis and the locations of the corresponding code. The locations refer to locations in GitHub repositories. Locations starting with `michael-joseph-s-lee-ms-thesis/` refer to items in the repository at <https://github.com/mich-lee/michael-joseph-s-lee-ms-thesis> , and locations starting with `SW-DORT-Research-Code/` refer to items in the repository at <https://github.com/mich-lee/SW-DORT-Research-Code> . Note that the code listed under Sections 8.3, 8.4, 8.5, and 8.6 in Table 1 (given below) requires other code to run, which can be found in the repositories at <https://github.com/mich-lee/SW-DORT-Research-Code> and <https://github.com/mich-lee/holofork> .

Item	Location
Figure 3.1	michael-joseph-s-lee-ms-thesis/Code/DORT_Background/ DORT_Focusing_Demo_Near_Field.m
Figure 3.2	michael-joseph-s-lee-ms-thesis/Code/DORT_Background/ DORT_Focusing_Demo_Far_Field.m
Figure 7.1	michael-joseph-s-lee-ms-thesis/Code/MATLAB_Simulations/ DORT_Single_Wavelength_Focusing_1.m
Figure 7.2	michael-joseph-s-lee-ms-thesis/Code/MATLAB_Simulations/ DORT_Single_Wavelength_Focusing_2.m
Figure 7.3	michael-joseph-s-lee-ms-thesis/Code/MATLAB_Simulations/ DORT_Synthetic_Wavelength_Focusing.m
Figure 7.4a	michael-joseph-s-lee-ms-thesis/Code/MATLAB_Simulations/ DORT_Path_Length_Aberration_Test_Single_Wavelength_1.m
Figure 7.4b	michael-joseph-s-lee-ms-thesis/Code/MATLAB_Simulations/ DORT_Path_Length_Aberration_Test_Single_Wavelength_2.m
Figure 7.5	michael-joseph-s-lee-ms-thesis/Code/MATLAB_Simulations/ DORT_Path_Length_Aberration_Test_Synthetic_Wavelength.m
Sections 8.3, 8.4, and 8.5	SW-DORT-Research-Code/THESIS EXPERIMENTS/ Generate_Data (aberrating layer 7mm in front of scatterer plane).py Additional Code: SW-DORT-Research-Code/ScattererModel.py SW-DORT-Research-Code/TransferMatrixProcessor.py SW-DORT-Research-Code/WavefrontAberrator.py
Section 8.6	SW-DORT-Research-Code/THESIS EXPERIMENTS/ Analyze_Data (THESIS).py

Table 1: Items and corresponding code locations

Chapter 1

Introduction

1.1 Introductory remarks

In the real world, that which we wish to see is sometimes hidden behind a translucent obstruction. However, ascertaining what is behind a translucent obstruction is a difficult task; light may pass through such an obstruction, but it gets aberrated in the process. For example, objects on the other side of frosted glass appear blurry and diffuse, making it difficult to clearly see what is on the other side. Moreover, in the medical realm, biological tissue—which is translucent at certain wavelengths—scatters light, making it difficult to see deep inside tissue [6].

Seeing through translucent obstructions, or in general, through aberrating media, is undoubtedly not a straightforward task. Yet, various methods exist for doing so. Some methods isolate single-scattered or ballistic light in order to accomplish this task [6]. Another method relies on a concept known as “synthetic wavelengths” to effectively work with longer wavelengths, thus allowing one to image through scattering media [7].

This thesis focuses on imaging small, discrete scatterers behind aberrating media using a combination of the DORT technique and synthetic wavelengths. The DORT technique involves taking the singular value decomposition (SVD) of a transfer (e.g. transmission)

matrix. The singular vectors from the SVD define fields that can be numerically backpropagated. If one has a model of one's system, including the aberrating medium, these numerically backpropagated fields will, under certain circumstances, focus in on individual scatterers. However, this requires that one have an explicit model of the aberrating medium, which one might not have.

Synthetic wavelengths are used to allow for focusing behavior in backpropagation without needing an explicit model of the aberrating medium. Fields obtained from the singular vectors that came from DORT are used to define a synthetic field that can be backpropagated. The use of synthetic wavelengths allows one to ignore the aberrating medium and pretend that it is free space.

Ultimately, this thesis presents a way to image small, discrete scatterers behind an aberrating medium that does not require one to have an explicit model of the aberrating medium. Additionally, this thesis also provides evidence for the efficacy of combining DORT and synthetic wavelengths in general. Experimental evidence is given in the form of MATLAB simulations and a simulated experiment using a modified version [1] of the Holotorch library [2], a Fourier optics library.¹

This thesis also gives a set of equations for describing the results of performing DORT, along with a detailed derivation. Previous pieces of literature, such as [3] and [4], give similar equations which are not as general or complete for the case of taking the singular value decomposition of a transfer matrix.

1.2 Existing work

The problem of optical imaging through aberrating media is a problem that has been explored extensively prior to this thesis. [6] gives a review of various optical imaging techniques that have been used to image through complex scattering media. A number of techniques

¹See “[Online Availability](#)” near the beginning of this thesis for more information on Holotorch and the modified version of the Holotorch library.

described in [6] involve isolating single-scattered or ballistic light from multiple-scattered light.

Of particular relevance to this thesis, however, is work that utilized DORT to optically image through aberrating media. This was done in [8] and [9]. In those works, a “reflection matrix” corresponding to single scattering was obtained, and DORT was performed using said matrix. The information from DORT was used to obtain images of beads behind a scattering medium. Also relevant to this thesis is some of the work pertaining to synthetic wavelengths. Synthetic wavelengths have been used to image through aberrating media, revealing objects which were previously obscured [7].

1.3 Contributions

This thesis makes a couple of contributions. It proposes a new² imaging technique that combines the DORT technique and the concept of synthetic wavelengths. This imaging technique can be used to image small, discrete scatterers which may or may not be located behind an aberrating medium. This thesis also gives a set of equations (Equations B.24, B.26, B.35, and B.38) that describe the results of performing DORT. These equations are more general and complete than those in some existing literature, such as [3] and [4].

1.4 Notation

This thesis uses certain notation and conventions. This section (Section 1.4) will go over some of the notation and conventions used.

Complex conjugation is denoted as $(\dots)^*$, matrix transposition is denoted as $(\dots)^\top$, and conjugate transposition for matrices is denoted as $(\dots)^\dagger$. Matrices and vectors are denoted by bold letters, and scalars are denoted by regular (non-bold) letters. Given a matrix \mathbf{M} , $M_{i,j}$ denotes the component of \mathbf{M} in the i^{th} row and j^{th} column of \mathbf{M} , $\mathbf{M}_{i,*}$ denotes a row

²“New” as far as the author of this thesis is aware.

vector made from the i^{th} row of \mathbf{M} , and $\mathbf{M}_{*,j}$ denotes a column vector made from the j^{th} column of \mathbf{M} . Standard basis (column) vectors are denoted as $\hat{\mathbf{e}}_i$. Finally, the complex inner product/complex dot product for finite-dimensional vectors is taken to be conjugate linear in its ***second*** argument and is defined as

$$\langle \vec{\mathbf{a}}, \vec{\mathbf{b}} \rangle = \vec{\mathbf{a}} \cdot \vec{\mathbf{b}} = \sum_{i=1}^N a_i b_i^*, \quad (1.1)$$

where $\vec{\mathbf{a}}$ and $\vec{\mathbf{b}}$ are N -dimensional complex vectors.

1.5 Outline of this thesis

This thesis is organized into chapters. Chapter 1 provides an introduction to this thesis. Then, Chapter 2 provides general background information. Afterwards, Chapter 3 provides background information on the DORT technique. Chapter 4 details a set of equations that describe the results of performing DORT under certain conditions. An overview of synthetic wavelengths is given in Chapter 5.

Chapter 6 theoretically investigates combining synthetic wavelengths and DORT. MATLAB experiments pertaining to DORT and synthetic wavelengths combined with DORT are detailed in Chapter 7. A Holotorch experiment pertaining to imaging through an aberrating medium with DORT, with and without synthetic wavelengths, is detailed in Chapter 8. Chapter 9 gives a conclusion and describes future work that could be done.

Appendix A contains miscellaneous appendix sections. A proof for/derivation of the equations in Chapter 4 is given in Appendix B. Various theorems and proofs are given in Appendix C. Finally, a paper accepted to the Computational Optical Sensing and Imaging (COSI) 2023 conference is given in Appendix D.

Chapter 2

General Background

2.1 Introduction

This chapter (Chapter 2) gives some general background. Specifically, it gives general background on phase retrieval and transfer matrices.

2.2 Phase retrieval

Being able to sample a waveform allows one to recover the phases of the waveform's various signal components via a discrete Fourier transform (DFT). Such sampling is possible with acoustic signals as well as RF/microwave signals, and hardware exists for this purpose.¹ However, for optical frequencies, measuring phase becomes more complicated. Optical frequencies are too high to be sampled directly, meaning that directly measuring an optical waveform is not viable. Interferometry can be used to measure the phase of monochromatic light, but doing so requires a reference arm/phase reference and the process can be sensitive to vibrations.

Moreover, the most readily available light sensors only measure the average intensity of light. With such hardware, for monochromatic light, one can directly measure the amplitude

¹In the case of RF, one might first demodulate a signal down to baseband and then sample.

of the incident field using intensity measurements, but phase cannot be measured. This is sometimes suboptimal as it is sometimes desirable to measure phase.

It turns out the loss of phase information after physical measurements has a name: the phase problem. This problem occurs in the field of X-ray crystallography and when measuring light. The task of solving this problem—i.e. obtaining phase/complex phasors from amplitude measurements—is known as phase retrieval. One way of mathematically describing the phase retrieval problem is as follows [10]:

$$\text{Given an known observation } \vec{y}, \text{ where } \vec{y} = |\mathbf{A}\vec{x}| \text{ and } \mathbf{A} \text{ is known, find } \vec{x}. \quad (2.1)$$

This equation expresses a general form that the phase retrieval problem may take. Solving problems of this form has applications in computational optics, and this problem formulation can be seen in works such as [10], [11], and [12]. There are a multitude of phase retrieval algorithms, and an overview of phase retrieval algorithms can be found in [10].

2.3 Transfer matrices

2.3.1 Introduction and definition

Suppose one had a set of transmitting transducers and a set of receiving transducers. There are many different types of transducers: piezoelectric elements that produce and receive sound waves, antennas that transmit and receive electromagnetic waves, spatial light modulators that modulate the amplitude and/or phase of incident light, camera sensors that measure light intensity, et cetera. One might ask if one can come up with a way to relate the transmitted signals from the transmitting transducers to either the signals directly received

by the receiving transducers, or the signals/fields incident upon them.² It turns out that the answer is oftentimes “yes”.

For linear media subject to a (linear) wave equation, one can come up with Green’s functions that relate the fields at a source point to those at an observation point. This effectively means that one can come up with (frequency domain) transfer functions between transmitting and receiving transducers. These transfer functions relate transmitted signals to those incident on the receivers. Additionally, assuming that the principle of superposition holds³, one can express the signals incident on the receivers as linear combinations of the transmitted signals. In matrix form, this can be expressed as

$$\vec{\mathbf{Y}}(\lambda) = \mathbf{H}(\lambda) \vec{\mathbf{X}}(\lambda) \quad (2.2)$$

where $\vec{\mathbf{Y}}(\lambda)$ is a vector of fields incident on the receivers, $\vec{\mathbf{X}}(\lambda)$ is a vector of transmitted signals, and $\mathbf{H}(\lambda)$ is a transfer matrix that relates the two aforementioned vectors. The component $H_{ij}(\lambda)$ relates the j^{th} transmitted field to the field incident on the i^{th} receiving element—in other words, $H_{ij}(\lambda)$ is the transfer function going from the position of the j^{th} transmitting transducer to the position of the i^{th} receiving transducer.

Figure 2.1 provides an illustration for a case/setup that may occur when working in optics/light. In that figure, the transmitting transducers are controllable segments on a spatial light modulator (SLM) and the receiving transducers are pixels on a camera sensor. The fields at the SLM output, i.e. the fields in the SLM plane, are related to the fields incident on⁴ the camera sensor, i.e. the fields in the sensor plane, by the (frequency domain)

²Note that one can make a distinction between the signals fed to the transmitting transducers and the signals that are ultimately transmitted into the medium—for example, the frequency response of a transmitting transducer can cause these signals to be different. One can also make a distinction between the signals incident on the receiving transducers and the signals that the receiving transducers ultimately measure—for example, if the receiving transducer is a camera sensor that only measures intensity, the incident and measured signals will be different.

³In many cases, the principle of superposition does hold.

⁴The phrase “incident on” is intentionally used instead of “measured by” or “received by”. This is because camera sensors oftentimes only measure light intensity, but transfer functions relate the amplitude and phase of fields between two points.

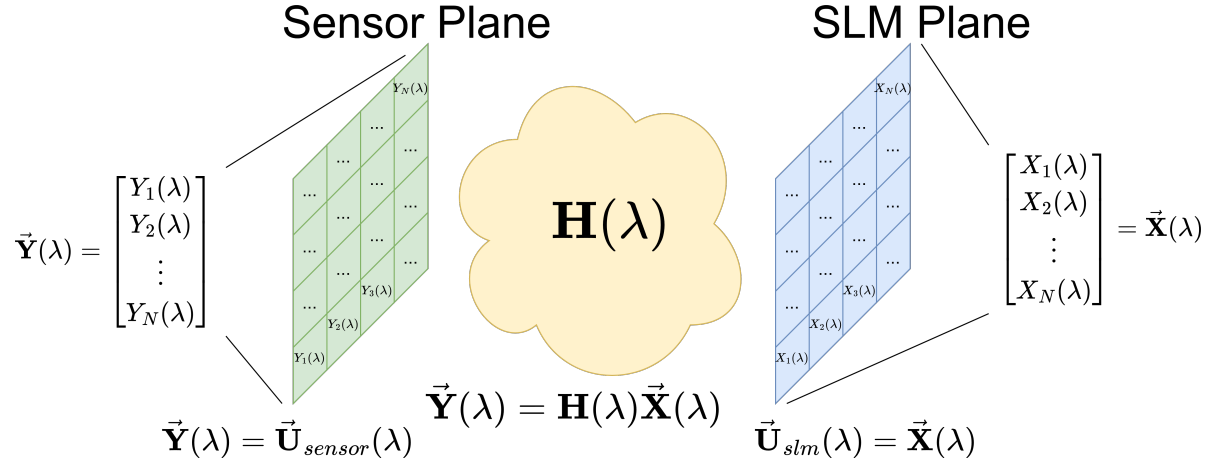


Figure 2.1: Transfer matrix illustration

transfer matrix $\mathbf{H}(\lambda)$.

Additionally, it should be noted that transfer matrices do not necessarily need to be between a set of transmitting and receiving transducers. More generally, they can relate the signals transmitted by sources at arbitrary points to the fields observed at arbitrary observation points. Thus, given two points, one could come up with a transfer function between said points.

Ultimately, obtaining transfer matrices can be desirable. A brief (but likely outdated) overview of applications of transfer matrices can be found in [13].⁵ Summarizing from [13], knowing a transmission matrix can give one information about the medium, and it allows one to perform time-reversal-based techniques to perform imaging and/or focusing (for specific references for these applications, refer to the introduction section of [13]). In short, knowing a transmission matrix can give insight into the medium/environment within which the transmitting and receiving transducers reside [13].

2.3.2 Measuring transfer matrices in the optical domain

In the acoustics and microwave/RF regimes, transfer matrices can be measured by measuring the impulse responses between elements. Analog-to-digital converters (ADC) have sufficient

⁵Note that [13] uses the term “transmission matrix” instead of “transfer matrix”.

sampling rates to be able to directly sample waveforms and digitally record the measured samples. After measuring the impulse responses, a discrete Fourier transform (DFT) can be taken to obtain the (frequency domain) transfer function at specific frequencies. Since the DFT gives both amplitude and phase data, getting amplitude and phase information about the transfer functions is “straightforward”.

However, measuring transfer matrices for optical systems is difficult. ADCs cannot sample fast enough to adequately sample optical waveforms, which makes the previous approach—which relies on taking DFTs—unusable in the context of optics. Many optical sensors, such as charge-coupled devices (CCD), can only measure intensity. If one’s sensor can only measure intensity, one could measure the amplitude of incident light, but not the phase (assuming monochromatic incident light). This poses a problem as one needs phase information to properly measure a transfer matrix.

Despite the difficulties, approaches for measuring transfer matrices at optical frequencies have been developed. In 2010, Popoff et al. [13] used an interferometry-based method to measure transfer matrices. In that work, a phase-only spatial light modulator (SLM) was used to modify an incoming monochromatic beam of light to project patterns onto a scattering medium. An Hadamard basis was used for these patterns to improve the signal-to-noise ratio and because such patterns were compatible with phase-only SLMs.⁶ On the other side of the scattering medium was a CCD camera sensor, which measured the intensity of the resulting speckle patterns. The “four phases” method [14] was used to recover the phases of the incident waveforms using CCD camera images. Additionally, instead of using a reference beam, which would require interferometric stability, part of the SLM was left unmodulated; the unmodulated, or “reference” part of the SLM served a role similar to that of a reference beam. Note that the procedure given in [13] does not give the exact transfer matrix, but instead gives an “observed” transfer matrix that is related to the actual transfer matrix. Moreover, Figure 2.2 gives an abbreviated (i.e. incomplete but illustrative) version

⁶The Hadamard basis has elements that are either $+1$ or -1 , which can be achieved via phase shifts of 0 or $\pm\pi$ respectively.

of the setup used in [13]—to see the actual setup used, please refer to [13].

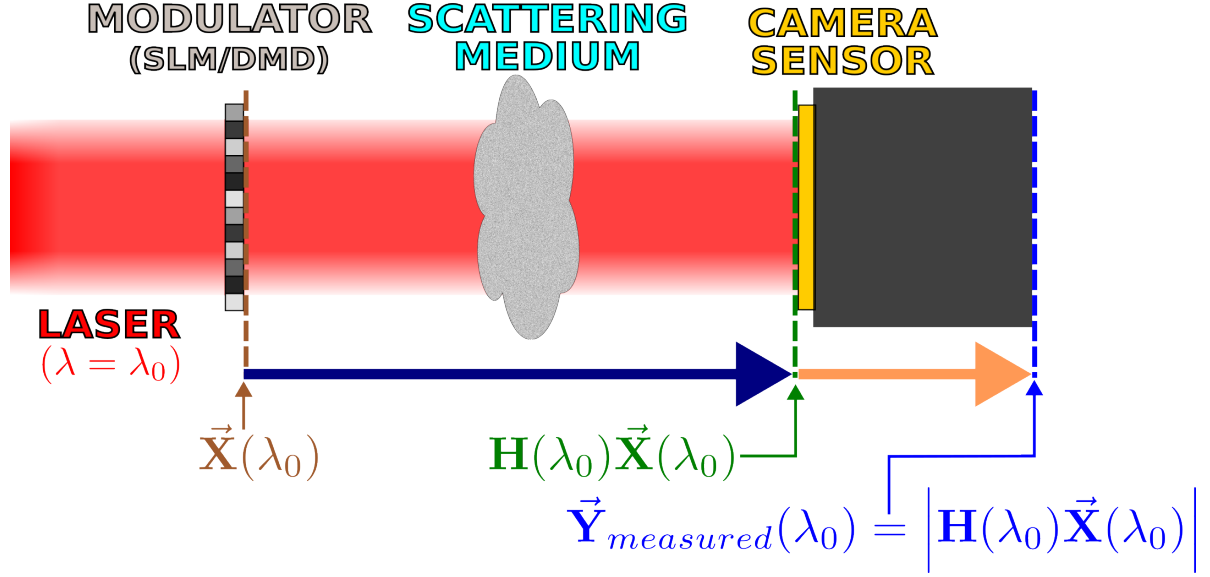


Figure 2.2: General setup for recovering a transmission (transfer) matrix

A later work by Drémeau et al. [11] in 2015 leveraged computational optics to measure transfer matrices. This work had the advantage of not requiring a reference, which was present in [13] and is required for interferometric methods. In order to collect data, Drémeau et al. in [11] used a digital micromirror device (DMD) and an imaging camera that measured light intensity. A simplified version of the setup used is shown in Figure 2.2—note that certain parts of the system are omitted in that figure for brevity. It was assumed that the output pattern from the DMD was related to the measured intensity image from the camera sensor by

$$\vec{Y}_{measured}(\lambda_0) = |\mathbf{H}(\lambda_0)\vec{X}(\lambda_0)| \quad (2.3)$$

where $\vec{X}(\lambda_0)$ is the input pattern from the DMD, $\mathbf{H}(\lambda_0)$ is the transfer matrix at $\lambda = \lambda_0$, and $\vec{Y}_{measured}(\lambda_0)$ is the measured intensity image from the camera sensor. Note that λ_0 is used here instead of λ to emphasize that monochromatic light was used for the experiment.

In order to recover the transfer matrix, [11] projected a series of calibration patterns $\{\vec{X}_1(\lambda_0), \vec{X}_P(\lambda_0), \dots, \vec{X}_P(\lambda_0)\}$ onto a scattering medium using a DMD. The resulting speckle

intensity patterns were measured by the camera sensor. Using these calibration pattern-intensity image pairs and Equation 2.3, one can come up with P equations:

$$\vec{\mathbf{Y}}_{measured,p}(\lambda_0) = \left| \mathbf{H}(\lambda_0) \vec{\mathbf{X}}_p(\lambda_0) \right|, \quad \forall p \in \{1, 2, \dots, P\}. \quad (2.4)$$

These equations can be concatenated together column-wise to form the equation

$$\mathbf{Y}_{concatenated}(\lambda_0) = |\mathbf{H}(\lambda_0) \mathbf{X}_{concatenated}(\lambda_0)| \quad (2.5)$$

where $\mathbf{Y}_{concatenated}(\lambda_0) = [\vec{\mathbf{Y}}_{measured,1}(\lambda_0), \vec{\mathbf{Y}}_{measured,2}(\lambda_0), \dots, \vec{\mathbf{Y}}_{measured,P}(\lambda_0)]$ and $\mathbf{X}_{concatenated}(\lambda_0) = [\vec{\mathbf{X}}_1(\lambda_0), \vec{\mathbf{X}}_2(\lambda_0), \dots, \vec{\mathbf{X}}_P(\lambda_0)]$. Taking the conjugate transpose of Equation 2.5 gives

$$\mathbf{Y}_{concatenated}^\dagger(\lambda_0) = \left| \mathbf{X}_{concatenated}^\dagger(\lambda_0) \mathbf{H}^\dagger(\lambda_0) \right| \quad (2.6)$$

where $(\dots)^\dagger$ denotes the conjugate transpose. Since the projected patterns $\{\vec{\mathbf{X}}_p(\lambda_0)\}_{p=1}^{p=P}$ are known and the columns of $\mathbf{X}_{concatenated}(\lambda_0)$ consist of these patterns, the matrix $\mathbf{X}_{concatenated}^\dagger(\lambda_0)$ is known. In Equation 2.6, each column of the (known) matrix $\mathbf{Y}_{concatenated}^\dagger(\lambda_0)$, the corresponding column in $\mathbf{H}^\dagger(\lambda_0)$, and the entire (known) matrix $\mathbf{X}_{concatenated}^\dagger(\lambda_0)$ together specify a phase retrieval problem in the form of Equation 2.1. Solving this phase retrieval problem gives one the rows⁷ of the transfer matrix $\mathbf{H}(\lambda)$, thus allowing one to recover the entire transfer matrix by solving a series of phase retrieval problems. This was the method that Drémeau et al. [11] used to recover the transfer matrix—in that work, a phase retrieval algorithm known as *prVBEM* [15] was used to perform the phase retrieval.

Later work by Metzler et al. [10] in 2017 and by Sharma et al. [12] in 2020 used the same fundamental method for recovering transfer matrices that was used in [11] and described above. Once again, these methods relied on computational optics, did not require the use of any sort of phase reference (unlike the work in [13]), and had a hardware setup that could

⁷Techically, it gives the complex conjugates of the rows. However, the rows can easily be obtained if one knows their complex conjugates.

be abbreviated to that of Figure 2.2. However, [10] and [12] differed from [11] as the former two used an SLM instead of a DMD for the light-modulating element. Another difference is that both [10] and [12] used a different phase retrieval algorithm called *prVAMP*, which is described in [10], to solve the necessary phase retrieval for recovering transfer matrices.⁸ Finally, while outside the scope of this subsection, it can be noted that [10] and [12] used the transfer matrix and an additional phase retrieval step to image behind scattering media.

⁸Comparisons of various phase retrieval algorithms can be found in [10] and [12].

Chapter 3

DORT Background

3.1 Introduction

In Section 2.3, the idea of a transfer matrix which relates, in the frequency domain, signals transmitted by a set of transmitting transducers to signals incident on a set of receiving transducers was introduced. Transfer matrices can encode information about the medium surrounding the transmitting and receiving transducers [13] [16].

One technique that utilizes transfer matrices is known as the DORT technique, where DORT is a French acronym that stands for *Décomposition de l'Opérateur de Retournement Temporel*, which can be translated as “decomposition of the time-reversal operator”. The DORT technique arose from the study of time-reversal mirrors [3], which are described in [17]. The seminal paper on DORT, [18], was done in the realm of acoustics. The work demonstrated how DORT could be used to selectively focus on scatterers (or “targets”) in a medium using an array of ultrasonic transducers. Since then, the DORT technique has been applied outside of acoustics and in the realm of microwaves [4] [19] [20] and optics [8] [9] [16].

The DORT technique can be performed by taking the singular value decomposition (SVD) of the frequency domain transfer matrix¹ [4] [19] [20], or equiv-

¹Note that the transfer matrix is denoted as $\mathbf{H}(\lambda)$ in this thesis.

alently, by performing eigendecomposition of a so-called time-reversal operator [4] [21].² It should be noted, however, that the eigendecompositions of time-reversal operators can be derived from the SVDs of transfer matrices—the singular vectors and the squares of the singular values from SVD are eigenvectors and eigenvalues respectively [4].³

DORT can be used for a number of tasks. One such task is the detection of scatterers in a medium [21]. The eigenvalues from the eigendecomposition of a time-reversal operator (which are the squares of the singular values of the transfer matrix [4]) are proportional to the reflectivity of the corresponding scatterers. As such, the eigenvalues (or singular values) can be used to detect the presence of scatterers in a medium.

Another application of DORT is selective focusing on scatterers [4] [18] [19] [20] [21] energy on scatterers. Assuming well-resolved scatterers and no degenerate eigenvalues in the time-reversal operator, the singular vectors of the transfer matrix (or equivalently, the eigenvectors of the time-reversal operator) obtained from DORT should define signals which, when transmitted from transducers in the system, selectively focus on a particular scatterer. One potential application of this selective focusing ability of DORT is wireless power transfer [20], which had been proposed in [23].

DORT can also be used to image scatterers [4] [19] [20] [22]. Singular vectors obtained from DORT form a set of signals that can be numerically backpropagated, i.e. one simulates transmitting such signals into a medium [4] [19] [20] [22]. The backpropagated signals can either be single-frequency signals (i.e. continuous wave or CW), or consist of multiple frequencies (e.g. a band of frequencies). Under proper conditions (e.g. “well-resolved scatterers”), each field from backpropagation should reach a maximum near the corresponding scatterer, thus indicating the location of the scatterer.

²The reason why the word “a . . . time-reversal operator” is used instead of “the . . . time-reversal operator” is because there are actually two time-reversal operators when the transmitting and receiving transducers are separate: one for the transmitting array and one for the receiving array [22].

³The claim that one can derive eigendecompositions of time-reversal operators from SVDs of transfer matrices relies on the assumption that the reciprocity theorem holds. See [22] for an illustration of this. It should be noted that oftentimes, one can assume reciprocity—thus the aforementioned claim is often true.

3.2 A quick demonstration of DORT

In the previous section, Section 3.1, DORT was introduced. This section will provide some quick illustrations/examples to illustrate—non-comprehensively—how DORT can be used.

Figure 3.1 shows an example of imaging with DORT.⁴ A set of 64 transmit/receive transducers spaced 0.5 mm apart—with each transducer being both a transmitter and receiver⁵—along with two pointlike scatterers are simulated. The transmitted signals are continuous (sinusoidal) wave signals with a wavelength of approximately 0.9993 mm.⁶ The background (i.e. surrounding) medium is assumed to be a homogeneous medium, and scalar waves are assumed. The transfer matrix is computed by assuming Green’s functions of the form given in Appendix Section A.1⁷

$$G(\vec{r}, \vec{r}_{source}; \omega) = \frac{e^{+jk\|\vec{r} - \vec{r}_{source}\|}}{\|\vec{r} - \vec{r}_{source}\|} \quad (3.1)$$

and by using the first-order Born approximation, which assumes that the scattered field at a point is proportional to the incident field at that point. The scattering is assumed to be isotropic. After computing the transfer matrix, DORT is performed by taking the singular value decomposition of the transfer matrix. This gives singular vectors that define signals that can be numerically backpropagated. These signals are numerically backpropagated, and the resulting fields are computed by assuming the Green’s function in Equation 3.1. For more information on the process behind obtaining Figure 3.1, see Chapter 7—the process for obtaining Figure 3.1 is essentially the same as what was described in Chapter 7.

It can be seen in Figure 3.1 that each individual field reaches its maximum around a particular scatterer, and that there is one maximum per backpropagated field. The fields can be used to form images of the scatterers. Thus, Figure 3.1 demonstrates imaging, detection

⁴The code used to produce Figure 3.1 has been published online. See “[Online Availability](#)” near the beginning of this thesis for more information.

⁵Note that in general, one can also have separate transmitting and receiving transducers.

⁶For electromagnetic waves in free space, the corresponding frequency is 300 GHz.

⁷Note that in equation 3.1, k is the wavenumber. Also note that under the convention that phasors rotate clockwise in time—which is the convention that is being used here—the positive sign in the $e^{+jk\|\vec{r} - \vec{r}_{source}\|}$ term in Equation 3.1 represents an outgoing wave.

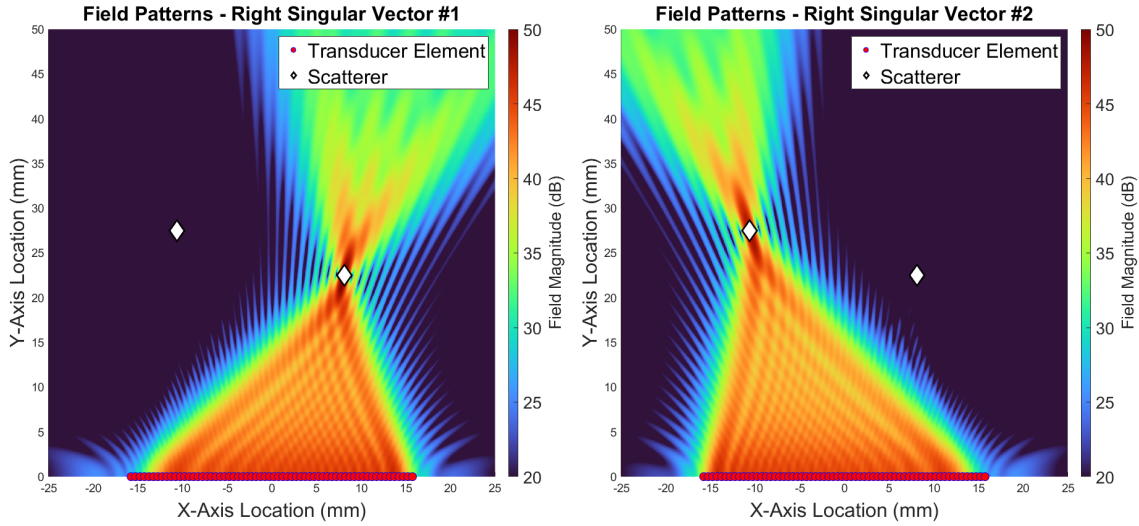


Figure 3.1: Imaging scatterers in the near-field with DORT and backpropagation

of scatterers, and selective focusing using DORT. It should be noted that the sharp local maximima observed in Figure 3.1 are possible because the scatterers are in the near-field of the array.

Figure 3.2 shows another example of backpropagation.⁸ The setup for Figure 3.2 is the same as for Figure 3.1, except the number of transmitting/receiving elements is reduced to 8 and the scatterers are placed further away. The same assumptions that were made when producing Figure 3.1 are made when producing Figure 3.2, namely scalar waves, the first-order Born approximation, isotropic scattering, and Green's functions of the form shown in Equation 3.1. More information on the process behind obtaining Figure 3.2 can be found in Chapter 7—Figure 3.2 essentially follows the same process that was described in Chapter 7.

In Figure 3.2, a set of 8 transmit/receive transducers along with two scatterers, all embedded in a homogeneous medium, are simulated. Due to the smaller array size and the fact that the scatterers are further away relative to their locations in Figure 3.1, the scatterers are located in the far-field of the array. When scatterers are located in the far-field, as shown

⁸The code used to produce Figure 3.2 has been published online. See “[Online Availability](#)” near the beginning of this thesis for more information.

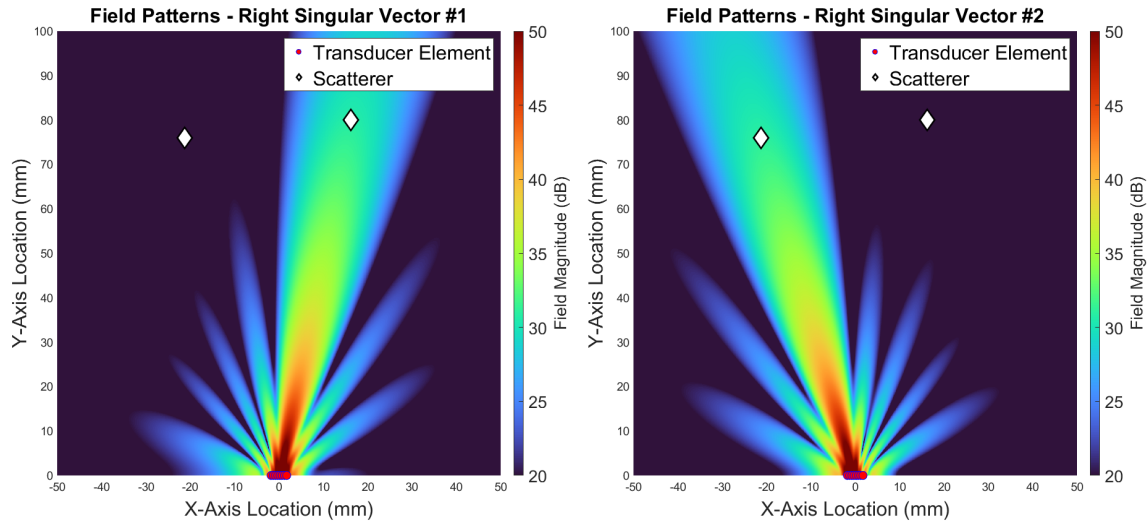


Figure 3.2: Detecting scatterers in the far-field with DORT and backpropagation

in Figure 3.2, one cannot get good images of the scatterers. This is because in the far-field, backpropagating fields only allows one to resolve direction—one cannot resolve a precise location. It can be seen in Figure 3.2 that the fields are strong in the general *directions* of the scatterers but do not give information about the range/distance of the scatterers.

Finally, as an aside, it can be noted that the plots in Figures 3.1 and 3.2 are supposed to represent electromagnetic waves at 300 GHz with a background (i.e. surrounding) medium of free space. However, the simulation is not entirely accurate as scalar waves were assumed—as opposed to vector waves, which are what electromagnetic waves are—and the transmitting and receiving transducers were assumed to be isotropic radiators and receivers respectively. These assumptions are not physically accurate—not to electromagnetic waves at least⁹—so the plots in Figures 3.1 and 3.2 are not the most representative of a physical process.

⁹For instance, it is impossible to have an isotropic radiator of electromagnetic waves.

3.3 Transfer matrix model assumed by DORT

NOTE:

The model described in this section has been described in the literature in [3], [18], and [21].

In Section 2.3.1, a general model for relating transmitted fields to those fields incident on receiving elements was given. In that model, the (frequency domain) fields transmitted by a set of transmitting transducers ($\vec{\mathbf{X}}(\lambda)$) were related to the fields incident on a set of receiving transducers ($\vec{\mathbf{Y}}(\lambda)$) by a transfer matrix ($\mathbf{H}(\lambda)$). This is a very general model that merely posits that—in the frequency domain—the fields incident on the receivers is a linear combination of the fields transmitted by the receivers.

In the context of DORT, certain assumptions are typically made about the system being analyzed. This allows one to obtain a more precise model for the transfer matrix. One assumption that is often made is that one has a set of pointlike scatterers¹⁰ embedded in some sort of medium, and that these scatterers follow the first-order Born approximation¹¹. Another assumption that is typically made is that energy does not directly travel directly between the transmitting and receiving transducers, and instead must bounce off the scatterers first—in other words, it is often assumed that no direct coupling (transmitters to receivers) is present and that any received signals must have been scattered first.

Under these assumptions, propagation from transmitters to receivers can be modeled in three steps: propagation from the transmitting transducers to the scatterers, scattering of the fields incident on the scatterers, and propagation from the scatterers to the receiving transducers. Each of these steps can be expressed as its own matrix, and the transfer matrix

¹⁰It should be noted that non-pointlike, or “extended”, scatterers are sometimes considered in the context of DORT. However, many works on DORT assume/deal with pointlike scatterers.

¹¹Assuming that the scatterers follow the first-order Born approximation allows one to assume that the scattered fields are produced by induced point sources located at the scatterers that are proportional in amplitude to the incident fields at the corresponding scatterer locations.

$\mathbf{H}(\lambda)$ can be broken down into the product of these three matrices, i.e. as

$$\mathbf{H}(\lambda) = \mathbf{B}(\lambda)\mathbf{S}(\lambda)\mathbf{F}(\lambda). \quad (3.2)$$

In Equation 3.2, $\mathbf{F}(\lambda)$ is the transfer matrix that relates the fields transmitted by the transmitting transducers to the fields incident on the scatterers. The matrix $\mathbf{F}(\lambda)$ models propagation from the transmitting transducers to the scatterers. $\mathbf{S}(\lambda)$ is the matrix that relates the fields incident on the scatterers to the outgoing (scattered) fields the scatterers. That matrix, $\mathbf{S}(\lambda)$, models scattering. Finally, $\mathbf{B}(\lambda)$ is the matrix relating the fields outgoing from the scatterers to the fields incident on the receiving transducers. $\mathbf{B}(\lambda)$ models propagation from the scatterers to the receiving transducers. Figure 3.3 gives an illustration of the process described in Equation 3.2.

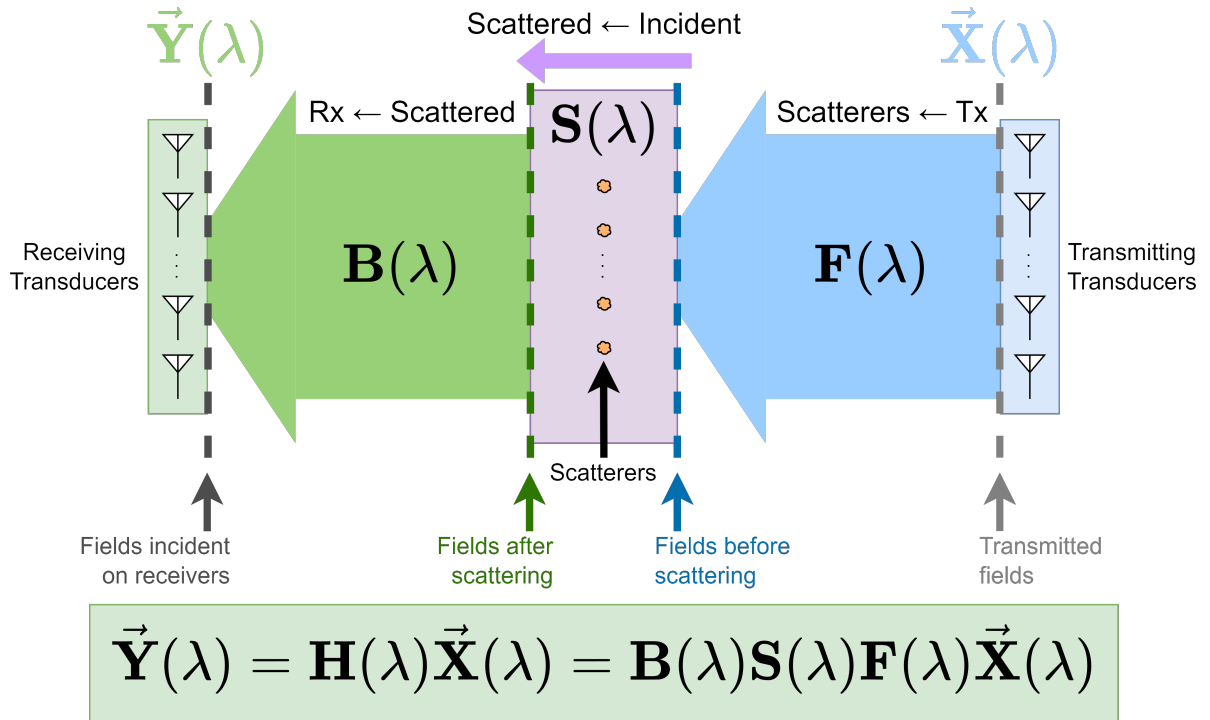


Figure 3.3: The transfer matrix \mathbf{H} decomposed into a product of three matrices

The dimensions of the matrices $\mathbf{B}(\lambda)$, $\mathbf{S}(\lambda)$, and $\mathbf{F}(\lambda)$ depend on the number of transmitting transducers, receiving transducers, and scatterers. Specifically, assuming that there

are N transmitting transducers, M receiving transducers, and D scatterers, the size of $\mathbf{B}(\lambda)$ is $M \times D$, the size of $\mathbf{S}(\lambda)$ is $D \times D$, and the size of $\mathbf{F}(\lambda)$ is $D \times N$ [3]. Additionally, $\vec{\mathbf{X}}(\lambda)$ is an $N \times 1$ column vector and $\vec{\mathbf{Y}}(\lambda)$ is an $M \times 1$ column vector.

3.4 Ideally-resolved and well-resolved assumptions

NOTE:

For a summary of the mathematical implications of the terms “ideally-resolved” and “well-resolved”, refer to the end of this section (Section 3.4).

In the DORT literature, it is oftentimes assumed that one has a set of discrete scatterers that are “ideally-resolved” or “well-resolved”. From [3] and [24], the meaning of “ideally-resolved” can be inferred to mean that using time-reversal focusing, one can focus on each scatterer without sending energy to the other scatterers. The definition of time-reversal focusing can be inferred from [18] and [21]. From [21], “well-resolved” means that the scatterers are *approximately* “ideally-resolved”. This section will attempt to explain all of the aforementioned terms (“ideally-resolved”, “well-resolved”, and “time-reversal focusing”), but one should consult these sources for more information if necessary.

To understand what time-reversal focusing is, note that given an array of transducers (transmitting, receiving, or both), for each scatterer, there is a set of impulse responses between the transducers and the scatterer. Now, assume a reciprocal medium (this is typically assumed). Under that assumption, these impulse responses are the same regardless of whether they are going from the scatterer’s position to the transducers’ positions or going from the transducers’ positions to the scatterer’s position. Ignoring the response of the transducer elements themselves¹²—i.e. pretending that the transducers can transmit and/or receive an impulse without distortion—time-reversal focusing is when the transducers send out time-reversed versions of the impulse responses going from their positions to a scatterer’s

¹²Note that the work in [21] considers non-ideal transducer responses.

position.

Put differently, imagine that a point source, located at a scatterer's position, emits an impulse and the (impulse) responses at the transducers' locations were measured. Time-reversal focusing on that scatterer means that time-reversed versions of those aforementioned (impulse) responses are retransmitted by the transducers—again, this is assuming ideal transducer responses for simplicity.¹³ It should be noted that time-reversal focuses has been noted to, in a number of cases, result in selective focusing on scatterers [17] [18], i.e. a wavefront that converges upon a particular scatterer.

In the frequency domain, and under the model described in Section 3.3, time-reversal focusing from the transmitting transducers would look like transmitting the signals $[\mathbf{F}_{i,*}^*(\lambda)]^\top$ from the transmitting transducers; and time-reversal focusing from the receiving transducers would look like transmitting the signals $\mathbf{B}_{*,i}^*(\lambda)$ from the receiving transducers¹⁴. Note that $1 \leq i \in \mathbb{Z} \leq D$ where D is the number of scatterers. The complex conjugation comes from the fact that for real-valued signals¹⁵, time-reversal is equivalent to complex conjugation in the frequency domain.

For the transmitting array, again in the frequency domain, the fields incident on the scatterers when performing time-reversal focusing on the i^{th} scatterer can be written as

$$\vec{\mathbf{W}}^{(f)}(\lambda) = \mathbf{F}(\lambda) [\mathbf{F}_{i,*}^*(\lambda)]^\top = \begin{bmatrix} F_{1,1}(\lambda) & F_{1,2}(\lambda) & \cdots & F_{1,N}(\lambda) \\ F_{2,1}(\lambda) & F_{2,2}(\lambda) & \cdots & F_{2,N}(\lambda) \\ \vdots & \vdots & \ddots & \vdots \\ F_{D,1}(\lambda) & F_{D,2}(\lambda) & \cdots & F_{D,N}(\lambda) \end{bmatrix} \begin{bmatrix} F_{i,1}^*(\lambda) \\ F_{i,2}^*(\lambda) \\ \vdots \\ F_{i,N}^*(\lambda) \end{bmatrix} = \begin{bmatrix} \sum_{k=1}^N F_{1,k}(\lambda) F_{i,k}^*(\lambda) \\ \sum_{k=1}^N F_{2,k}(\lambda) F_{i,k}^*(\lambda) \\ \vdots \\ \sum_{k=1}^N F_{D,k}(\lambda) F_{i,k}^*(\lambda) \end{bmatrix}$$

The rightmost part of the expression above consists of complex inner products (complex dot

¹³The definition of time-reversal focusing can include the transducer response in reception. In [18] and [21], the transducer response is considered.

¹⁴Note that the receiving transducers might not physically be able to transmit. However, if they cannot, one can pretend that they can.

¹⁵Since we are dealing with fields, the time-domain signals should be real-valued.

products) with conjugate linearity in the second argument.¹⁶ Now, recall that being ideally-resolved means that time-reversal focusing will only send energy to individual scatterers. This means that the fields $\mathbf{W}^{(f)}(\lambda)$ incident on the scatterers must only have one non-zero element. This means that all of the complex inner products shown above must be zero, except for one. Thus, $[\mathbf{F}_{i,*}(\lambda)]^\top$ must be orthogonal to all of the rows of $\mathbf{F}(\lambda)$ except for one—assuming that $[\mathbf{F}_{i,*}^*(\lambda)]^\top$ is non-zero, the single row that is not orthogonal to $[\mathbf{F}_{i,*}(\lambda)]^\top$ must be the i^{th} row as a non-zero vector cannot be orthogonal to itself. Additionally, since these statements should apply for all $1 \leq i \in \mathbb{Z} \leq D$, and $\mathbf{F}(\lambda)$ is $D \times N$ in dimension, all of the rows of $\mathbf{F}(\lambda)$ must be mutually orthogonal in order for the scatterers to be ideally-resolved from the transmitting transducers' point of view.

Now, imagine that one performed time-reversal focusing with the receiving transducers.¹⁷ This means that the receiving transducers transmit $\mathbf{B}_{*,i}^*(\lambda)$. The fields incident on the scatterers would then be $\mathbf{W}^{(b)}(\lambda) = \mathbf{B}^\top(\lambda)\mathbf{B}_{*,i}^*(\lambda)$.¹⁸ Going through a similar argument to the one in the previous paragraph, one can argue that the columns of $\mathbf{B}(\lambda)$ must be mutually orthogonal in order for the scatterers to be ideally-resolved from the point of view of the receiving transducers.

It can also be noted that if $\mathbf{F}(\lambda)$ had a row that consisted of all zeros, or if $\mathbf{B}(\lambda)$ had a column that consisted of all zeros, that would imply that time-reversal focusing cannot focus on a scatterer as the fields incident on the scatterer associated with the zero-vector row/column would always be zero. Since being ideally-resolved requires that one be able to focus on all of the scatterers individually without sending energy to the other scatterers, having such a condition would imply that the scatterers are not ideally-resolved. Therefore, ideally-resolvedness requires that none of the rows (resp. columns) of $\mathbf{F}(\lambda)$ (resp. $\mathbf{B}(\lambda)$) consist of all zeros.

¹⁶There are different conventions on the complex inner product/complex dot product. The opposite convention, which is often used in physics, is to have conjugate linearity in the first argument.

¹⁷Depending on one's physical setup, the receiving transducers may or may not be able to transmit. However, one can pretend that the receiving transducers can transmit in this case.

¹⁸Note that reciprocity—which is a common assumption—is being assumed here. Reciprocity means that the transfer matrix going from the receiving transducers to the scatterers is $\mathbf{B}^\top(\lambda)$.

Furthermore, ideally-resolvedness excludes the possibility of multiple scattering. If there was multiple scattering, then even if energy was only incident on one scatterer, energy would reach other scatterers. Mathematically speaking, there being no multiple scattering implies that the matrix describing scattering, must be a diagonal matrix. Therefore, ideally-resolvedness requires that the matrix describing scattering, in this case $\mathbf{S}(\lambda)$, be a diagonal matrix.

Note that it has been implicitly assumed here that ideally-resolved means the scatterers are ideally-resolved from the point of view of both the transmitting and receiving transducers. It should be noted that early literature on DORT [18] [21] [24] assumed that the transmitting and receiving transducers were the same, thus ideally-resolvedness implied ideally-resolvedness for both the transmitting transducers and the receiving transducers—these works did not have to consider the more general case of the transmitting and receiving transducers being different. Despite the early literature not considering such a case, it makes sense to define the term “ideally-resolved” in the manner stated earlier as it allows for certain nice mathematical results to follow (see Appendix B). Therefore, this work will define “ideally-resolved” to mean “ideally-resolved from the perspectives of both the transmitting transducers and the receiving transducers”.

It should also be noted that the literature defines an additional term: well-resolved. Well-resolved essentially means approximately ideally-resolved¹⁹ [21]. Results/expressions for the well-resolved case should be approximated by results/expressions for the ideally-resolved case.

To summarize, under the model given in Section 3.3. the ideally-resolved scatterers assumption implies that the rows of the matrix $\mathbf{F}(\lambda)$ are mutually orthogonal and non-zero, the columns of the matrix $\mathbf{B}(\lambda)$ are mutually orthogonal and non-zero, and the matrix $\mathbf{S}(\lambda)$

¹⁹The source that defines well-resolved [21] mathematically describes being well-resolved as the rows of the propagation matrix (analogous to $\mathbf{F}(\lambda)$ in this document) being approximately orthogonal. Non-orthogonal rows, however, is not the only way to break the ideally-resolved assumption (e.g. multiple scattering among scatterers can break that assumption). It can be inferred though that any case where scatterers are nearly ideally-resolved could be labeled as “well-resolved”, so long as the results for the ideally-resolved case approximately hold.

is a diagonal matrix.²⁰ These assumptions are convenient mathematically, and, along with the model described in Section 3.3, are used to derive Equations B.24, B.26, B.35, and B.38. Finally, the well-resolved assumption implies that the scatterers are approximately ideally-resolved, and that mathematical results from the ideally-resolved case approximately apply.

3.5 Eigenstructure mixing and demixing

DORT is done on a per-frequency/per-wavelength basis. DORT is typically performed by taking the singular value decomposition (SVD) of the frequency domain transfer matrix at evaluated discrete frequencies/wavelengths. Thus, one SVD is performed for each frequency/wavelength.

Ideally, each singular vector number corresponds to a specific scatterer. One might assume that the i^{th} singular vector would correspond to the same scatterer for all frequencies/wavelengths. However, this is not necessarily the case. Anytime DORT is done over more than one frequency/wavelength, one runs into the possibility of “eigenstructure mixing” [20]. When eigenstructure mixing has occurred, one encounters a situation where for some i , the i^{th} singular vector does not correspond to the same scatterer for all frequencies/wavelengths. This can be problematic whenever SVDs at multiple frequencies/wavelengths are being used. It should be noted though that eigenstructure mixing does not always occur, and that in a fair number of cases, it does not occur [20].

One can alleviate this the eigenstructure mixing problem by noting that singular vectors at nearby frequencies/wavelengths corresponding to the same scatterer are generally “correlated”, i.e. the complex inner product/complex dot product ***is not*** approximately

²⁰It is theoretically possible for the scatterers to be ideally-resolved from the perspective of only one set—either transmitting or receiving—of transducers. However, such cases are less convenient mathematically (see Appendix Section B for an example of a derivation). Therefore, it will be assumed that the terms ideally-resolved/well-resolved will refer to the scatterers being ideally-resolved/well-resolved from the perspective of both the transmitting and receiving transducers.

zero, and those corresponding to different scatterers are generally “uncorrelated”, i.e. the complex inner product/complex dot product *is* approximately zero [20]. This information can be used to rearrange the singular vector numberings so that a given numbered singular vector will correspond to the same scatterer at all frequencies/wavelengths. This procedure is known as “eigenstructure demixing” [20].

It should be noted, however, that with DORT, a scatterer can potentially have multiple different scattering patterns associated with it [16]. In this case, multiple singular values and singular vectors can correspond to a given scatterer. The case of multiple singular values and singular vectors corresponding to a single scatterer does not seem to have been mentioned in [20], but this case showed up in [16]. The way that the eigenstructure mixing issue was formulated in [20] does not address the case of multiple different scattering patterns for a single scatterer, however. Still, it may be possible to extend the definition of eigenstructure demixing to refer to a case where the scattering pattern and scatterer corresponding to a given numbered singular vector is not consistent across wavelengths—this definition was not given in [20] though.

Chapter 4

DORT Equations

NOTE:

A full derivation of the equations in this chapter (Equations B.24, B.26, B.35, and B.38) can be found in Appendix B.

As mentioned in Section 3.1, DORT can be performed by taking the singular value decomposition (SVD) of the transfer matrix $\mathbf{H}(\lambda)$. As such, having expressions for the matrices $\mathbf{U}(\lambda)$, $\Sigma(\lambda)$, and $\mathbf{V}(\lambda)$ associated with taking the SVD of a transfer matrix $\mathbf{H}(\lambda)$ is desirable when one is trying to characterize the results of performing DORT.

It turns out that under certain assumptions, one can get relatively simple expressions that describe the aforementioned $\mathbf{U}(\lambda)$, $\Sigma(\lambda)$, and $\mathbf{V}(\lambda)$ matrices. In Section 3.3, a model that is frequently assumed in DORT is described. If one combines that assumed model with the assumption of ideally-resolved scatterers (the term “ideally-resolved” is described in Section 3.4), one can get tractable closed-form expressions for the results of taking the SVD of the transfer matrix $\mathbf{H}(\lambda)$. Specifically, one gets the following equations:

$$\mathbf{V}_{*,i}(\lambda) = \left[\frac{[\mathbf{F}_{i,*}^*(\lambda)]^\top}{\sqrt{\sum_{\ell=1}^N |F_{i,\ell}(\lambda)|^2}} \right] e^{j\phi_i(\lambda)}, \text{ for } 1 \leq i \in \mathbb{Z} \leq D \quad (\text{B.24})$$

$$\mathbf{U}_{*,i}(\lambda) = \left[\frac{\mathbf{B}_{*,i}(\lambda)}{\sqrt{\sum_{\ell=1}^M |B_{\ell,i}(\lambda)|^2}} \right] e^{j\theta_i(\lambda)}, \text{ for } 1 \leq i \in \mathbb{Z} \leq D \quad (\text{B.26})$$

$$\Sigma_{i,j}(\lambda) = \begin{cases} |S_{i,i}(\lambda)| \left(\sqrt{\sum_{\ell=1}^N |F_{i,\ell}(\lambda)|^2} \right) \left(\sqrt{\sum_{\ell=1}^M |B_{\ell,i}(\lambda)|^2} \right), & \text{for } (i=j) \wedge (i \leq D) \\ 0, & \text{for } (i \neq j) \vee (i > D). \end{cases} \quad (\text{B.35})$$

$$\theta_i(\lambda) - \phi_i(\lambda) = \text{Arg}(S_{i,i}(\lambda)) + 2\pi m_i(\lambda), \text{ for } 1 \leq i \in \mathbb{Z} \leq D \text{ such that } S_{i,i}(\lambda) \neq 0, \quad (\text{B.38})$$

and where $m_i(\lambda)$ is some integer.

A full derivation of Equations B.24, B.26, B.35, and B.38 is given in Appendix B. Note that when the scatterers are well-resolved instead of ideally-resolved (the terms “well-resolved” and “ideally-resolved” are described in Section 3.4), the equations above (Equations B.24, B.26, B.35, and B.38) are only approximately true.

In Equations B.24, B.26, B.35, and B.38, $\mathbf{U}(\lambda)$, $\Sigma(\lambda)$, and $\mathbf{V}(\lambda)$ come from taking the SVD of the transfer matrix. Note that the transfer matrix $\mathbf{H}(\lambda)$ obeys the equalities $\mathbf{H}(\lambda) = \mathbf{B}(\lambda)\mathbf{S}(\lambda)\mathbf{F}(\lambda)$ and $\mathbf{H}(\lambda) = \mathbf{U}(\lambda)\Sigma(\lambda)\mathbf{V}^\dagger(\lambda)$. Additionally, note that for a $\mathbf{H}(\lambda)$ matrix that is $M \times N$ in size, the matrices $\mathbf{U}(\lambda)$, $\Sigma(\lambda)$, and $\mathbf{V}(\lambda)$ will be $M \times M$, $M \times N$, and $N \times N$ in size respectively.

Now, it should be noted that Equations B.24, B.26, B.35, and B.38 have some caveats to them. Mainly, the equations do not apply for i corresponding to repeated singular values (i.e. singular values that whose values show up more than once) and might not apply for i corresponding to zero-valued singular values (i.e. i such that $\Sigma_{i,i} = 0$). For a full list of caveats on these equations (Equations B.24, B.26, B.35, and B.38), please refer to Appendix Section B.7.

It should also be noted that Equations B.24, B.26, B.35, and B.38 assume a certain “structure” or “ordering” to the $\mathbf{B}(\lambda)$, $\mathbf{S}(\lambda)$, and $\mathbf{F}(\lambda)$ matrices. Such a “structure” or “ordering” can be assumed without altering the product $\mathbf{H}(\lambda) = \mathbf{B}(\lambda)\mathbf{S}(\lambda)\mathbf{F}(\lambda)$. Assuming that “structure” or “ordering” should not affect anything unless one explicitly defines the

matrices $\mathbf{B}(\lambda)$, $\mathbf{S}(\lambda)$, and $\mathbf{F}(\lambda)$ and defines them in such a way that the “structure” or “ordering” of those matrices is different from the aforementioned assumed “structure” or “ordering”—in that case, Equations B.24, B.26, B.35, and B.38 would not be correct. It should be noted that in general, one can either choose to explicitly define the $\mathbf{B}(\lambda)$, $\mathbf{S}(\lambda)$, and $\mathbf{F}(\lambda)$ matrices in such a way that the assumed “structure” or “ordering” is satisfied, or one could leave those matrices undefined and instead implicitly define them via Equations B.24, B.26, B.35, and B.38—both of these options are compatible with the “structure” or “ordering” assumption, and neither option should be difficult or negatively impactful to make. For more information, please refer to Appendix Section B.1.2.

Comparison of equations with those in existing literature

Equations B.24, B.26, B.35, and B.38 in this chapter (Chapter 4) are more general and complete than those found in [3] and [4]. Those equations—Equations B.24, B.26, B.35, and B.38 in this thesis—are for the general case of separate transmitting and receiving arrays, and address SVD phase factors (the term “SVD phase factors” refers to the $e^{j\phi_i(\lambda)}$ and $e^{j\theta_i(\lambda)}$ terms in Equations B.24 and B.26 in this thesis).

Equations 12 and 13 in [3] correspond to Equations B.35 and B.24 in this thesis. Like this thesis, [3] does handle the more general case of a bistatic array arrangement. However, no SVD phase factor is present in Equation 13 in [3], and there do not appear to be equations in [3] corresponding to Equations B.26 and B.38 in this thesis. It should be noted though that Equation 13 in [3] describes an eigenvector, not specifically a singular vector—this is different from Equation B.24 in this thesis, which describes a singular vector. It should also be noted that it can be inferred that Equation 12 in [3] gives singular values¹, like Equation B.35 in this thesis effectively does.

Equations 3.21 and 3.31 in [4] correspond to Equation B.24 in this thesis, and Equations

¹The $\Delta_2 \mathbf{C} \Delta_1$ matrix in [3] corresponds to the Σ matrix from singular value decomposition. Equation 12 in [3] gives the diagonal elements of the aforementioned $\Delta_2 \mathbf{C} \Delta_1$ matrix. Therefore, Equation 12 in [3] gives singular values.

3.20 and 3.22 in [4] correspond to Equations B.26 and B.35 in this thesis respectively.² However, Equations 3.20-3.22 and 3.31 in [4] are for a monostatic array arrangement³, which is less general than the case covered in this thesis. This thesis handles the case of separate transmit and receive arrays—i.e. a bistatic array arrangement—which is a more general case⁴ than what was considered in [4]. Additionally, [4] does not fully address SVD phase factors—an SVD phase factor is present in Equation 3.31 in [4], but there is no SVD phase factor on Equation 3.20 in [4]. Moreover, as far as the author of this thesis can tell, there is no equation in [4] that gives a constraint on SVD phase factor arguments⁵ like Equation B.38 in this thesis does. It should be noted though that [4] considers the more general case of taking the SVD of a multistatic data matrix (denoted as “MDM” in [4]).⁶ The MDM considers responses to pulses that are not necessarily impulses. In contrast, the transfer matrix deals with responses to impulses—this thesis considers taking the SVD of transfer matrices, not multistatic data matrices. To summarize, unlike this thesis, [4] is for the more specific monostatic array case and does not fully address the issue of SVD phase factors; [4] does, however, consider the more general case of a multistatic data matrix.

²Equations 3.21 and 3.21 in [4] and Equation B.24 in this thesis describe right-singular vectors. Equation 3.20 in [19] and Equation B.26 in this thesis describe left-singular vectors. Equation 3.22 in [4] and Equation B.35 in this thesis describe singular values.

³As in, the transmit and receive arrays are the same array.

⁴One can think of a monostatic array arrangement as two separate arrays that are located in exactly the same spot. Thus, the case of separate transmitting and receiving arrays includes the case of a single array that both transmits and receives.

⁵“Arguments” as in complex arguments.

⁶A transfer matrix is a specific case of an MDM. If one lets the input pulse in Chapter 3 of [4] be an impulse—i.e. letting $s(\omega)$ in Chapter 3 of [4] be 1 for all ω —the MDM in Chapter 3 of [4] becomes the transfer matrix.

Chapter 5

Synthetic Wavelengths Background

Imaging through scattering media is a difficult task. When a scattering medium is present between an imaging system and an object, the scattering medium will typically degrade the performance of the imaging system. However, this is not to say that it is impossible to image through scattering media. One approach for imaging through scattering media is to use the concept of *synthetic wavelengths*. The idea behind synthetic wavelengths is that one does some form of processing, either computationally or physically, to effectively get a longer wavelength than the wavelengths that are present in one's measurements—one can effectively get a measurement with a wavelength that is orders of magnitude larger than the wavelengths one actually used to perform measurements. This approach was used in [7] to image through scattering media.

It should be noted though that synthetic wavelengths are useful for cases outside of imaging through scattering media as well. More generally, [7] used synthetic wavelengths to image objects when there was no direct line-of-sight to the object, which is a more general case which imaging through scattering media falls under. Synthetic wavelengths were also used in [25] to measure, with high depth range and resolution, the three-dimensional surface variation of optically rough objects.

Now, as demonstrated in [7] and [25], the ability to effectively work with a longer wave-

length is a useful ability. Various aberrations, such as those from a scattering medium, create variations in path length [7]. These path length variations manifest themselves as variations in measured phases. If the path lengths are too large relative to the wavelength, this effectively randomizes one's measured phase. Using a larger wavelength—or a larger *synthetic* wavelength—mitigates this issue as for a larger wavelength, the induced phase shifts would be less. This allows one to gain more useful information from the phases.

The basic process of using synthetic wavelengths involves having two complex-valued optical fields. These fields can be represented in the form [7]

$$E(x, y; \lambda) = A(x, y; \lambda)e^{j\phi(x, y; \lambda)} \quad (5.1)$$

where $A(x, y; \lambda)$ is non-negative and real-valued and $\phi(x, y; \lambda)$ is real-valued. Given two complex-valued optical fields $E(x, y; \lambda_1)$ and $E(x, y; \lambda_2)$ at two nearby¹ wavelengths λ_1 and λ_2 , a synthetic optical field $E(x, y; \Lambda)$ with synthetic wavelength Λ , where $\Lambda = \frac{\lambda_1 \lambda_2}{|\lambda_1 - \lambda_2|}$, can be created according to the formula [7]

$$E(x, y; \Lambda) = E(x, y; \lambda_1)E^*(x, y; \lambda_2), \quad (5.2)$$

where $*$ denotes complex conjugation. In other words, a synthetic optical field is created via a pointwise multiplication of $E(x, y; \lambda_1)$ and the complex conjugate of $E(x, y; \lambda_2)$. Substituting Equation 5.1 into Equation 5.2 gives

$$E(x, y; \Lambda) = A(x, y; \lambda_1)A(x, y; \lambda_2)e^{j[\phi(x, y; \lambda_1) - \phi(x, y; \lambda_2)]} \quad (5.3)$$

For a given geometry/setup, the optical fields for two closely spaced wavelengths λ_1 and λ_2 should be highly correlated as the light at those wavelengths should follow similar paths

¹How close the wavelengths are depends on how long one's synthetic wavelength is. Longer synthetic wavelengths mean that the wavelengths are closer together, and shorter synthetic wavelengths mean that the wavelengths are further apart.

[7]. In fact, difference in phases, i.e. $\phi(x, y; \lambda_1) - \phi(x, y; \lambda_2)$, can potentially contain useful information, as was shown to be the case in [7] and [25]. Note that this difference in phases appears as the phase of the synthetic field, as shown in Equation 5.3.

Moreover, the synthetic field acts as if it has a wavelength of $\Lambda = \frac{\lambda_1 \lambda_2}{|\lambda_1 - \lambda_2|}$ [7]. To illustrate, suppose that $\phi(x, y; \lambda) = \frac{2\pi}{\lambda} d(x, y)$ —this sort of situation came about in [25], where the phase shift was proportional to the surface variation of an object. Then, it follows that

$$\begin{aligned}\phi(x, y; \lambda_1) - \phi(x, y; \lambda_2) &= \frac{2\pi}{\lambda_1} d(x, y) - \frac{2\pi}{\lambda_2} d(x, y) \\ &= 2\pi \left(\frac{\lambda_2 - \lambda_1}{\lambda_1 \lambda_2} \right) d(x, y).\end{aligned}$$

It can be seen that this difference in phases is equal to the phase that one would get if the wavelength λ was equal to $\frac{\lambda_1 \lambda_2}{\lambda_2 - \lambda_1}$. Ignoring the sign and assuming that the wavelength is positive, this situation is as if we have an effective—or *synthetic*—wavelength of $\Lambda = \frac{\lambda_1 \lambda_2}{|\lambda_1 - \lambda_2|}$.

Once the synthetic fields are generated, one can proceed in a number of ways. In [25], the phases of the synthetic fields were analyzed. Since these phases were proportional to path length, the surface variations of measured three-dimensional objects were able to be recovered. In [7], the synthetic fields were backpropagated as if they were waves with wavelengths equal to the synthetic wavelengths. The fields from backpropagation gave images of the measured objects.

It turns out that even though synthetic waves—i.e. backpropagated waves at the synthetic wavelength from a synthetic field—are computational in nature, they still exhibit behavior that is similar to physical waves at the synthetic wavelength [7]. This fact was utilized during the backpropagation step in [7]. Additionally, it was demonstrated in [7] that the synthetic waves appeared to be diffraction-limited in a manner akin to classical waves.

Ultimately, the use of synthetic wavelengths opens up new possibilities. Using measurements from two nearby² wavelengths, one can act as if one has a longer, synthetic

²See Footnote 1.

wavelength [7]. This synthetic wavelength can be orders of magnitude longer than the wavelengths present in one's system, which can allow one to effectively work with a wavelength that is otherwise unattainable in one's system.³ Synthetic wavelengths, by virtue of being longer than the non-synthetic wavelengths, allow one to make measurements that are less sensitive to path length variations [7] [25]. One can also generate synthetic fields that act as if they had a wavelength equal to their corresponding synthetic wavelengths—these fields can be (back)propagated through space, which can allow one to form images in certain cases [7]. The idea of synthetic wavelengths has been used to image through scattering media [7], perform non line-of-sight imaging [7], and measure the three-dimensional surface of optically rough objects with high depth resolution and greater depth range than certain interferometric methods [25].

³For example, a tunable laser would likely not be able to output wavelengths on the order of millimeters, but one can get a synthetic wavelength on the order of millimeters.

Chapter 6

DORT and Synthetic Wavelengths Investigation

6.1 Introduction

This chapter investigates combining DORT and synthetic wavelengths. A particular case is analyzed theoretically, and conclusions are made based off of that analysis and observations from an experiment.

6.2 Main idea and conclusions

One can create synthetic fields that can be backpropagated to form images [7]. In DORT, one obtains singular vectors that can be backpropagated to form images of scatterers under certain circumstances. One might wonder if one could form synthetic singular vectors in a similar way that one forms synthetic fields and if those synthetic singular vectors can be backpropagated to form images.

Section 6.3 provides a mathematical derivation that analyzes this question. Specifically, it analyzes a situation where DORT was performed where there was one scatterer embedded in a homogeneous, dispersionless, isotropic, and unbounded medium. In that case, form-

ing synthetic singular vectors and backpropagating them at the synthetic wavelength—i.e. assuming that the wavelength was the synthetic wavelength—resulted in focusing on the scatterer. This is because all individual contributions from transmitting sources ended up being in-phase at the scatterer.

Similar math to what was done in Section 6.3 should apply in cases with multiple scatterers and where the assumptions behind the equations in Chapter 4 are satisfied. Thus, should the assumptions behind the equations in Chapter 4 be satisfied, and assuming no eigenstructure mixing (see Section 3.5 for more information on eigenstructure mixing), one can expect to see selective focusing with synthetic singular vectors. Even in cases where the assumptions behind the equations in Chapter 4 are only approximately satisfied—e.g. when one has “well-resolved” scatterers instead of “ideally-resolved” scatterers—one can likely still expect to see selective focusing.

Even though the claims in the previous paragraph are not rigorous, possible experimental evidence for the claims is provided later in Section 7.8. Results showing selective focusing with backpropagated synthetic singular vectors is given in that section. Whether or not the behavior seen in Section 7.8 matches up with the theoretical results from Section 6.3 is unknown, but the fact that selective focusing/constructive interference at the scatterers occurs in Section 6.3 appears, on a qualitative and non-rigorous level, to be consistent with the theory from Section 6.3. Regardless, between the theoretical analysis in Section 6.3 and the experimental evidence given in Section 7.8, it can be inferred that one can likely form images of individual scatterers via backpropagating synthetic singular vectors at the synthetic wavelength under certain circumstances.

Finally, it should be noted that this analysis ***does not*** explain or provide theoretical support for the synthetic wavelengths case in Section 8.6.2 as a different method was used for the backpropagation there.

6.3 DORT and synthetic wavelengths derivation

This section (Section 6.3) does a theoretical derivation pertaining to synthetic wavelengths and DORT. Please read Section 6.2 first for the main idea and main conclusions.

6.3.1 Defining a DORT model

Referring to Appendix Section A.1, the Green's function for the (scalar) Helmholtz equation of the form $(\nabla^2 + k^2) U(\vec{r}; \omega) = -4\pi f(\vec{r}; \omega)$ is of the form $G(\vec{r}, \vec{r}_{source}; \omega) = \frac{\exp(+jk\|\vec{r} - \vec{r}_{source}\|)}{\|\vec{r} - \vec{r}_{source}\|}$, where \vec{r}_{source} is the source location. In Appendix Section A.1, a homogeneous, dispersionless, isotropic, and unbounded medium was assumed—therefore, such will also be assumed here.

Now, since k is a wavenumber, it can be written as $n\frac{2\pi}{\lambda}$, where n is the index of refraction. Additionally, one can make $U(\vec{r}; \omega)$, $f(\vec{r}; \omega)$, and $G(\vec{r}, \vec{r}_{source}; \omega)$ functions of λ instead of ω since ω is a function of λ .¹ Making the aforementioned changes gives

$$(\nabla^2 + k^2) U(\vec{r}; \lambda) = -4\pi f(\vec{r}; \lambda) \quad (6.1)$$

as one's differential equation and

$$G(\vec{r}, \vec{r}_{source}; \lambda) = \frac{e^{+jn\frac{2\pi}{\lambda}\|\vec{r} - \vec{r}_{source}\|}}{\|\vec{r} - \vec{r}_{source}\|} \quad (6.2)$$

as the Green's function for a source at \vec{r}_{source} . Note that $G(\vec{r}, \vec{r}_{source}; \lambda)$ satisfies $(\nabla^2 + k^2) G(\vec{r}, \vec{r}_{source}; \lambda) = -4\pi\delta(\vec{r} - \vec{r}_{source})$.

Now, suppose one had a set of sources located at locations $(\vec{r}_j^{(tx)})_{j=1}^N$, a set of observation points at $(\vec{r}_i^{(rx)})_{i=1}^M$, and a pointlike scatterer at the location $\vec{r}^{(scatterer)}$. Now suppose that $f(\vec{r}; \lambda) = \sum_{j=1}^N \tilde{A}_j^{(tx)}(\lambda)\delta(\vec{r} - \vec{r}_j^{(tx)})$. This means that the transmitting elements transmit with amplitudes $(\tilde{A}_j^{(tx)})_{j=1}^N$, where the source at $\vec{r}_j^{(tx)}$ transmits with complex amplitude $\tilde{A}_j(\lambda)$.

¹Note that $\omega = c\frac{2\pi}{\lambda}$, where c is the phase velocity in a vacuum/when the refractive index n is 1.

The situation with the transmitting point sources is the same as the situation encountered in Appendix Section A.2. Thus, following the same logic in Appendix Section A.2, one can write the incident field at point $\vec{r}^{(scatterer)}$ as

$$U_{incident}(\vec{r}^{(scatterer)}, \lambda) = \begin{bmatrix} \frac{\exp(+jn\frac{2\pi}{\lambda}R_1^{(tx)})}{R_1^{(tx)}} & \frac{\exp(+jn\frac{2\pi}{\lambda}R_2^{(tx)})}{R_2^{(tx)}} & \dots & \frac{\exp(+jn\frac{2\pi}{\lambda}R_N^{(tx)})}{R_N^{(tx)}} \end{bmatrix} \begin{bmatrix} \tilde{A}_1(\omega) \\ \tilde{A}_2(\omega) \\ \vdots \\ \tilde{A}_N(\omega) \end{bmatrix}, \quad (6.3)$$

where $R_j^{(tx)} = \left\| \vec{r}^{(scatterer)} - \vec{r}_j^{(tx)} \right\|$. Referring back to the model in Section 3.3, one can let

$$\mathbf{F}(\lambda) = \begin{bmatrix} \frac{\exp(+jn\frac{2\pi}{\lambda}R_1^{(tx)})}{R_1^{(tx)}} & \frac{\exp(+jn\frac{2\pi}{\lambda}R_2^{(tx)})}{R_2^{(tx)}} & \dots & \frac{\exp(+jn\frac{2\pi}{\lambda}R_N^{(tx)})}{R_N^{(tx)}} \end{bmatrix} \quad (6.4)$$

as the row vector on the right-hand side of Equation 6.3 relates the transmitted fields to the incident field on the scatterer. Additionally, again referring back to the model in Section 3.3, one can let

$$\vec{\mathbf{X}}(\lambda) = \begin{bmatrix} \tilde{A}_1(\omega) \\ \tilde{A}_2(\omega) \\ \vdots \\ \tilde{A}_N(\omega) \end{bmatrix} \quad (6.5)$$

as the column vector in Equation 6.3 represents the transmitted signals. Thus, one has

$$U_{incident}(\vec{r}^{(scatterer)}, \lambda) = \mathbf{F}(\lambda) \vec{\mathbf{X}}(\lambda). \quad (6.6)$$

Now, assuming a pointlike scatterer at the location $\vec{r}^{(scatterer)}$ and using the first-order Born approximation, one can model the scattered fields as being produced by an induced point source at the location $\vec{r}^{(scatterer)}$ with an amplitude proportional to the incident field

at the location $\vec{r}^{(scatterer)}$. The scattered field is therefore

$$U_{scattered}(\vec{r}, \lambda) = \tilde{S}(\lambda) U_{incident}(\vec{r}^{(scatterer)}, \lambda) \frac{e^{+jn\frac{2\pi}{\lambda} \|\vec{r} - \vec{r}^{(scatterer)}\|}}{\|\vec{r} - \vec{r}^{(scatterer)}\|} \quad (6.7)$$

where $\tilde{S}(\lambda)$ is a constant relating the incident field to the amplitude of the induced point source at the location $\vec{r}^{(scatterer)}$. Furthermore, substituting Equation 6.6 into Equation 6.7 gives

$$U_{scattered}(\vec{r}, \lambda) = \frac{e^{+jn\frac{2\pi}{\lambda} \|\vec{r} - \vec{r}^{(scatterer)}\|}}{\|\vec{r} - \vec{r}^{(scatterer)}\|} \tilde{S}(\lambda) \mathbf{F}(\lambda) \vec{\mathbf{X}}(\lambda). \quad (6.8)$$

Now, assuming, like what was done in Section 3.3, that the fields from the transmitting sources do not reach the observation points and that only the scattered fields reach the observation points, the fields at the observation points can be listed in a vector as

$$\vec{\mathbf{Y}}(\lambda) = \begin{bmatrix} U_{scattered}(\vec{r}_1^{(rx)}, \lambda) \\ U_{scattered}(\vec{r}_2^{(rx)}, \lambda) \\ \vdots \\ U_{scattered}(\vec{r}_M^{(rx)}, \lambda) \end{bmatrix}. \quad (6.9)$$

Substituting Equation 6.8 into Equation 6.9 gives

$$\vec{\mathbf{Y}}(\lambda) = \begin{bmatrix} \frac{\exp(+jn\frac{2\pi}{\lambda} R_1^{(rx)})}{R_1^{(rx)}} \\ \frac{\exp(+jn\frac{2\pi}{\lambda} R_2^{(rx)})}{R_2^{(rx)}} \\ \vdots \\ \frac{\exp(+jn\frac{2\pi}{\lambda} R_M^{(rx)})}{R_M^{(rx)}} \end{bmatrix} \tilde{S}(\lambda) \mathbf{F}(\lambda) \vec{\mathbf{X}}(\lambda), \quad (6.10)$$

where $R_i^{(rx)} = \|\vec{r}_i^{(rx)} - \vec{r}^{(scatterer)}\|$. Looking at Equation 6.10 and referring back to the model in Section 3.3, the leftmost column vector on the right-hand side of Equation 6.10 is analogous to $\mathbf{B}(\lambda)$ and $\tilde{S}(\lambda)$ is analogous to $\mathbf{S}(\lambda)$. One can construct the model in Section

3.3 with

$$\mathbf{S}(\lambda) = \left[\tilde{S}(\lambda) \right] \quad (6.11)$$

and

$$\mathbf{B}(\lambda) = \begin{bmatrix} \frac{\exp(+jn\frac{2\pi}{\lambda}R_1^{(rx)})}{R_1^{(rx)}} \\ \frac{\exp(+jn\frac{2\pi}{\lambda}R_2^{(rx)})}{R_2^{(rx)}} \\ \vdots \\ \frac{\exp(+jn\frac{2\pi}{\lambda}R_M^{(rx)})}{R_M^{(rx)}} \end{bmatrix}. \quad (6.12)$$

One can now define $\mathbf{H}(\lambda)$ as $\mathbf{H}(\lambda) = \mathbf{B}(\lambda)\mathbf{S}(\lambda)\mathbf{F}(\lambda)$.

6.3.2 Obtaining synthetic singular vectors

Now, assume that $\tilde{S}(\lambda) \neq 0$. Since $\tilde{S}(\lambda) \neq 0$, $\mathbf{B}(\lambda)$ is $M \times 1$ in size, $\mathbf{S}(\lambda)$ is 1×1 in size, and $\mathbf{F}(\lambda)$ is $1 \times N$ in size, and $\mathbf{H}(\lambda) = \mathbf{B}(\lambda)\mathbf{S}(\lambda)\mathbf{F}(\lambda)$, the equations in Chapter 4—i.e. Equation B.24, B.26, B.35, and B.38—are valid.² See Chapter 4 for an overview of the conditions on validity of the equations in that chapter.

Substituting Equation 6.4 into Equation B.24 and writing the equation component-wise, one obtains

$$V_{k,1}(\lambda) = \frac{1}{\sqrt{\sum_{\ell=1}^N \left(\frac{1}{R_\ell^{(tx)}}\right)^2}} \left[\frac{\exp(-jn\frac{2\pi}{\lambda}R_k^{(tx)})}{R_k^{(tx)}} \right] \exp(j\phi_1(\lambda)). \quad (6.13)$$

Note that i in Equation B.24 was replaced by 1 because $\mathbf{F}(\lambda)$ only has one row in this case. Now suppose that one had right-singular vectors at wavelengths λ_1 and λ_2 , where $\lambda_1 < \lambda_2$. Then, one would have $\vec{V}_{*,1}(\lambda_1)$ and $\vec{V}_{*,1}(\lambda_2)$. Using Equation 6.13, performing synthetic

²The single column of $\mathbf{B}(\lambda)$ forms a set consisting of one vector, and that set is mutually orthogonal. and the single row of $\mathbf{F}(\lambda)$ forms a set consisting of one vector, and that set is mutually orthogonal. Therefore, the scatterers are ideally-resolved. Repeated non-zero singular values should also not show up since $\tilde{S}(\lambda) \neq 0$ and $\mathbf{S}(\lambda)$ is 1×1 . Therefore, the equations in Chapter 4—i.e. Equation B.24, B.26, B.35, and B.38—should be valid.

wavelength-style multiplication of the right-singular vectors gives

$$\begin{aligned}
V_{k,1}(\lambda_1)V_{k,1}^*(\lambda_2) &= \left[\frac{\exp(j[\phi_1(\lambda_1) - \phi_1(\lambda_2)])}{\sum_{\ell=1}^N \left(\frac{1}{R_\ell^{(tx)}} \right)^2} \right] \left[\frac{\exp(-jn2\pi \left(\frac{1}{\lambda_1} - \frac{1}{\lambda_2} \right) R_k^{(tx)})}{(R_k^{(tx)})^2} \right] \\
&= \left[\frac{\exp(j[\phi_1(\lambda_1) - \phi_1(\lambda_2)])}{\sum_{\ell=1}^N \left(\frac{1}{R_\ell^{(tx)}} \right)^2} \right] \left[\frac{\exp(-jn2\pi \left(\frac{\lambda_2 - \lambda_1}{\lambda_1 \lambda_2} \right) R_k^{(tx)})}{(R_k^{(tx)})^2} \right] \\
&= \left[\frac{\exp(j[\phi_1(\lambda_1) - \phi_1(\lambda_2)])}{\sum_{\ell=1}^N \left(\frac{1}{R_\ell^{(tx)}} \right)^2} \right] \left[\frac{\exp(-jn \frac{2\pi}{\Lambda} R_k^{(tx)})}{(R_k^{(tx)})^2} \right],
\end{aligned}$$

where $\Lambda = \frac{\lambda_1 \lambda_2}{\lambda_2 - \lambda_1}$ is the synthetic wavelength. Now, writing the expression above in vector form, one obtains

$$\mathbf{V}_{*,1}^{(\Lambda)}(\lambda_1, \lambda_2) = \frac{\exp(j[\phi_1(\lambda_1) - \phi_1(\lambda_2)])}{\sum_{\ell=1}^N \left(\frac{1}{R_\ell^{(tx)}} \right)^2} \begin{bmatrix} \frac{\exp(-jn \frac{2\pi}{\Lambda} R_1^{(tx)})}{(R_1^{(tx)})^2} \\ \frac{\exp(-jn \frac{2\pi}{\Lambda} R_2^{(tx)})}{(R_2^{(tx)})^2} \\ \vdots \\ \frac{\exp(-jn \frac{2\pi}{\Lambda} R_N^{(tx)})}{(R_N^{(tx)})^2} \end{bmatrix} \quad (6.14)$$

where $V_{k,1}^{(\Lambda)}(\lambda_1, \lambda_2) = V_{k,1}(\lambda_1)V_{k,1}^*(\lambda_2)$. $\mathbf{V}_{*,1}^{(\Lambda)}(\lambda_1, \lambda_2)$ is a synthetic right-singular vector.

Substituting Equation 6.12 into Equation B.26 and writing the equation component-wise, one obtains

$$\mathbf{U}_{k,i}(\lambda) = \frac{1}{\sqrt{\sum_{\ell=1}^M \left(\frac{1}{R_\ell^{(rx)}} \right)^2}} \left[\frac{\exp(+jn \frac{2\pi}{\lambda} R_k^{(rx)})}{R_k^{(rx)}} \right] \exp(j\theta_1(\lambda)). \quad (6.15)$$

Now suppose that one had left-singular vectors at wavelengths λ_1 and λ_2 , where $\lambda_1 <$

λ_2 . Then, one would have the singular vectors $\vec{U}_{*,1}(\lambda_1)$ and $\vec{U}_{*,1}(\lambda_2)$. Using Equation 6.15, performing synthetic wavelength-style multiplication of the left-singular vectors gives

$$\begin{aligned} U_{k,1}(\lambda_1)U_{k,1}^*(\lambda_2) &= \left[\frac{\exp(j[\theta_1(\lambda_1) - \theta_1(\lambda_2)])}{\sum_{\ell=1}^M \left(\frac{1}{R_\ell^{(rx)}} \right)^2} \right] \left[\frac{\exp(+jn2\pi \left(\frac{1}{\lambda_1} - \frac{1}{\lambda_2} \right) R_k^{(rx)})}{(R_k^{(rx)})^2} \right] \\ &= \left[\frac{\exp(j[\theta_1(\lambda_1) - \theta_1(\lambda_2)])}{\sum_{\ell=1}^M \left(\frac{1}{R_\ell^{(rx)}} \right)^2} \right] \left[\frac{\exp(+jn2\pi \left(\frac{\lambda_2 - \lambda_1}{\lambda_1 \lambda_2} \right) R_k^{(rx)})}{(R_k^{(rx)})^2} \right] \\ &= \left[\frac{\exp(j[\theta_1(\lambda_1) - \theta_1(\lambda_2)])}{\sum_{\ell=1}^M \left(\frac{1}{R_\ell^{(rx)}} \right)^2} \right] \left[\frac{\exp(+jn \frac{2\pi}{\Lambda} R_k^{(rx)})}{(R_k^{(rx)})^2} \right], \end{aligned}$$

where $\Lambda = \frac{\lambda_1 \lambda_2}{\lambda_2 - \lambda_1}$ is the synthetic wavelength. Writing the expression above in vector form gives

$$\mathbf{U}_{*,1}^{(\Lambda)}(\lambda_1, \lambda_2) = \frac{\exp(j[\theta_1(\lambda_1) - \theta_1(\lambda_2)])}{\sum_{\ell=1}^N \left(\frac{1}{R_\ell^{(rx)}} \right)^2} \begin{bmatrix} \frac{\exp(+jn \frac{2\pi}{\Lambda} R_1^{(rx)})}{(R_1^{(rx)})^2} \\ \frac{\exp(+jn \frac{2\pi}{\Lambda} R_2^{(rx)})}{(R_2^{(rx)})^2} \\ \vdots \\ \frac{\exp(+jn \frac{2\pi}{\Lambda} R_M^{(rx)})}{(R_M^{(rx)})^2} \end{bmatrix} \quad (6.16)$$

where $U_{k,1}^{(\Lambda)}(\lambda_1, \lambda_2) = U_{k,1}(\lambda_1)U_{k,1}^*(\lambda_2)$. $\mathbf{U}_{*,1}^{(\Lambda)}(\lambda_1, \lambda_2)$ is a synthetic left-singular vector.

6.3.3 Backpropagating synthetic singular vectors

One can backpropagate the synthetic singular vectors at the synthetic wavelength Λ . Recall that Equation 6.4 in Subsection 6.3.1 gave an expression for $\mathbf{F}(\lambda)$ and that $\mathbf{F}(\lambda)$ from Equation 6.4 relates transmitted fields to the field incident on the scatterer at $\vec{r}^{(scatterer)}$. One can

substitute $\lambda = \Lambda$ into the expression for $\mathbf{F}(\lambda)$ from Equation 6.4. This gives

$$\mathbf{F}(\Lambda) = \begin{bmatrix} \frac{\exp(+jn\frac{2\pi}{\Lambda}R_1^{(tx)})}{R_1^{(tx)}} & \frac{\exp(+jn\frac{2\pi}{\Lambda}R_2^{(tx)})}{R_2^{(tx)}} & \dots & \frac{\exp(+jn\frac{2\pi}{\Lambda}R_N^{(tx)})}{R_N^{(tx)}} \end{bmatrix}. \quad (6.17)$$

Now suppose that one transmits the synthetic right-singular vector $\mathbf{V}_{*,1}^{(\Lambda)}(\lambda_1, \lambda_2)$ from Equation 6.14 at wavelength Λ from sources located at locations $(\vec{\mathbf{r}}_j^{(tx)})_{j=1}^N$. Specifically, for each $1 \leq j \in \mathbb{Z} \leq N$, the source at $\vec{\mathbf{r}}_j^{(tx)}$ transmits with complex amplitude $\mathbf{V}_{j,1}^{(\Lambda)}(\lambda_1, \lambda_2)$ at wavelength Λ . This is like setting $\vec{\mathbf{X}}(\lambda)$ in Equation 6.6 to $\mathbf{V}_{*,1}^{(\Lambda)}(\lambda_1, \lambda_2)$. From Section 6.3.1 and Equation 6.6, we know that the field incident on the scatterer is therefore $\mathbf{F}(\Lambda)\mathbf{V}_{*,1}^{(\Lambda)}(\lambda_1, \lambda_2)$. Substituting Equations 6.17 and 6.14 into $\mathbf{F}(\Lambda)\mathbf{V}_{*,1}^{(\Lambda)}(\lambda_1, \lambda_2)$ gives

$$U_{incident}^{(tx)}(\vec{\mathbf{r}}^{(scatterer)}, \Lambda) = \frac{\exp(j[\phi_1(\lambda_1) - \phi_1(\lambda_2)])}{\sum_{\ell=1}^N \left(\frac{1}{R_\ell^{(tx)}}\right)^2} \begin{bmatrix} \frac{\exp(+jn\frac{2\pi}{\Lambda}R_1^{(tx)})}{R_1^{(tx)}} & \frac{\exp(+jn\frac{2\pi}{\Lambda}R_2^{(tx)})}{R_2^{(tx)}} & \dots & \frac{\exp(+jn\frac{2\pi}{\Lambda}R_N^{(tx)})}{R_N^{(tx)}} \end{bmatrix} \begin{bmatrix} \frac{\exp(-jn\frac{2\pi}{\Lambda}R_1^{(tx)})}{(R_1^{(tx)})^2} \\ \frac{\exp(-jn\frac{2\pi}{\Lambda}R_2^{(tx)})}{(R_2^{(tx)})^2} \\ \vdots \\ \frac{\exp(-jn\frac{2\pi}{\Lambda}R_N^{(tx)})}{(R_N^{(tx)})^2} \end{bmatrix}, \quad (6.18)$$

where $U_{incident}^{(tx)}(\vec{\mathbf{r}}^{(scatterer)}, \Lambda)$ is the field incident on the scatterer. One can further simplify Equation 6.18 to be³

$$U_{incident}^{(tx)}(\vec{\mathbf{r}}^{(scatterer)}, \Lambda) = \frac{\exp(j[\phi_1(\lambda_1) - \phi_1(\lambda_2)])}{\sum_{\ell=1}^N \left(\frac{1}{R_\ell^{(tx)}}\right)^2} \sum_{k=1}^N \left(\frac{\exp(+jn\frac{2\pi}{\Lambda}R_k^{(tx)})}{R_k^{(tx)}} \right) \left(\frac{\exp(-jn\frac{2\pi}{\Lambda}R_k^{(tx)})}{(R_k^{(tx)})^2} \right), \quad (6.19)$$

³Note that the right-hand side of Equation 6.18 would technically be a one-element matrix whereas the right-hand side of Equation 6.19 is a scalar. This discrepancy is being ignored here as one-element matrices are similar to scalars.

which further simplifies to

$$U_{incident}^{(tx)}(\vec{r}^{(scatterer)}, \Lambda) = \sum_{k=1}^N \left(\frac{\exp(j[\phi_1(\lambda_1) - \phi_1(\lambda_2)])}{\sum_{\ell=1}^N \left(\frac{1}{R_\ell^{(tx)}} \right)^2} \right) \left(\frac{1}{\left(R_k^{(tx)} \right)^3} \right). \quad (6.20)$$

Note that each individual summand in the summation on the right-hand side of Equation 6.20 is the contribution to the total incident field from an individual source. It can be seen that the phase of each of these individual contributions is the same. Therefore, at the scatterer's location ($\vec{r}^{(scatterer)}$), all of the contributions from the various sources are in-phase, thus resulting in constructive interference. Thus, the scatterer is focused on. At other locations, the individual contributions are not guaranteed to be perfectly in-phase, so focusing might not occur at other points.

Now, using the same procedure used to obtain $\mathbf{F}(\lambda)$ in Subsection 6.3.1, one can obtain a matrix that relates the fields transmitted from locations $(\vec{r}_i^{(rx)})_{i=1}^M$. Going through this procedure, it turns out that this matrix is $\mathbf{B}^\top(\lambda)$.

Now suppose that one transmits the *complex conjugate* of the synthetic left-singular vector, i.e. the complex conjugate of $\mathbf{U}_{*,1}^{(\Lambda)}(\lambda_1, \lambda_2)$ from Equation 6.16, at wavelength Λ from sources located at locations $(\vec{r}_i^{(rx)})_{i=1}^M$. To be more specific, for each $1 \leq i \in \mathbb{Z} \leq M$, the source at $\vec{r}_i^{(rx)}$ transmits with complex amplitude $[\mathbf{U}_{i,1}^{(\Lambda)}(\lambda_1, \lambda_2)]^*$ at wavelength Λ . Using similar logic as previously, the field incident on the scatterer in this case is $U_{incident}^{(rx)}(\vec{r}^{(scatterer)}, \Lambda) = \mathbf{B}^\top(\Lambda) [\mathbf{U}_{*,1}^{(\Lambda)}(\lambda_1, \lambda_2)]^*$. Substituting in Equations 6.12 and 6.16

into that expression gives

$$U_{\text{incident}}^{(rx)}(\vec{\mathbf{r}}^{(\text{scatterer})}, \Lambda) = \frac{\exp(j[\theta_1(\lambda_1) - \theta_1(\lambda_2)])}{\sum_{\ell=1}^N \left(\frac{1}{R_\ell^{(rx)}}\right)^2} \begin{bmatrix} \frac{\exp(+jn\frac{2\pi}{\Lambda}R_1^{(rx)})}{R_1^{(rx)}} & \frac{\exp(+jn\frac{2\pi}{\Lambda}R_2^{(rx)})}{R_2^{(rx)}} & \vdots & \frac{\exp(+jn\frac{2\pi}{\Lambda}R_M^{(rx)})}{R_M^{(rx)}} \end{bmatrix} \begin{bmatrix} \frac{\exp(-jn\frac{2\pi}{\Lambda}R_1^{(rx)})}{(R_1^{(rx)})^2} \\ \frac{\exp(-jn\frac{2\pi}{\Lambda}R_2^{(rx)})}{(R_2^{(rx)})^2} \\ \vdots \\ \frac{\exp(-jn\frac{2\pi}{\Lambda}R_M^{(rx)})}{(R_M^{(rx)})^2} \end{bmatrix} \quad (6.21)$$

which can be written as⁴

$$U_{\text{incident}}^{(rx)}(\vec{\mathbf{r}}^{(\text{scatterer})}, \Lambda) = \frac{\exp(j[\theta_1(\lambda_1) - \theta_1(\lambda_2)])}{\sum_{\ell=1}^N \left(\frac{1}{R_\ell^{(rx)}}\right)^2} \sum_{k=1}^M \left(\frac{\exp(+jn\frac{2\pi}{\Lambda}R_k^{(rx)})}{R_k^{(rx)}} \right) \left(\frac{\exp(-jn\frac{2\pi}{\Lambda}R_k^{(rx)})}{(R_k^{(rx)})^2} \right). \quad (6.22)$$

Equation 6.22 simplifies even further to

$$U_{\text{incident}}^{(rx)}(\vec{\mathbf{r}}^{(\text{scatterer})}, \Lambda) = \sum_{k=1}^M \left(\frac{\exp(j[\theta_1(\lambda_1) - \theta_1(\lambda_2)])}{\sum_{\ell=1}^N \left(\frac{1}{R_\ell^{(rx)}}\right)^2} \right) \left(\frac{1}{(R_k^{(rx)})^3} \right). \quad (6.23)$$

Just as with Equation 6.20, the individual summands in Equation 6.23 represent the contribution to the total incident field from individual sources. It can be seen that all of these contributions have the same phase. Thus, constructive interference at the scatterer's location ($\vec{\mathbf{r}}^{(\text{scatterer})}$) occurs. This results in focusing at the position $\vec{\mathbf{r}}^{(\text{scatterer})}$. Note that the individual contributions are not guaranteed to all be in-phase at other points, thus focusing might not occur at other points.

⁴The right-hand side of Equation 6.21 would technically be a one-element matrix whereas the right-hand side of Equation 6.22 is a scalar. This discrepancy is being ignored here as one-element matrices are similar to scalars.

Chapter 7

MATLAB Simulations

NOTE:

Code for the experiments in this chapter (Chapter 7) has been published online. See “[Online Availability](#)” near the beginning of this thesis for more information.

7.1 Introduction

This chapter (Chapter 7) details various MATLAB simulations with conventional DORT and DORT combined with synthetic wavelengths. Although these simulations are limited in accuracy and realism, they nonetheless demonstrate a number of expected phenomena. Perhaps most saliently, the simulations provide evidence for the potential usefulness of combining DORT and synthetic wavelengths.

7.2 Outline of the chapter

This chapter details various experiments in MATLAB pertaining to DORT and DORT combined with synthetic wavelengths. Section 7.3 describes the assumptions behind the various MATLAB simulations. Next, Section 7.4 describes how the transfer matrices going from the transmitting elements to the receiving elements are computed. Then, Section 7.5 describes the results of performing DORT using the transfer matrices. Afterwards, Section 7.6 describes how signals can be backpropagated to form images, and how the information from

DORT can be used to form signals that can be backpropagated to form images.

In Section 7.7, the results of imaging with conventional DORT are detailed. Section 7.8 details the results of imaging with DORT combined with synthetic wavelengths. The results of imaging using DORT with and without synthetic wavelengths when path lengths are aberrated are detailed in Section 7.9. Section 7.10 gives some notes about eigenstructure mixing and eigenstructure demixing, and explains that eigenstructure demixing was not performed and likely not needed for the experiments detailed in Sections 7.8 and 7.9. Finally, Section 7.11 provides some concluding remarks on the MATLAB simulations/experiments.

7.3 Assumptions behind the simulations

The MATLAB simulations start by assuming that one has a set of transmitting elements, a set of receiving elements, and a set of scatterers. It is supposed that the transmitting elements are located at locations $\left(\mathbf{r}_j^{(tx)}\right)_{j=1}^N$, the receiving elements are located at locations $\left(\mathbf{r}_i^{(rx)}\right)_{i=1}^M$, and the scatterers are located at locations $\left(\mathbf{r}_\ell^{(scatterer)}\right)_{\ell=1}^D$. These elements—transmitting elements, receiving elements, and scatterers—are assumed to be pointlike, so their physical dimensions are not considered.

It is also assumed that the medium within which these transmitting elements, receiving elements, and scatterers lie is non-dispersive, homogeneous almost everywhere¹, and unbounded. Additionally, it is assumed that the simulated environments are governed by a scalar wave equation and that all sources emit outgoing waves. No multiple scattering² is supposed, and isotropic scattering that follows the first-order Born approximation is also supposed. Finally, it is assumed that there is no direct coupling between the transmitting and receiving elements, i.e. all energy that reaches the receiving elements from the transmitting elements must have been scattered first.

¹The existence of scatterers implies inhomogeneities, but the scatterers are supposed to be pointlike. Therefore, the inhomogeneities due to the scatterers can be treated as infinitesimally small.

²I.e. scattering that involves waves scattering off of more than one scatterer.

7.4 Computing the transfer matrix

Since the MATLAB simulations simulate non-dispersive, homogeneous, unbounded media where a scalar wave equation applies, one can assume Green's functions of the form

$$G(\vec{r}, \vec{r}_{source}; \lambda) = \frac{e^{+jk\|\vec{r} - \vec{r}_{source}\|}}{\|\vec{r} - \vec{r}_{source}\|}, \quad (\text{A.4})$$

where $k = 2\pi/\lambda$ —for more information on this choice of Green's function, see Appendix Section A.1.³ This Green's function allows one to calculate the field at a given point \vec{r} due to a point source at the point $\vec{r}_j^{(tx)}$. Given the aforementioned Green's function, a point source at the point $\vec{r}_j^{(tx)}$ transmitting with a complex amplitude $\tilde{A}_j(\lambda)$ will produce a field

$$U_j^{(tx)}(\vec{r}; \lambda) = \tilde{A}_j(\lambda) \frac{e^{+jk\|\vec{r} - \vec{r}_j^{(tx)}\|}}{\|\vec{r} - \vec{r}_j^{(tx)}\|}. \quad (7.1)$$

At the scatterer location $\vec{r}_\ell^{(scatterer)}$, the field from Equation 7.1 will be

$$U_j^{(tx)}(\vec{r}_\ell^{(scatterer)}; \lambda) = \tilde{A}_j(\lambda) \frac{e^{+jk\|\vec{r}_\ell^{(scatterer)} - \vec{r}_j^{(tx)}\|}}{\|\vec{r}_\ell^{(scatterer)} - \vec{r}_j^{(tx)}\|}. \quad (7.2)$$

Using the first-order Born approximation, one can generate the scattered fields by imagining an induced point source at the scatterer location with an amplitude that is proportional to the incident field at the scatterer location—in this case, the incident field at the scatterer location would be $U_j^{(tx)}(\vec{r}_\ell^{(scatterer)}; \lambda)$. Then, the scattered field from a scatterer at $\vec{r}_\ell^{(scatterer)}$ would be of the form

$$\begin{aligned} U_{\ell,j}^{(scattered)}(\vec{r}; \lambda) &= \tilde{S}_\ell(\lambda) U_j^{(tx)}(\vec{r}_\ell^{(scatterer)}; \lambda) \frac{e^{+jk\|\vec{r} - \vec{r}_\ell^{(scatterer)}\|}}{\|\vec{r} - \vec{r}_\ell^{(scatterer)}\|} \\ &= \tilde{S}_\ell(\lambda) \left(\tilde{A}_j(\lambda) \frac{e^{+jk\|\vec{r}_\ell^{(scatterer)} - \vec{r}_j^{(tx)}\|}}{\|\vec{r}_\ell^{(scatterer)} - \vec{r}_j^{(tx)}\|} \right) \frac{e^{+jk\|\vec{r} - \vec{r}_\ell^{(scatterer)}\|}}{\|\vec{r} - \vec{r}_\ell^{(scatterer)}\|}, \end{aligned} \quad (7.3)$$

³A slight notational change from Appendix Section A.1 was made. Namely, ω was replaced with λ since λ is usually used more than ω when dealing with optics.

where $\tilde{S}_\ell(\lambda)$ is a complex number relating the incident field on the ℓ^{th} scatterer to the amplitude of the source induced by the incident field at scatterer location $\vec{r}_\ell^{(\text{scatterer})}$. **Note that isotropic scatterers/isotropic scattering is assumed here**, which is not necessarily physically accurate. Now, at receiver location $\vec{r}_i^{(rx)}$, the scattered field given in Equation 7.3 would be

$$\begin{aligned} U_{\ell,j}^{(\text{scattered})} \left(\vec{r}_i^{(rx)}; \lambda \right) &= \tilde{S}_\ell(\lambda) U_j^{(tx)} \left(\vec{r}_\ell^{(\text{scatterer})}; \lambda \right) \frac{e^{+jk\|\vec{r}_i^{(rx)} - \vec{r}_\ell^{(\text{scatterer})}\|}}{\|\vec{r}_i^{(rx)} - \vec{r}_\ell^{(\text{scatterer})}\|} \\ &= \tilde{S}_\ell(\lambda) \left(\tilde{A}_j(\lambda) \frac{e^{+jk\|\vec{r}_\ell^{(\text{scatterer})} - \vec{r}_j^{(tx)}\|}}{\|\vec{r}_\ell^{(\text{scatterer})} - \vec{r}_j^{(tx)}\|} \right) \frac{e^{+jk\|\vec{r}_i^{(rx)} - \vec{r}_\ell^{(\text{scatterer})}\|}}{\|\vec{r}_i^{(rx)} - \vec{r}_\ell^{(\text{scatterer})}\|}. \end{aligned} \quad (7.4)$$

However, since there are multiple scatterers, one will get multiple scattered fields when transmitting at location $\vec{r}_j^{(tx)}$. Thus, the actual field at receiver location $\vec{r}_i^{(rx)}$ when transmitting at location $\vec{r}_j^{(tx)}$ would be the sum of scattered fields, i.e.

$$\begin{aligned} U_{i,j}^{(rx)} (\lambda) &= \sum_{\ell=1}^D \tilde{S}_\ell(\lambda) U_j^{(tx)} \left(\vec{r}_\ell^{(\text{scatterer})}; \lambda \right) \frac{e^{+jk\|\vec{r}_i^{(rx)} - \vec{r}_\ell^{(\text{scatterer})}\|}}{\|\vec{r}_i^{(rx)} - \vec{r}_\ell^{(\text{scatterer})}\|} \\ &= \sum_{\ell=1}^D \tilde{S}_\ell(\lambda) \left(\tilde{A}_j(\lambda) \frac{e^{+jk\|\vec{r}_\ell^{(\text{scatterer})} - \vec{r}_j^{(tx)}\|}}{\|\vec{r}_\ell^{(\text{scatterer})} - \vec{r}_j^{(tx)}\|} \right) \frac{e^{+jk\|\vec{r}_i^{(rx)} - \vec{r}_\ell^{(\text{scatterer})}\|}}{\|\vec{r}_i^{(rx)} - \vec{r}_\ell^{(\text{scatterer})}\|}. \end{aligned} \quad (7.5)$$

Equation 7.5 above gives the received field at receiver location $\vec{r}_i^{(rx)}$ when transmitting at location $\vec{r}_j^{(tx)}$. **Note that multiple scattering is not modeled here, and that it is assumed that only single scattering occurs. Also note that it is assumed that direct coupling between the transmitting and receiving elements is non-existent, i.e. that any wave that reaches the receiving elements from the transmitting elements must have been scattered first.** These assumptions are not necessarily physically accurate.

Letting $\tilde{A}_j(\lambda) = 1$ for all λ in Equation 7.5 gives the element in the i^{th} row and j^{th} column of the transfer matrix $\mathbf{H}(\lambda)$ (see Section 2.3 for more information on transfer matrices). This is because the element at the i^{th} row and j^{th} column of the transfer matrix is the response

received at the i^{th} receiving element/location i given an impulse in the time domain (which becomes a constant 1 in the frequency domain) at transmitting element/location j , and letting $\tilde{A}_j(\lambda) = 1$ gives this impulse response. Therefore, one can express the transfer matrix element-wise as⁴

$$H_{i,j}(\lambda) = \sum_{\ell=1}^D \tilde{S}_\ell(\lambda) \left(\frac{e^{+jn\frac{2\pi}{\lambda}\|\bar{\mathbf{r}}_\ell^{(\text{scatterer})} - \bar{\mathbf{r}}_j^{(tx)}\|}}{\|\bar{\mathbf{r}}_\ell^{(\text{scatterer})} - \bar{\mathbf{r}}_j^{(tx)}\|} \right) \left(\frac{e^{+jn\frac{2\pi}{\lambda}\|\bar{\mathbf{r}}_i^{(rx)} - \bar{\mathbf{r}}_\ell^{(\text{scatterer})}\|}}{\|\bar{\mathbf{r}}_i^{(rx)} - \bar{\mathbf{r}}_\ell^{(\text{scatterer})}\|} \right). \quad (7.6)$$

Note that Equation 7.6 was obtained by substituting $\tilde{A}_j(\lambda) = 1$ for all λ and $k = n(2\pi/\lambda)$ for all λ into Equation 7.5, where n is the refractive index of the medium.

The MATLAB simulations compute the transfer matrix using the formula given in Equation 7.6. The transfer matrices were computed for discrete wavelengths, i.e. discrete λ . Since there are M receiving element locations and N transmitting element locations, for each wavelength, the corresponding transfer matrix is $M \times N$ in size.⁵

7.5 Performing DORT

Recall from Section 3.3 that DORT can be performed via taking the singular value decomposition (SVD) of a transfer matrix $\mathbf{H}(\lambda)$. Since the transfer matrix $\mathbf{H}(\lambda)$ is computed for discrete wavelengths in the manner described in Section 7.4, one can perform DORT by taking the SVD of the computed transfer matrices.

Specifically, each wavelength has its own corresponding transfer matrix, and for each wavelength, the SVD of the corresponding transfer matrix is taken. Since each transfer matrix is $M \times N$ in size, from each singular value decomposition, one gets an $M \times M$ matrix \mathbf{U} whose columns are left-singular vectors, an $M \times N$ diagonal matrix Σ whose diagonal entries are the singular values, and an $N \times N$ matrix \mathbf{V} whose columns are right-singular vectors. If one has Q discrete wavelengths, then there will be Q different \mathbf{U} matrices,

⁴Equation 7.6 is similar to the equation for $H_{ij}(\omega)$ in [26]. [26] considers the case where the transmitting and receiving elements are the same, however.

⁵To improve computation speed, the transfer matrix computation is vectorized and performed on a GPU.

Q different Σ matrices, and Q different \mathbf{V} matrices. In the actual code, these matrices are stored in three-dimensional arrays where the first two dimensions are the rows and columns, and the last dimension corresponds to the wavelength.

7.6 Backpropagating fields

7.6.1 Backpropagating arbitrary fields

One can simulate transmitting fields from a set of points. Suppose one has a set of point sources at locations $(\vec{\mathbf{r}}_i)_{i=1}^{N_{elements}}$ that transmit with respective complex amplitudes $(\tilde{\mathbf{A}}_i(\lambda))_{i=1}^{N_{elements}}$, i.e. for each i , the point source at $\vec{\mathbf{r}}_i$ transmits a sinusoidal signal with an amplitude and phase equal to the magnitude and phase of $A_i(\lambda)$ respectively. Finally, suppose that these point sources are embedded in a homogeneous, dispersionless, isotropic, and unbounded medium, and that the point sources all act like sources and not sinks.

Referring to Appendix Section A.2, one can write the differential equation $(\nabla^2 + k^2) U(\vec{\mathbf{r}}; \lambda) = -4\pi \sum_{i=1}^{N_{elements}} \tilde{A}_i(\lambda) \delta(\vec{\mathbf{r}} - \vec{\mathbf{r}}_i)$ to describe this situation.⁶ Additionally, referring to Appendix Section A.2 again, under the assumptions given earlier in this section (Section 7.6.1), one obtains the field⁷

$$U(\vec{\mathbf{r}}, \lambda) = \sum_{i=1}^{N_{elements}} \tilde{A}_i(\lambda) \frac{\exp(+jn\frac{2\pi}{\lambda} \|\vec{\mathbf{r}} - \vec{\mathbf{r}}_i\|)}{\|\vec{\mathbf{r}} - \vec{\mathbf{r}}_i\|}, \quad (7.7)$$

which can be computed numerically⁸. One can define the transmitted signals $(\tilde{\mathbf{A}}_i(\lambda))_{i=1}^{N_{elements}}$ with a vector of length $N_{elements}$, i.e. a vector in $\mathbb{C}^{N_{elements}}$, where $N_{elements}$ is the number of elements being used for transmitting. For each $1 \leq i \in \mathbb{Z} \leq N$, the i^{th} component of the vector becomes $\tilde{A}_i(\lambda)$.

⁶Note that ω was replaced with λ here.

⁷Equation 7.7 comes from Equation A.7. Note that the substitution $k = n(2\pi/\lambda)$ was made into Equation A.7, where n is the index of refraction.

⁸This computation can be done in a vectorized manner on a GPU. Doing so results in a faster computation.

7.6.2 DORT and backpropagation

One can use the general framework given in Subsection 7.6.1 to backpropagate fields using information obtained from DORT. In the case of DORT, one can use the singular vectors obtained from DORT to define signals to transmit. It can be noted that the right- and left-singular vectors from DORT will have dimensions equal to the number of transmitting and receiving transducers respectively—this is no coincidence, as these singular vectors come from taking the SVD of the transfer matrix $\mathbf{H}(\lambda)$, which relates the fields transmitted by the transmitting transducers to the fields incident on the receiving transducers.

The right-singular vectors can be used to define signals transmitted from the transmitting transducer locations $(\vec{\mathbf{r}}_j^{(tx)})_{j=1}^N$. The components of a given right-singular vector can be used to define the amplitudes and phases of sinusoidal signals transmitted by the transmitting transducers at those aforementioned locations. To be more specific, referring back to the general framework given in Subsection 7.6.1, the $(\vec{\mathbf{r}}_i)_{i=1}^{N_{elements}}$ seen in Equation 7.7 become the transmitting transducer locations $(\vec{\mathbf{r}}_j^{(tx)})_{j=1}^N$, and the $(\vec{\mathbf{A}}_i(\lambda))_{i=1}^{N_{elements}}$ seen in Equation 7.7 become the components of the given right-singular vector. Finally, making these substitutions into Equation 7.7 gives one an image in the form of a field.

Similarly, the complex conjugates of the left-singular vectors can be used to define signals transmitted from the receiving transducer locations $(\vec{\mathbf{r}}_i^{(rx)})_{i=1}^M$. The complex-conjugated components of a given left-singular vector can be used to define the amplitudes and phases of sinusoidal signals emitted by the receiving transducers. To be more specific, referring back to the general framework given in Subsection 7.6.1, the $(\vec{\mathbf{r}}_i)_{i=1}^{N_{elements}}$ seen in Equation 7.7 become the receiving transducer locations $(\vec{\mathbf{r}}_i^{(rx)})_{i=1}^M$, and the $(\vec{\mathbf{A}}_i(\lambda))_{i=1}^{N_{elements}}$ seen in Equation 7.7 become the complex conjugates of the components of the given left-singular vector. Finally, similarly to before, making these substitutions into Equation 7.7 gives one an image in the form of a field.

7.6.3 Backpropagating at synthetic wavelengths

It turns out that one can apply the concept of synthetic wavelengths to DORT in order to aid with imaging. This can be done if one acquires transfer matrices for two separate wavelengths, which shall be denoted as λ_1 and λ_2 , where $\lambda_1 < \lambda_2$. Performing DORT, i.e. taking the SVD of those transfer matrices, gives one a set of left-singular vectors, right-singular vectors, and singular values for each wavelength.

Now, supposing that the right-singular vectors $\mathbf{V}_{*,i}(\lambda_1)$ and $\mathbf{V}_{*,i}(\lambda_2)$ correspond to the same scatterer and scattering pattern⁹, then one can create a synthetic right-singular vector $\mathbf{V}_{*,i}^{(\Lambda)}$ via the formula

$$\mathbf{V}_{*,i}^{(\Lambda)} = \mathbf{V}_{*,i}(\lambda_1) \odot \mathbf{V}_{*,i}^*(\lambda_2), \quad (7.8)$$

where \odot denotes element-wise multiplication and the superscript * denotes complex conjugation. Similarly, supposing that the left-singular vectors $\mathbf{U}_{*,i}(\lambda_1)$ and $\mathbf{U}_{*,i}(\lambda_2)$ correspond to the same scatterer and scattering pattern¹⁰, then one can create a synthetic left-singular vector $\mathbf{U}_{*,i}^{(\Lambda)}$ via the formula

$$\mathbf{U}_{*,i}^{(\Lambda)} = \mathbf{U}_{*,i}(\lambda_1) \odot \mathbf{U}_{*,i}^*(\lambda_2). \quad (7.9)$$

The synthetic singular vectors can be backpropagated to form images in a similar manner to what was described in Subsection 7.6.2. The right-singular vectors $\mathbf{V}_{*,i}^{(\Lambda)}$ will define signals that the transmitting transducers transmit, and the complex conjugates of the left-singular vectors $\mathbf{U}_{*,i}^{(\Lambda)}$ will define signals that the receiving transducers transmit. The main difference, however, is that *the backpropagation will occur at the synthetic wavelength*, i.e. at the wavelength $\lambda = \Lambda = \frac{\lambda_1 \lambda_2}{|\lambda_1 - \lambda_2|}$. This means that λ in Equation 7.7 will be equal to Λ .

Note that not all singular values will correspond to a scatterer—these singular values have values that are either extremely close to zero or actually zero. It has been empirically observed by the author of this thesis that singular vectors corresponding to singular values that do not correspond to any scatterers likely cannot be used to form useful synthetic

⁹The term “scattering pattern” is being used in the manner that [16] used the term.

¹⁰See Footnote 9.

singular vectors—these synthetic singular vectors do not appear to form useful images when backpropagated.¹¹

Finally, as an aside, it is possible for a scatterer to have multiple singular values corresponding to it [16] [19] and that these singular values can correspond to different scattering patterns¹² of the scatterer [16].¹³ The author of this thesis is unsure what would happen if one formed synthetic singular vectors from singular vectors corresponding to the same scatterer but different scattering patterns, therefore the qualification “correspond to the same ... scattering pattern” was made earlier in this section (Section 7.6.3).

7.7 Imaging experiment with DORT at single wavelengths

Under the assumptions given in Section 7.3, a transfer matrix $\mathbf{H}(\lambda)$ can be computed using Equation 7.6. DORT can be performed by taking the SVD of the transfer matrix $\mathbf{H}(\lambda)$. Afterwards, singular vectors can be backpropagated in the manner described in Subsection 7.6.2.

This procedure is implemented in a MATLAB experiment. The experiment is done in two dimensions. In the experiment, two arrays, one transmitting and one receiving, are placed 50 mm apart, with both arrays being parallel to the x-axis. Each array has 1920 elements spaced $6.4 \mu\text{m}$ apart, which was chosen to be consistent with the HOLOEYE LETO spatial light modulator’s specifications.¹⁴ The medium contains two scatterers, each located approximately halfway between the transmitting and receiving arrays at coordinates

¹¹It should be noted however that singular vectors that do not correspond to scatterers can be useful. Specifically, TR-MUSIC [19] [26] makes use of these singular vectors for imaging.

¹²See Footnote 9.

¹³It has been noted in the literature, e.g. [16] and [19], that multiple singular values can correspond to a single scatterer. [16] seems to imply that these singular values that correspond to the same scatterer correspond to different scattering patterns of the same scatterer. [19] states that “more than one eigenvalue may be associated with a single scatterer” for “non-isotropic scattering”—note that the eigenvalues mentioned here correspond to singular values of the transfer matrix.

¹⁴As an aside, a HOLOEYE LETO spatial light modulator was used in [25].

(−6.1 mm, 24 mm) and (12.9 mm, 26 mm).¹⁵ For both scatterers, $\tilde{S}_\ell(\lambda)$ is 1×10^{-6} (see Section 7.4 for the definition of $\tilde{S}_\ell(\lambda)$). Additionally, the medium has a refractive index of 1.

Using Equation 7.6, a transfer matrix $\mathbf{H}(\lambda)$ is computed for wavelengths $\lambda_1 = 1200$ nm and $\lambda_2 \approx 1214.57$ nm. The SVD is taken twice, once for each transfer matrix: $\mathbf{H}(\lambda_1 = 1200 \text{ nm})$ and $\mathbf{H}(\lambda_2 \approx 1214.57 \text{ nm})$. Backpropagation of singular vectors is performed in the manner described in Subsection 7.6.2 for singular vectors at each wavelength.

Figure 7.1 shows the results of backpropagation at the wavelength $\lambda_1 = 1200$ nm. It can be seen that when backpropagated, the first singular vectors—left and right—selectively focus on the scatterer on the left and the second singular vectors—left and right—selectively focus on the scatterer on the right. The same can be observed for Figure 7.2, which shows the results of backpropagation at the wavelength $\lambda_2 \approx 1214.57$ nm.

This selective focusing behavior is consistent with the selective focusing behavior that DORT has been widely documented to show [4] [18] [19] [20] [21]. Backpropagating singular vectors from DORT gives fields that reach their maximum around particular scatterers [4] [19] [20].¹⁶ This behavior can be seen in Figures 7.1 and 7.2. However, it is difficult to make out where the scatterers are based on the areas where the fields are focused in those figures. This is because the array elements are spaced more than half of a wavelength apart, which creates spatial aliasing—thus, the fields seem to focus at multiple spots and it is difficult to visually tell where the scatterers may be.¹⁷

¹⁵As an aside, the array locations in these experiments, which can be seen in Figures 7.1 and 7.2, might suggest the possibility of some degree of direct coupling between the transmitting and receiving transducers, i.e. some waves might theoretically be able to travel directly from the transmitting transducers to the receiving transducers—this fact is ignored in these experiments. Additionally, multiple scattering, i.e. waves scattering off multiple scatterers, is also ignored in these experiments.

¹⁶[4], [19], and [20] discuss selective focusing using singular vectors over a band of frequencies. However, the selective focusing should apply for individual frequencies as a given focusing signal that spans a band of frequencies will consist of individual components at single frequencies, and each single frequency should exhibit selective focusing behavior in order for the entire signal to exhibit selective focusing behavior (the power received by a scatterer at one frequency should be independent of the other frequencies). Additionally, it can be seen from the MATLAB experiments (Figures 7.1 and 7.2) that focusing with DORT at single frequency does, in fact, work.

¹⁷It can be noted though that closer inspection of Figures 7.1 and 7.2 shows that the focusing is the strongest at the locations of the scatterers. However, this may not be apparent from a cursory visual inspection.

DORT Singular Vector Backpropagation

$\lambda = 1200.00\text{nm}$

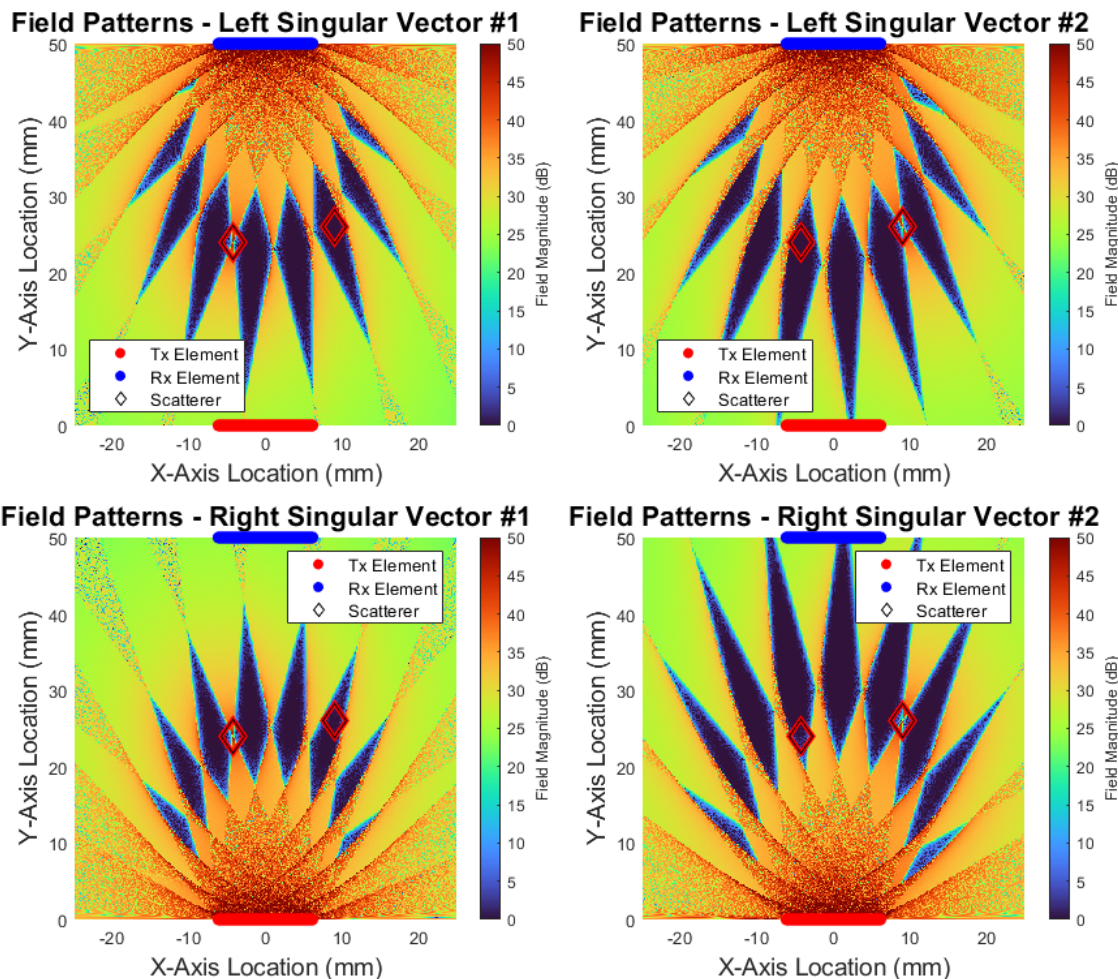


Figure 7.1: Selective focusing on scatterers with DORT at a non-synthetic wavelength ($\lambda = 1200 \text{ nm}$)

DORT Singular Vector Backpropagation

$\lambda \approx 1214.57\text{nm}$

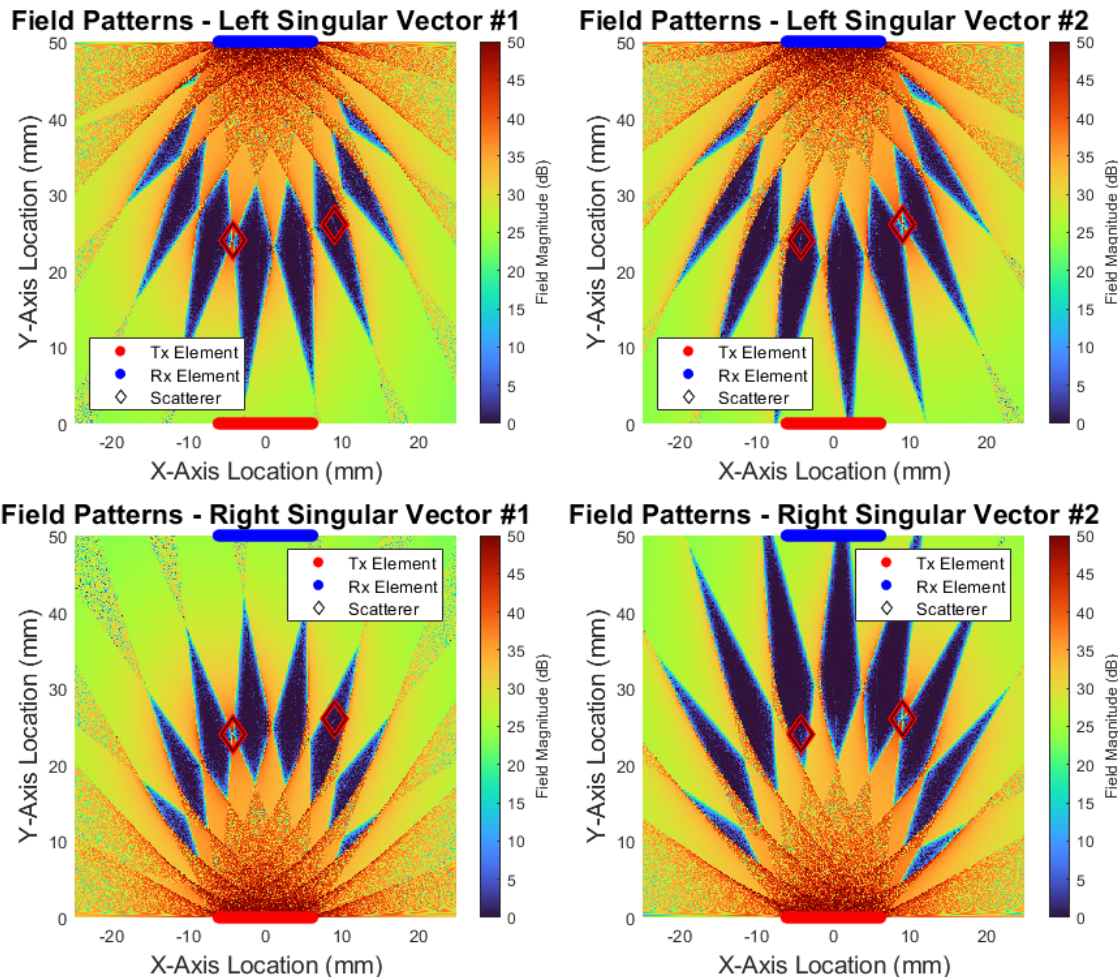


Figure 7.2: Selective focusing on scatterers with DORT at a non-synthetic wavelength ($\lambda \approx 1214.57\text{ nm}$)

7.8 Imaging experiment with DORT and synthetic wavelengths

The same setup that is used for the single wavelength DORT experiments described in Section 7.7 is used to test the use of synthetic wavelengths. Moreover, minus the backpropagation, the procedure described in Section 7.7 is also followed for this experiment—as DORT is performed for wavelengths $\lambda_1 = 1200\text{ nm}$ and $\lambda_2 \approx 1214.57\text{ nm}$, two sets of left-singular vectors, right-singular vectors, and singular values are obtained for the transfer matrices at wavelengths $\lambda_1 = 1200\text{ nm}$ and $\lambda_2 \approx 1214.57\text{ nm}$.

The aforementioned singular vectors are used to form images in the manner described in Subsection 7.6.3. In this case, the i^{th} singular vector at one wavelength was paired with the i^{th} singular vector at the other wavelength, where $i \in \{1, 2\}$.¹⁸ The wavelengths used in the experiments described in Section 7.7 give a synthetic wavelength¹⁹ of $\Lambda = 0.10\text{ mm}$, so a synthetic wavelength of $\Lambda = 0.10\text{ mm}$ is used.

Figure 7.3 shows the results of backpropagating synthetic singular vectors at the synthetic wavelength. It can be seen that selective focusing on scatterers occurs. Furthermore, the spatial aliasing that occurred in Figures 7.1 and 7.2 is not present—this is to be expected as unlike the non-synthetic wavelengths, the inter-element spacing of $6.4\text{ }\mu\text{m}$ is less than half of the synthetic wavelength of $\Lambda = 0.10\text{ mm}$.²⁰

¹⁸See Section 7.10 for a note on eigenstructure mixing.

¹⁹Recall that the synthetic wavelength is given by $\Lambda = \frac{\lambda_1 \lambda_2}{|\lambda_1 - \lambda_2|}$.

²⁰Inter-element spacing should be less than half of a wavelength long to prevent spatial aliasing.

DORT Synthetic Singular Vector Backpropagation

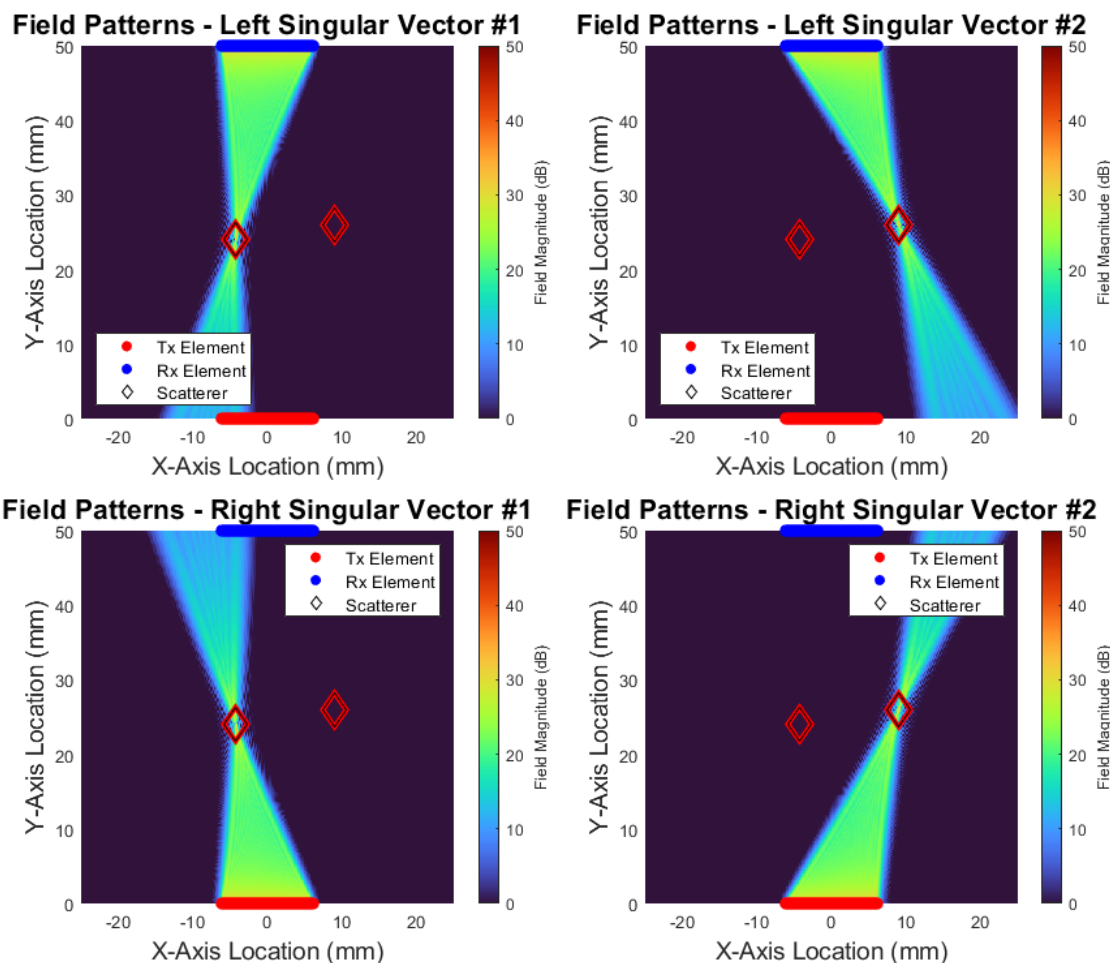
$$\Lambda_{\text{synth}} = 0.10 \text{mm} - \lambda_1 = 1200.00 \text{nm}, \lambda_2 \approx 1214.57 \text{nm}$$


Figure 7.3: Selective focusing on scatterers with DORT using a synthetic wavelength ($\Lambda = 0.10 \text{ mm}$)

7.9 Aberrated path length imaging experiment

One of the advantages of using synthetic wavelengths is that there can be less sensitivity to aberrations in path length [7] [25]. To test the resiliency of synthetic wavelengths to path length variations in the context of DORT, the performance of imaging via DORT and backpropagation in the presence of path length variations is examined. The results obtained when not using a synthetic wavelength are compared to the results obtained when using a synthetic wavelength.

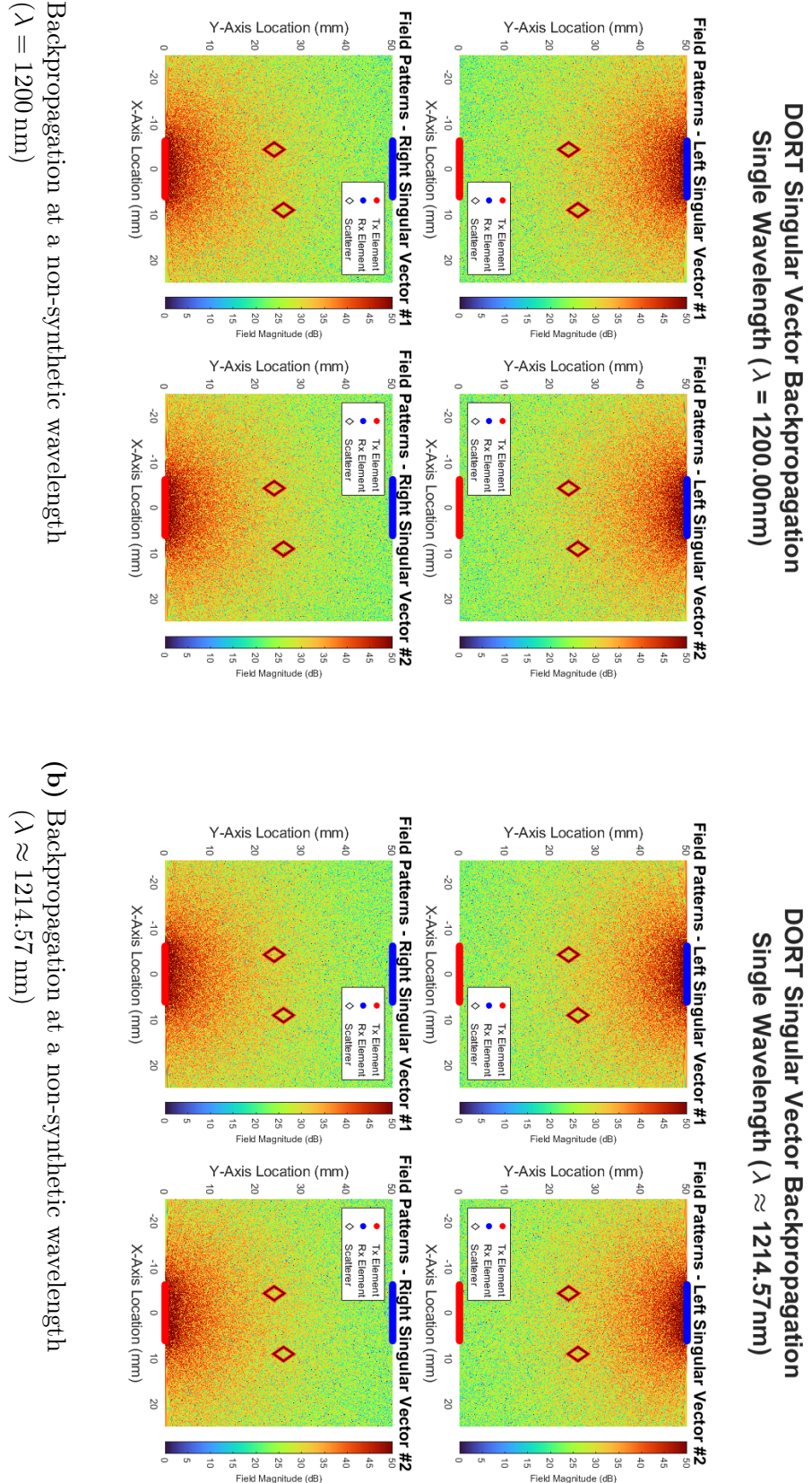
Once again, the setup that is used for the single wavelength DORT experiments described in Section 7.7 is used here. The experiments in Sections 7.7 and 7.8 are repeated, except this time path length variations are added while calculating the transfer matrix. Specifically, random variations that are uniformly distributed²¹ from $-25\text{ }\mu\text{m}$ to $+25\text{ }\mu\text{m}$ are added to the $\|\vec{\mathbf{r}}_{\ell}^{(\text{scatterer})} - \vec{\mathbf{r}}_j^{(tx)}\|$ and $\|\vec{\mathbf{r}}_i^{(rx)} - \vec{\mathbf{r}}_{\ell}^{(\text{scatterer})}\|$ terms in Equation 7.6.²² The backpropagation step remains unchanged.

The results of repeating the experiments in Sections 7.7 and 7.8 with aberrated path lengths are shown in Figures 7.4 and 7.5 respectively. It can be seen in Figure 7.4 that the images from backpropagation are essentially noise, and one cannot see any selective focusing behavior. In contrast, one still sees selective focusing behavior in Figure 7.5. Some small aberrations in the fields can be seen relative to what is shown in Figure 7.3, in which there were no random path length variations. However, the fields from backpropagation are still mostly intact, and images of the scatterers can be seen.²³

²¹These numbers are generated by subtracting 0.5 from MATLAB's `rand(...)` function and multiplying the result by `50e-6`.

²²It can be noted that $\|\vec{\mathbf{r}}_{\ell}^{(\text{scatterer})} - \vec{\mathbf{r}}_j^{(tx)}\|$ and $\|\vec{\mathbf{r}}_i^{(rx)} - \vec{\mathbf{r}}_{\ell}^{(\text{scatterer})}\|$ show up multiple times in Equation 7.6. To clarify, for a given ℓ and j , the same random variation is added to each occurrence of $\|\vec{\mathbf{r}}_{\ell}^{(\text{scatterer})} - \vec{\mathbf{r}}_j^{(tx)}\|$. For a given i and ℓ , the same random variation is added to each occurrence of $\|\vec{\mathbf{r}}_i^{(rx)} - \vec{\mathbf{r}}_{\ell}^{(\text{scatterer})}\|$.

²³See Section 7.10 for a note on eigenstructure mixing.



(a) Backpropagation at a non-synthetic wavelength
($\lambda = 1200\text{nm}$)

Figure 7.4: Demonstration showing how backpropagating singular vectors from DORT can fail to create images in the presence of path length variations

DORT Synthetic Singular Vector Backpropagation

$\Lambda_{\text{synth}} = 0.10\text{mm} - \lambda_1 = 1200.00\text{nm}, \lambda_2 \approx 1214.57\text{nm}$

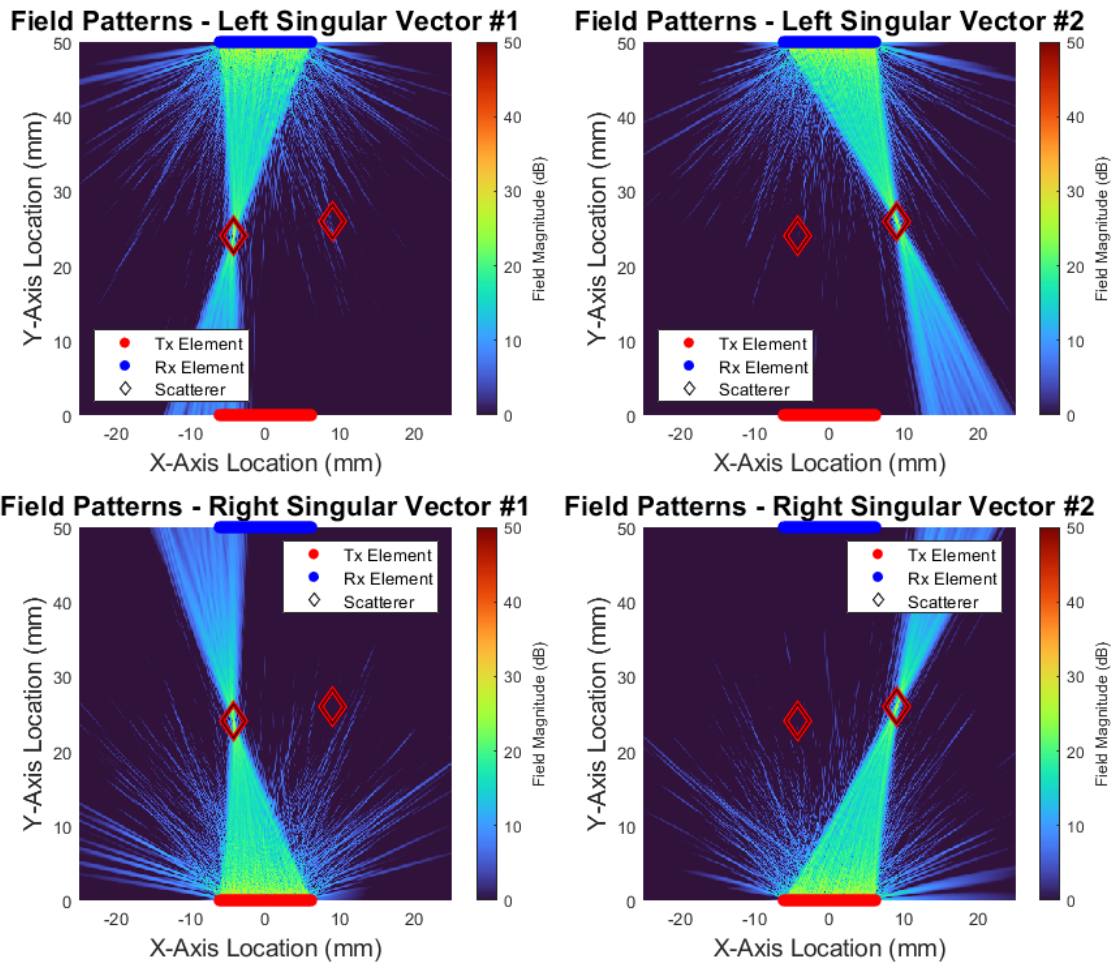


Figure 7.5: Demonstration showing how backpropagating synthetic singular vectors from DORT can create images despite path length variations

7.10 A note on eigenstructure mixing

By looking at Figures 7.1 and 7.2, it can be seen that same-numbered singular vectors correspond to the same scatterer across wavelengths as the backpropagated fields from a given singular vector number all focus on the same scatterer. There also appear to only be one scattering pattern per scatterer as for each wavelength, there are only two singular values that were not near zero, and there are only two scatterers, which likely each correspond to a single singular value²⁴ (see Subsection 7.6.3 for more information on scattering patterns and having multiple singular values per scatterer). Therefore, it can be assumed that the i^{th} singular vectors where $i \in \{1, 2\}$ correspond to the same scatterer and scattering pattern across wavelengths in the experiment described in Section 7.8. This is consistent with what was supposed in Subsection 7.6.3.

Put differently, there does not appear to be any eigenstructure mixing (see Section 3.5 for more information on eigenstructure mixing and eigenstructure demixing) in the experiment described in Section 7.8. There is likely no need to perform any sort of eigenstructure demixing in the experiment described in Section 7.8, and no eigenstructure demixing is performed in the experiment described in Section 7.8.

Furthermore, no eigenstructure demixing (see Section 3.5 for more information on eigenstructure mixing and eigenstructure demixing) was done in the synthetic wavelengths experiment detailed in Section 7.9. Seeing as selective focusing behavior was observed in Figure 7.5, it does not appear that eigenstructure demixing was needed in experiment detailed in Section 7.9, and no eigenstructure demixing is performed in experiment detailed in Section 7.9.

Note that the code for the experiments detailed in this Sections 7.8 and 7.9 does not contain any eigenstructure demixing code. More generally, the code for this chapter (Chapter

²⁴One can consider the fact that each scatterer is focused on once in Figure 7.1. The same holds for Figure 7.2. Thus, in each of those cases, it is likely that each scatterer had one corresponding singular value. The singular values near zero probably do not correspond to any particular scatterer, as can be inferred from [26] and [19].

[7](#)) does not include any eigenstructure demixing code. Thus, performing eigenstructure demixing is not an option for the experiments in this chapter (Chapter [7](#)), at least not as the code was at the time of this writing.²⁵

7.11 Summary and observations

In this chapter (Chapter [7](#)), a number of MATLAB experiments were detailed. Based on these experiments, it appears that using DORT with synthetic wavelengths appears to have a number of advantages over conventional DORT.

One advantage of using synthetic wavelengths appears to be that one can avoid spatial aliasing in the images that one forms via backpropagation of singular vectors from DORT. With synthetic wavelengths, one can ensure that the spacing between one's transducer elements is less than half of a synthetic wavelength, thus avoiding spatial aliasing. This can result in better, less ambiguous images.²⁶

Another advantage is that using synthetic wavelengths seems to provide some resilience to path length variations. At non-synthetic wavelengths, path length aberrations can destroy one's images.²⁷ In contrast, one can still potentially obtain images in the presence of path length aberrations using synthetic wavelengths.²⁸ Path length aberrations can occur when imaging through scattering media [[7](#)], so the ability to ignore path length aberrations can be useful for imaging through scattering media.

Ultimately, although the MATLAB experiments detailed in this chapter (Chapter [7](#)) were not detailed simulations, they may still be indicative of how conventional DORT and DORT with synthetic wavelengths behave. In the context of sampling theory, the lack of spatial aliasing when using a synthetic wavelength that is longer than twice the spacing

²⁵See “[Online Availability](#)” near the beginning of this thesis for more information on the code for the experiments done in Chapter [7](#).

²⁶Compare Figures [7.1](#) and [7.2](#), which show backpropagation at non-synthetic wavelengths with Figure [7.3](#), which shows backpropagation at synthetic wavelengths.

²⁷See Figure [7.4](#).

²⁸See Figure [7.5](#).

between elements is not surprising. Furthermore, the resiliency of synthetic wavelengths to path length variations has been documented in [7] and [25], so seeing further experimental confirmation of this resiliency is not at odds with what has already been shown. Thus, at the very least, the MATLAB experiments are in line with what is expected, and at best, the experiments may be a reasonable approximation of reality, although such is not guaranteed.

Chapter 8

Imaging Through Aberrating Media Simulation

NOTE:

Code for the experiment in this chapter (Chapter 8) has been published online. See “[Online Availability](#)” near the beginning of this thesis for more information.

8.1 Introduction

This chapter describes an experiment that involves imaging through an aberrating medium via backpropagation, without explicitly modeling the aberrating medium. The experiment is done using a modified version [1] of the Holotorch [2], which is a Fourier optics library.¹ This experiment is the “next step” after the MATLAB experiments (described in Chapter 7) as the modified version of Holotorch is expected to be more realistic than the MATLAB experiments. Ultimately, the results of the experiment provides more evidence that the concept of synthetic wavelengths can be usefully applied to DORT.

¹See “[Online Availability](#)” near the beginning of this thesis for more information on the modified version of Holotorch.

8.2 Outline of the chapter

This chapter details a DORT experiment done using a modified version [1] of the Holotorch [2].² The experiment is divided into two main steps: obtaining transfer matrices and backpropagating fields obtained from DORT.

Sections 8.3 and 8.4 provide details on the model used to obtain the transfer matrix used for DORT. Section 8.5 provides information on how the transfer matrix is obtained in simulation. Section 8.6 describes the DORT experiments that utilize the transfer matrix that was obtained—results are shown in that section (Section 8.6). Sections 8.7 and 8.8 describe limitations of the experiment. Finally, Section 8.9 gives some concluding remarks.

8.3 Holotorch model used when obtaining the transfer matrix

When performing DORT, one needs to measure a transfer matrix. This section details the simulated model used to obtain the transfer matrix. The process used to obtain the transfer matrix is detailed in Section 8.5.

8.3.1 Optical system overview

Figure 8.1 shows the simulated setup that is used to obtain the transfer matrix that is used in the experiment done in this chapter (Chapter 8). This setup is implemented using a modified version [1] of the Holotorch library [2].³ The setup consists of a Fourier transforming lens setup with the output plane of a spatial light modulator (SLM) in one focal plane of a lens and a collection of scatterers in the other focal plane of the aforementioned lens. There is a circular aperture on the front side—as in, the side facing the SLM—of the lens. Between the

²See “Online Availability” near the beginning of this thesis for more information on the modified version of Holotorch.

³See “Online Availability” near the beginning of this thesis for more information on the modified version of Holotorch.

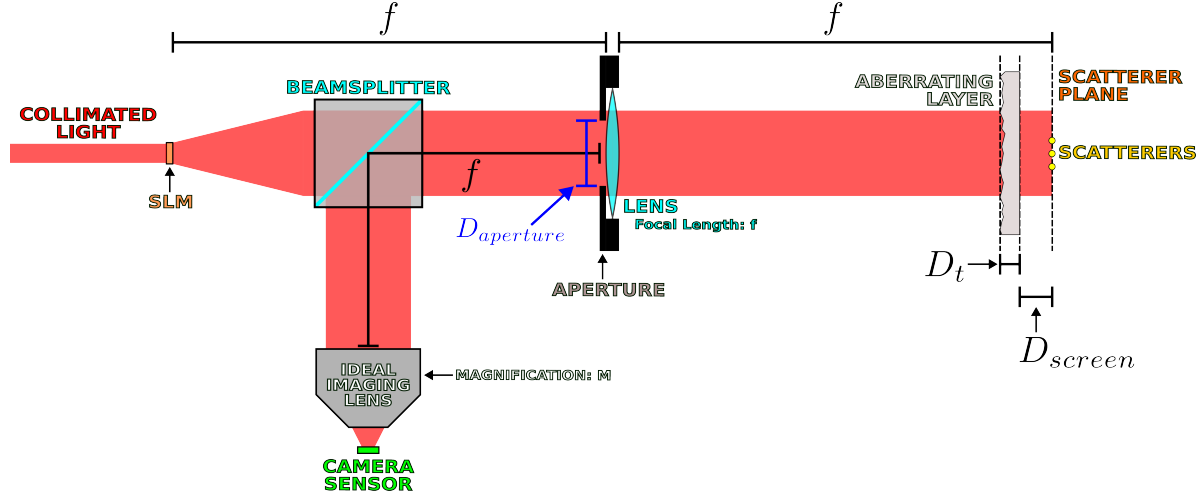


Figure 8.1: Simulated experimental setup used for measuring the transfer matrix used in Chapter 8

lens and the plane containing the scatterers is an aberrating layer that aberrates incoming wavefronts.

Light propagates from the SLM output plane, through the lens, through the aberrating layer, and then to the scatterers. Light incident on the scatterers bounces off and propagates in the opposite direction. The reflected light goes back through the aberrating layer and then back through the lens. A separate imaging lens setup images the reflected waves in the focal plane (not the focal plane that the scatterers lie in—the other focal plane) onto a camera sensor.

8.3.2 Optical system model details

In order to simulate this system, a model of the system was built using a modified version [1] of the Holotorch library [2],⁴ which is based around PyTorch. Referring to Figure 8.1, the model starts at the SLM output plane and ends at the input plane of the camera sensor. Figure 8.1 shows a parameterized diagram. In the experiment that was performed, the parameters in Figure 8.1 are $f = 50$ mm, $D_{aperture} = 10$ mm, $D_t = 200 \mu\text{m}$, $D_{screen} = 7$ mm,

⁴See “Online Availability” near the beginning of this thesis for more information on the modified version of Holotorch.

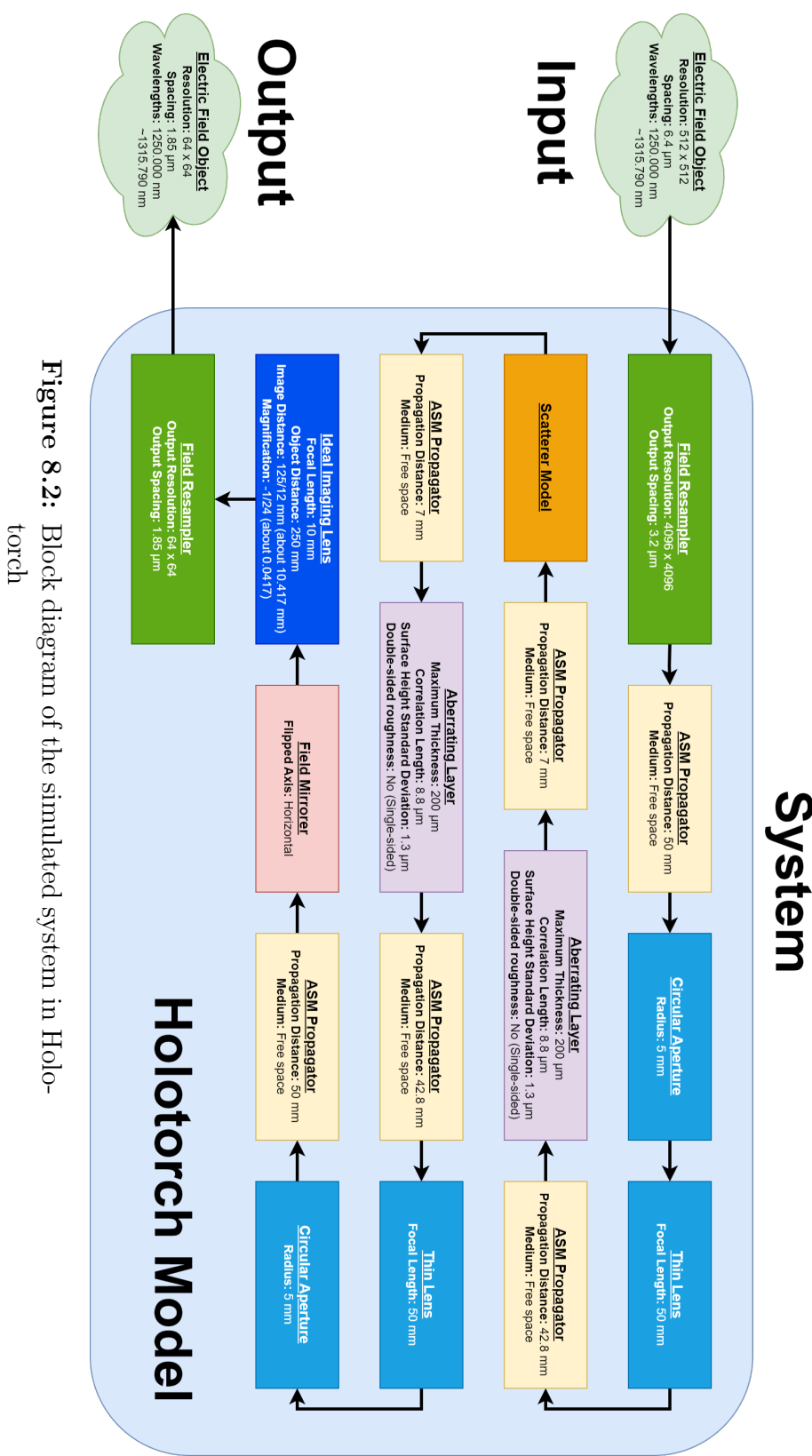


Figure 8.2: Block diagram of the simulated system in Holo-torch

and magnification $M = -1/24$.

Figure 8.2 shows a block diagram of the simulated system. The system model is built out of a sequence of components, which is shown in Figure 8.2. Each component takes an electric field object as its input and gives an electric field object as its output—in Holotorch, an electric field object consists of a multidimensional array of complex numbers which represent the values of the field at discrete points—where the points are uniformly sampled along a rectangular grid—along with data specifying the spacing of the electric field points and the wavelength of the electric field. To evaluate the model, an input electric field is first fed to that model. The first component in the model’s sequence of components takes that input electric field as input and gives an output. That output is then used as the input to the next component, and so on until the final component gives its output. The output of the final component is then used as the output of the model.

The model was run on an NVIDIA GeForce RTX 3080 Laptop graphics processing unit (GPU), which had 16 GB of video random-access memory (VRAM). Using a central processing unit (CPU) and random-access memory (RAM) to run the model was avoided as it would have likely been slower to run the model on those, compared to running the model on the aforementioned GPU. It should be also be noted that the limited VRAM of the GPU put a limit on how large and finely sampled the simulated fields could be.

The input to the model is taken to be the output of an amplitude and phase SLM. The SLM is 512×512 pixels in size, with the pixels being arranged in a rectangular grid with a pitch⁵ (i.e. spacing) of $6.4 \mu\text{m}$. The pixels are divided into 8×8 segments of pixels to yield 64×64 individually controllable segments. Note that all of the pixels in a given segment have the same output. Also note that the SLM itself is not simulated—instead, the output of the hypothetical SLM is generated programmatically.

The input to the model/input electric field is a 512×512 collection of points of a simulated electric field. Each of these points corresponds to the output of an SLM pixel in the

⁵A pitch of $6.4 \mu\text{m}$ was chosen to be consistent with the pitch on the HOLOEYE LETO. Moreover, as an aside, [25] used a HOLOEYE LETO SLM.

aforementioned SLM. Moreover, the input field contains fields at two wavelengths, one at 1250 nm and the other at approximately 1315.790 nm.⁶

The input electric field is fed to the first component in the model, which is a field resampler that resamples—using nearest-neighbor interpolation⁷—and pads the input electric field to lie on a 4096×4096 rectangular grid of points with a pitch of (i.e. spacing) of $3.2\text{ }\mu\text{m}$. Note that the physical size of the field does not change from input to output, but the input field representation is changed to fit the new space. The size of the resampled field— 4096×4096 points on a rectangular grid with a pitch of (i.e. spacing) of $3.2\text{ }\mu\text{m}$ —is the size that is used internally for the rest of the simulation.

The resulting resampled field is then propagated a distance of 50 mm through free space using an angular spectrum method (ASM) propagator component.⁸ Note that although there should be a beamsplitter somewhere along this 50 mm of propagation (see Figure 8.1), the beamsplitter is not modeled here. Thus, the partial reflection/partial transmission that would occur with a beamsplitter being present here is not modeled in this simulation.

Afterwards, a circular aperture component then applies a circular aperture with a radius of 5 mm (diameter 10 mm) to the field. The circular aperture component is implemented as a circular amplitude mask that only transmits a circular patch in the center. Note that unlike what is shown in the diagram in Figure 8.1, the circular aperture is modeled as being infinitely thin.

After the circular aperture component is a thin lens component. The thin lens component

⁶These wavelengths were chosen to be within the near-infrared window in biological tissue that occurs for wavelengths between 1000 nm and 1350 nm [27]. Less absorption occurs at these wavelengths in biological tissue.

⁷Nearest-neighbor interpolation is used in order to avoid distortions that occur when using bicubic interpolation. When turning on a single 8×8 SLM segment, which is done when measuring the transfer matrix in simulation (see Section 8.5 for more information on measuring the transfer matrix in simulation), bicubic interpolation gives overshoot in the resulting resampled SLM output pattern near the edges of the 8×8 SLM segment that is turned on. This may have something to do with the sharpness of the transition seen when single 8×8 SLM segments are turned on. Nearest-neighbor interpolation does not run into this issue, hence nearest-neighbor interpolation is used here instead of bicubic interpolation.

⁸The angular spectrum method (ASM) propagator requires one to take a two-dimensional discrete Fourier transform. In order to save memory, this operation was done “in-place” with specially written code (PyTorch’s `fft2` function was not an “in-place” operation). For more information, please refer to the publicized code for this thesis, which is linked to in “[Online Availability](#)” near the beginning of this thesis.

is implemented as a phase mask that introduces the phase shifts that would be introduced by a thin lens. This phase mask is applied to the field that was output in the previous step. Note that contrary to what is shown in Figure 8.1, the thin lens component is modeled as being infinitely thin. Now, under the convention that phasors rotate clockwise in time, the transmittance function of the phase mask should be [28]⁹

$$t_a(x, y) = \exp \left[-j \frac{k}{2f} (x^2 + y^2) \right], \quad (8.1)$$

where k is the wavenumber. Assuming that the lens is in free space, the thin lens phase mask requires a sampling interval less than or equal to $\lambda \frac{|f|}{D}$, where λ is the free space wavelength, f is the focal length, and D is the diameter of the lens [28].¹⁰ In this case, $D = 10\text{ mm}$, $f = 50\text{ mm}$, and the sampling interval is $3.2\text{ }\mu\text{m}$ —this means that the minimum wavelength that can be used here is 640 nm , which is smaller than any of the wavelengths used in the simulation (e.g. 1250 nm , approximately 1315.790 nm , and a synthetic wavelength of $25\text{ }\mu\text{m}$).

The field is then propagated a distance of 42.8 mm through free space using an ASM propagator component. Afterwards, the field is aberrated by an aberrating layer component. This aberrating layer component models a slab of varying thickness, with roughness on one side only and a refractive index of $n = 1.52$ (this refractive index is more-or-less consistent with that of glass). The slab is embedded in free space, which has a refractive index of $n = 1$. The aberrating layer model has various parameters, such as a maximum thickness of $200\text{ }\mu\text{m}$,¹¹ correlation length of $8.8\text{ }\mu\text{m}$, surface height standard deviation of $1.3\text{ }\mu\text{m}$,

⁹The equation for the lens transmittance function comes from Equation 6.12 in [28], where the pupil function $P(x, y)$ is taken to be a constant 1. The reason for this is that the circular aperture component fulfills the function of the pupil function.

¹⁰The expression $\Delta x \leq \lambda \frac{|f|}{D}$, where Δx is the sampling interval, comes from Equation 6.14 in [28].

¹¹ $200\text{ }\mu\text{m}$ was chosen because $200\text{ }\mu\text{m}$ was the mean thickness of the PDMS polymer layer in the aberrating layer in [16]. Admittedly, this PDMS polymer layer was deposited onto cover glass, which likely added to the thickness of the aberrating layer. $200\text{ }\mu\text{m}$ was also the mean thickness of the PDMS polymer layer in [16], **not** the maximum thickness as it is treated as in the model. Thus, choosing $200\text{ }\mu\text{m}$ as the maximum thickness in the model was not the most well thought out idea in hindsight.

However, it can be noted that the aberrating layer model is for a thin structure, so modeling thinner structures is preferable to modeling thicker structures. Therefore, it might have been good that $200\text{ }\mu\text{m}$ was chosen as the maximum thickness. Although, it is uncertain if $200\text{ }\mu\text{m}$ is sufficiently thin enough to result in an accurate model.

and single-sided roughness¹². The correlation length and surface height standard deviation statistics came from the 400SA diffuser statistics in [29].¹³ Note that the aberrating layer component assumes that the field is entirely transmitted and that no reflection occurs—this is not physically accurate. For more information on the aberrating layer component and its limitations, see Subsection 8.4.1.¹⁴ Now, after going through the aberrating layer component, the field is then propagated a distance of 7 mm through free space using an ASM propagator component.

Then, a scatterer model models scattering off of a set of three small, discrete scatterers. The scatterers are small and circular, and are located at coordinates¹⁵ $(-0.3 \text{ mm}, -0.4 \text{ mm})$, $(0.4 \text{ mm}, -0.3 \text{ mm})$, and $(0 \text{ mm}, 0.35 \text{ mm})$ with respective diameters of 0.012 mm, 0.015 mm, and 0.015 mm as well as respective scattering responses¹⁶ of 0.86, 0.82, and 0.78. The scatterer model outputs the scattered field that was scattered off of the scatterers. For more information on the scatterer model, see Subsection 8.4.3.

Afterwards, the scattered field travels back the way they came. To start, the field is propagated a distance of 7 mm through free space using the same 7 mm ASM propagator component as before. The field is fed through a model that is effectively identical to the aberrating layer model from before—the reason why the models are effectively identical is because propagation in the forward and reverse direction for the aberrating layer model should be the same based on how propagation is modeled in those models¹⁷. Then, the field is propagated a distance of 42.8 mm through free space using the same 42.8 mm ASM

¹²Single-sided roughness was assumed because many diffusers have single-sided roughness.

¹³Note that skewness was not modeled in the surface height distribution in the model, even though that statistic was given in [29].

¹⁴In that section, the refractive indices $n_{ambient}$ and n_{slab} are defined. The aberrating layer model in the simulation uses $n_{ambient} = 1$, which is the refractive index of free space, and $n_{slab} = 1.52$, which is a typical refractive index for glass.

¹⁵The coordinates are listed with the horizontal coordinate first and the vertical coordinate second.

¹⁶See Subsection 8.4.3 for the definition of “scattering responses”.

¹⁷The aberrating layer model applies phase shifts at points proportional to the thickness of the aberrating layer at those points. Since thickness is the same going forward and backward, the phase shifts should be the same in either direction. See Subsection 8.4.1 for more information on the aberrating layer model.

propagator component as before.¹⁸

The field is then fed through the same thin lens component that was used earlier and is afterwards fed through through the same circular aperture component as before—propagation through these components should be the same in both directions¹⁹, hence they are used again. Then, using the same 50 mm ASM propagator component as before²⁰, the field is propagated a distance of 50 mm through free space.

Looking at Figure 8.1, there should be a beamsplitter in the path of the 50 mm propagations. Moreover, during the last 50 mm propagation, we consider the reflected portion of the field (as opposed to earlier where the transmitted portion of the field was considered). Since the reflected portion is being considered, the field should be mirrored to model the mirroring that would occur on the reflected portion of the field due to the beamsplitter mirroring the field. Thus, after the last 50 mm propagation, the field is mirrored horizontally²¹ by feeding it through a horizontal field-mirroring component to model the mirroring that would occur as a result of reflection off of the beamsplitter. Note that the partial transmission/partial reflection of the field is not modeled here and that all of the field is assumed to have been reflected.

Next, an ideal imaging lens component images the resulting field. This ideal imaging lens component simulates a standard single lens imaging system. The input plane of the component is taken to be the object plane, and the output plane of the component is taken to be the image plane. Based on the object distance and the focal length, which are parameters that one provides to the component, the ideal imaging lens component calculates a magnification and applies that magnification to the input. The output field is thus equal to the input field with magnification applied.

¹⁸There is no need to define new ASM propagator components for identical propagation distances; hence, ASM propagator components are reused.

¹⁹The thin lens is modeled as having the same focal length on both sides. Therefore, it should behave the same going in either direction. The aperture is modeled as an amplitude mask, so it should behave the same going in either direction as well.

²⁰See Footnote 18.

²¹The field could have also been mirrored vertically, but the setup was imagined to lie in a horizontal, not vertical, plane. Thus, horizontal mirroring was done instead of vertical mirroring.

The ideal imaging lens has a focal length of 10 mm, an object distance of 250 mm, and an image distance²² of $125/12 \text{ mm} \approx 10.417 \text{ mm}$, which yields a magnification of $-1/24$. In the implementation, the magnification is done via resampling using bicubic interpolation. The purpose of this component is to scale the field down so it better fits onto the hypothetical image sensor.

Finally, a field resampler component resamples the field using bicubic interpolation. The new area covered by the resampled field is 64×64 with $1.85 \mu\text{m}$ spacing between sample points. This resolution is meant to be consistent with a 64×64 pixel subset of an imaging sensor, specifically a Sony IMX-226 CMOS sensor.²³

To summarize, the entire model takes as its input an electric field representation that has a size of 512×512 and where the points are spaced $6.4 \mu\text{m}$ apart. This electric field represents the output of an SLM consisting of 64×64 controllable segments of 8×8 blocks of pixels. The output of this model is an electric field representation that has a size of 64×64 and where the points are spaced $1.85 \mu\text{m}$ apart. This electric field represents the field incident on a small camera sensor. At a high level, this model describes propagation from the SLM output shown in Figure 8.1, through the optical system shown in that figure, and to the input plane of a small camera sensor, which is also shown in the aforementioned figure. Finally, this model was implemented using a modified version [1] of the Holotorch library [2], a Fourier optics library based around PyTorch.²⁴

²²The image distance is automatically calculated from the object distance and focal length.

²³The $1.85 \mu\text{m}$ spacing was chosen to be consistent with the spacing on a Sony IMX-226 CMOS sensor. Moreover, as an aside, [25] used a Sony IMX-226 CMOS sensor.

²⁴See “[Online Availability](#)” near the beginning of this thesis for more information on the modified version of Holotorch.

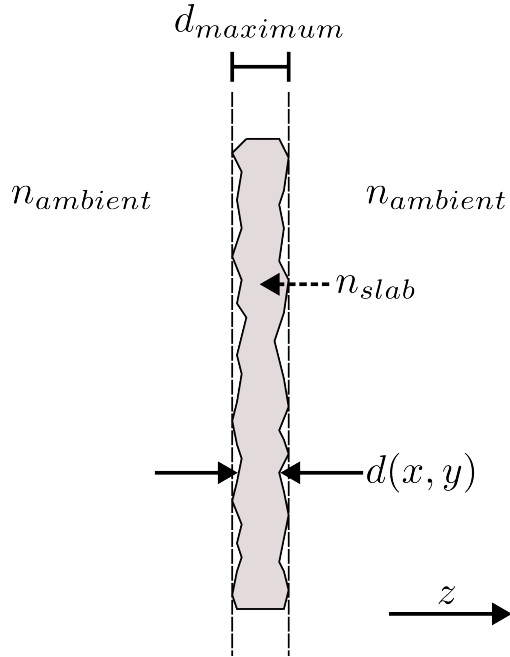


Figure 8.3: Random thickness screen model from Section 7.1.1 of [5]

8.4 More information on various model components

8.4.1 Aberrating layer model

In order to model an aberrating layer, the random thickness screen model specified in Section 7.1.1 in [5] was implemented. In that model, a thin slab with a refractive index of n_{slab} embedded in a medium with a refractive index of $n_{ambient}$ is assumed.²⁵ The slab has a thickness $d(x, y)$ that varies in the transverse direction, and a maximum thickness $d_{maximum}$.²⁶ Figure 8.3 gives an illustration for the model.

The model is implemented as a phase mask that applies a phase shift of

$$\Delta\phi(x, y) = \frac{2\pi}{\lambda}n_{slab}d(x, y) + \frac{2\pi}{\lambda}n_{ambient}\left[d_{maximum} - d(x, y)\right] \quad (8.2)$$

²⁵Section 7.1.1 in [5] uses n_1 and n_2 in place of $n_{ambient}$ and n_{slab} respectively.

²⁶Section 7.1.1 in [5] uses d_0 instead of $d_{maximum}$.

at each transverse coordinate (x, y) , where λ is the free space wavelength²⁷ (see Footnote 27 for a discussion on the validity of Equation 8.2). Essentially, the phase shift is proportional to the optical path length going through the structure in a direction that is perpendicular to the transverse plane. The phase shifts model propagation through the slab, and it is assumed that rays/wavefronts travel perfectly perpendicular to the transverse plane. Note that reflection at the interface is *not* modeled here.

Variations in thickness are determined by surface roughness statistics. In the simulation, two parameters are used to describe the surface roughness/height variations: surface height standard deviation σ_{height} and correlation length $l_{correlation}$. Surface height standard deviation σ_{height} is the standard deviation of the surface height variations [29] [30]. Correlation length $l_{correlation}$ describes how much lag in the height autocorrelation function is needed for it to reach $1/e$ times its maximum (zero lag) value [30]. Skew can also be used to describe the surface height variation [29] [30], but skew in the probability density of the surface height variations was not implemented in the simulation.

In order to generate random height variations for the model, random Gaussian distributed heights are generated via PyTorch’s `torch.randn(...)` function. The heights (in the space domain) are then convolved with a circular Gaussian function in order to obtain the desired correlation length $l_{correlation}$. Then, the result is scaled so that the standard deviation of the heights is the desired surface height standard deviation σ_{height} . If roughness on both sides of the slab is being modeled, then random height variations with the same $l_{correlation}$ and σ_{height} parameters are generated a second time for the second side—in this case, the generated height variations for both sides are added together to get the total height variations (note that in the experiment presented in this thesis, single sided—not double-sided—roughness is used). The thickness $d(x, y)$ is then determined based on the calculated height variations,

²⁷Equation 8.2 follows from Equation 7.1-1 in [5] as $c = \lambda f$ and time delay times angular frequency $\omega = 2\pi f$ gives phase shift. Equation 8.2-2 in Section 8.2 of [5] also gives a similar, albeit slightly different, expression to Equation 8.2—the fundamental idea is the same as Equation 8.2, however. Therefore, it is likely that Equation 8.2 is valid.

and it is ensured that the maximum thickness is $d_{maximum}$.²⁸

8.4.2 Discussion on the aberrating layer model

General discussion

The model described in Subsection 8.4.1 is supposed to model transmission/scattering through a thin slab of non-uniform thickness. It is a relatively simple model with a nice physical interpretation, namely that of rays/wavefronts traveling directly through the slab in a direction perpendicular to the transverse plane. Since the model is implemented as a wavelength-dependent phase mask, it is relatively simple²⁹ from a computational perspective. Moreover, the fact that the phase shift applied by the model is dependent on wavelength could be useful when experimenting with synthetic wavelengths as existing techniques involving synthetic wavelengths take advantage of wavelength-dependent phase shifts [7] [25].

It should be noted though that this model has some flaws. First off, it assumes rays/wavefronts enter and leave the slab at the same transverse location—this is implicitly assumed in Equation 8.2. However, incident rays/wavefronts do not necessarily travel perpendicularly to the transverse plane and refraction at the interfaces between media can change the direction of rays/wavefronts. The model described in Subsection 8.4.1 does not take these effects into account.

Moreover, as the aforementioned model is implemented as a phase mask, reflection at interfaces is not modeled. In general, when there is a change in refractive index, reflection of waves will generally occur, but this effect is not modeled in the model. The model also does not take into account attenuation that may occur as light travels through the slab.

²⁸There are some additional nuances to how thicknesses are calculated. Please refer to the publicized code for this thesis, which is linked to in “[Online Availability](#)” near the beginning of this thesis, for more information.

²⁹Compared to the conventional random phase screen model described in [31], which can involve computing free space propagation one or more times.

Possible alternative models

The conventional random phase screen model described towards the beginning of [31] could potentially be used instead of the random thickness model described in Subsection 8.4.1. That model is composed of a series of a sequence of random phase screens and propagations of a distance equal to the mean free path; the random phase screens and propagations alternate, and the sequence begins and ends with a random phase screen.³⁰ However, that model does not take into account reflection and does not take into account ballistic light.

Alternatively, [31] presents a model that has similarities to the conventional random phase screen model yet takes into account ballistic light. Such a model could potentially be used instead of a conventional random phase screen model.

However, one drawback of the two alternative models mentioned here is that they would likely be more computationally expensive than the random thickness model described in Subsection 8.4.1. This is because those models involve both phase screens (phase masks) and propagation, whereas the random thickness model only involves a phase mask.

8.4.3 Scatterer model

The scatterer model is implemented as an amplitude mask. The amplitude mask is transparent, save for the locations of the scatterers. Scatterers are represented as opaque spots on the amplitude mask that reflect with a certain amplitude.

One can control the location, diameter, and scattering response for each scatterer. The location and diameter of each scatterer determines which points on the mask get made opaque (i.e. given an amplitude other than zero). The amplitude of the points on the mask that are made opaque is set equal to the specified scattering response for that scatterer. For example, if there was a scatterer at point (0.1 mm, 0.2 mm) with a diameter of 0.01 mm and a scattering response of 0.8, points on the amplitude mask within 0.005 mm of the point

³⁰In that model, one could theoretically have just a single random phase screen and no propagators if the number of screens is set to 1.

(0.1 mm, 0.2 mm) would be set to 0.8.

In order to obtain the scattered fields from the incident fields, the incident field is multiplied by the amplitude mask. The result of this multiplication is the scattered field.

8.4.4 Discussion on the scatterer model

The scatterer model implicitly invokes a sort of first-order Born approximation as the scattered fields are produced by sources that are proportional in magnitude to the incident fields at the locations of the corresponding sources. However, the first-order Born approximation is an approximation. Furthermore, the scatterer model only considers scalar waves—this is an approximation as real light waves are vector waves. One could potentially model scatterers more accurately by taking into account Mie scattering theory and by taking into account the vector nature of light waves.

8.5 Measuring the transfer matrix in simulation

As stated earlier in Subsection 8.3.2, the input to the model is taken to be the output of an SLM with 64×64 controllable segments of 8×8 pixels. The output of the model is the incident field on a set of 64×64 camera sensor pixels. Now, recall from Section 2.3 that a transfer matrix relates a set of inputs $\vec{\mathbf{X}}(\lambda)$ to a set of outputs $\vec{\mathbf{Y}}(\lambda)$ by a matrix $\mathbf{H}(\lambda)$ via the formula $\vec{\mathbf{Y}}(\lambda) = \mathbf{H}(\lambda)\vec{\mathbf{X}}(\lambda)$. Each controllable SLM segment corresponds to a single element of the input vector $\vec{\mathbf{X}}(\lambda)$. On the camera sensor, each pixel's incident field corresponds to a single element of the output vector $\vec{\mathbf{Y}}(\lambda)$.

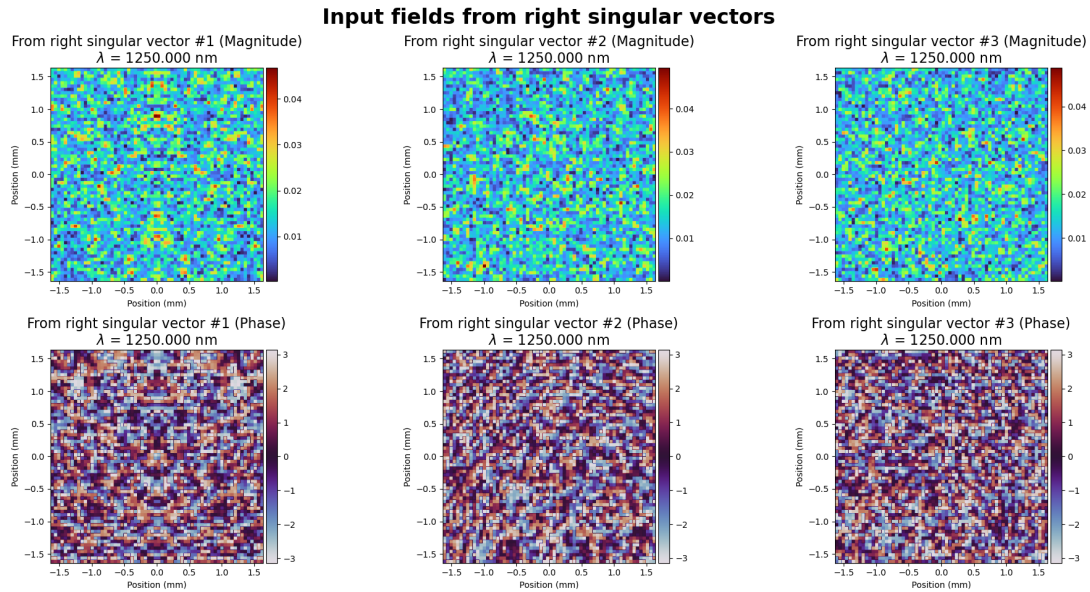
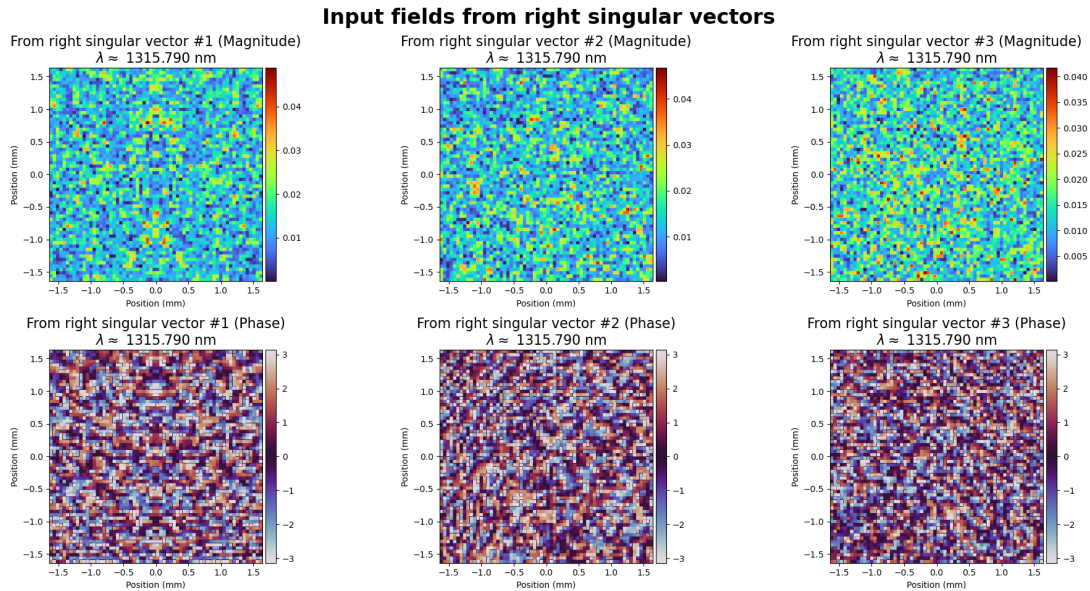
In simulation, the transfer matrix can be measured column-by-column by setting the i^{th} 8×8 pixel SLM segment output to 1 and the rest of the segment outputs to 0. This input can be input into the model described in Section 8.3 and the output of the model can be taken to be the i^{th} column of $\mathbf{H}(\lambda)$. This is akin to letting $\vec{\mathbf{X}}(\lambda) = \hat{\mathbf{e}}_i$, where $\hat{\mathbf{e}}_i$ is the i^{th} standard basis vector. Since $\vec{\mathbf{Y}}(\lambda) = \mathbf{H}(\lambda)\vec{\mathbf{X}}(\lambda)$, setting $\vec{\mathbf{X}}(\lambda)$ to $\hat{\mathbf{e}}_i$ gives $\vec{\mathbf{Y}}(\lambda)$ that is equal

to the i^{th} column of $\mathbf{H}(\lambda)$, so the i^{th} column of $\mathbf{H}(\lambda)$ can be recorded as the resulting $\vec{\mathbf{Y}}(\lambda)$. This process can be repeated for all i to get all of the columns of $\mathbf{H}(\lambda)$, and hence the entire matrix $\mathbf{H}(\lambda)$.

In the experiment detailed in this chapter (Chapter 8), the transfer matrix is computed for two wavelengths: $\lambda = 1250 \text{ nm}$ and $\lambda \approx 1315.790 \text{ nm}$. Due to the nature of PyTorch and the way that Holotorch³¹ is, the transfer matrix computation is able to be parallelized over wavelengths, meaning that the transfer matrix columns for the transfer matrices for both wavelengths could be computed at the same time. Additionally, the computation of transfer matrix columns can also be parallelized. The actual implementation of this chapter's (Chapter 8) experiment calculates three transfer matrix columns per each wavelength, for a total of six transfer matrix columns, in parallel.

Note that in a physical experiment, the procedure for measuring transfer matrices is different. See Subsection 2.3.2 for more information on how transfer matrices are measured in physical experiments.

³¹And consequently the modified version of Holotorch that was used.

(a) SLM output patterns from right-singular vectors ($\lambda = 1250 \text{ nm}$)(b) SLM output patterns from right-singular vectors ($\lambda \approx 1315.790 \text{ nm}$)**Figure 8.4:** SLM output patterns from right-singular vectors

8.6 Holotorch DORT experiments

Transfer matrices for the wavelengths $\lambda = 1250\text{ nm}$ and $\lambda \approx 1315.790\text{ nm}$ are obtained for the model described in Sections 8.3 and 8.4. These transfer matrices are obtained by using the procedure described in Section 8.5. DORT is performed using these transfer matrices.

In this experiment, the right-singular vectors from DORT give a set of signals that can be transmitted from the SLM. The i^{th} element of a given right-singular vector defines the complex output of the i^{th} controllable SLM segment. SLM patterns resulting from right-singular vectors are shown in Figure 8.4. These SLM patterns, when transmitted from the SLM, result in selective focusing on the scatterers. However, this selective focusing behavior relies on the properties of the system and aberrating medium. If one is simulating the system and an exact model of the aberrating medium is not used, then the selective focusing behavior is degraded.

This section (Section 8.6) investigates what happens when one tries to simulate selective focusing through an aberrating medium without modeling the aberrating medium. Specifically, in this experiment, two cases of the aforementioned focusing are considered: one not utilizing synthetic wavelengths and the other utilizing synthetic wavelengths. Note that the transfer matrices used for both of these cases are the same.

8.6.1 Non-synthetic wavelength case

The fields in Figure 8.7 were obtained by backpropagation of the SLM output fields derived from right-singular vectors, shown in Figure 8.4. Referring to Figure 8.1, the SLM output fields are propagated from the SLM output to the scatterer plane, except the aberrating layer is ignored. The simulation is done as if there was free space in place of the aberrating layer. Figure 8.5 shows an illustration of this process of propagating from the SLM output to the scatterer plane. The parameters in Figure 8.5 are $f = 50\text{ mm}$ and $D_{\text{aperture}} = 10\text{ mm}$, just as they were in Figure 8.1 in Section 8.3.

A block diagram of the model used for backpropagating fields to the scatterer plane is given in Figure 8.6. This model is similar, and in some ways identical to, the model described in Section 8.3 going from the SLM output to the scatterer plane—this model does not include the scatterer plane itself and the components that come after it, however. Additionally, it can be seen that the ASM propagator that propagates a distance of 42.8 mm, the $200\text{ }\mu\text{m}$ thick aberrating layer model, and the ASM propagator that propagates a distance of 7 mm have been condensed into a single ASM propagator that propagates a distance of 50 mm, thus effectively removing the aberrating layer from the system by replacing it with free space.

In Figure 8.7, does not see selective focusing behavior. The fields do seem to slightly tend towards individual scatterers, however. The focusing is quite blurry, not centered on the scatterers, and the spots where the field is visible appear to have speckle-like noise.³² Figure 8.8 shows where the fields in Figure 8.7 reach their maximums.³³ Had the aberrating layer been modeled, the fields would reach their maximums at the location of the scatterer. However, the aberrating layer is not being modeled here, or more specifically, it has been replaced with free space here. Looking at Figure 8.8, the maximums of the fields are offset quite a lot from the scatterer locations. Thus, it seems like using maximums in the fields may not be a reliable means of ascertaining scatterer locations in this case.

To summarize, from Figures 8.7 and 8.8, it is evident that not modeling the aberrating layer has greatly degraded the selective focusing. Ideally, one would be able to model the aberrating layer. However, in practice, it is not always possible to get an exact model for an aberrating or scattering medium. This causes difficulties when trying to image and locate scatterers by backpropagating fields. Ultimately, it does not appear to be feasible to locate

³²As an aside, it appears that periodic copies are visible in Figure 8.7. This is presumably due to the fact that a Fourier transforming lens was used and the SLM field can be thought of as the result of sampling, convolution with a rect function, and windowing. The spacing between the presumably periodic copies is also consistent with theory as the spacing between the presumably periodic copies is around $\frac{1}{8.64\text{ }\mu\text{m}} \cdot \lambda f$, which would be the spacing that one would get from a Fourier transforming lens ($8 \cdot 6.4\text{ }\mu\text{m}$ is the pitch for the 8×8 controllable SLM segments, and the focal length f is 50 mm, so $f = 50\text{ mm}$). Thus, it can be concluded that the “copies” seen in Figure 8.7 are due to how the SLM output field is constructed and the fact that a Fourier transforming lens setup is used.

³³This was accomplished by scaling the lower limit on the color axis to cut off all but the most intense points in the field.

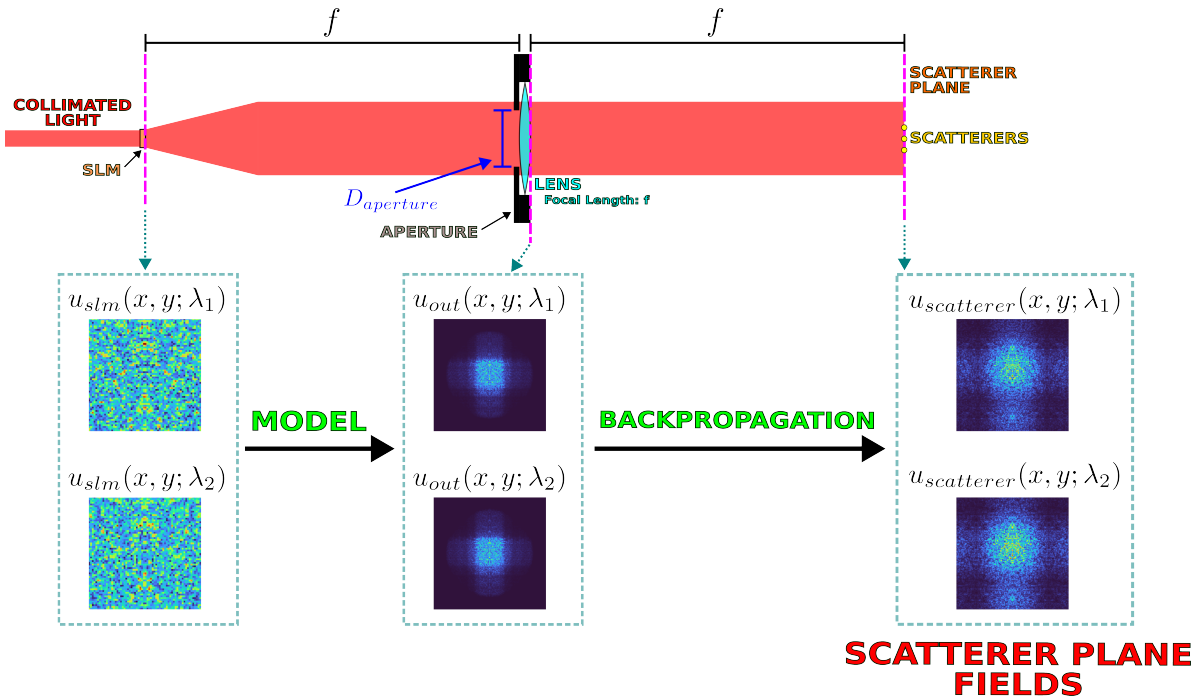


Figure 8.5: Diagram illustrating backpropagation to the scatterer plane

scatterers using the backpropagated scatterer plane fields shown in Figure 8.7 and 8.8.

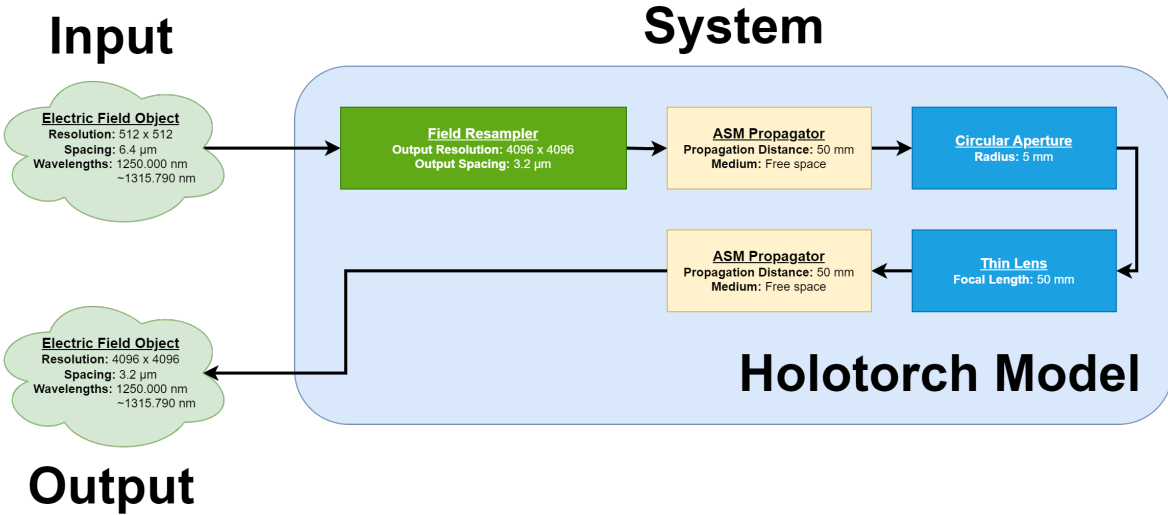


Figure 8.6: Block diagram of non-synthetic wavelength backpropagation

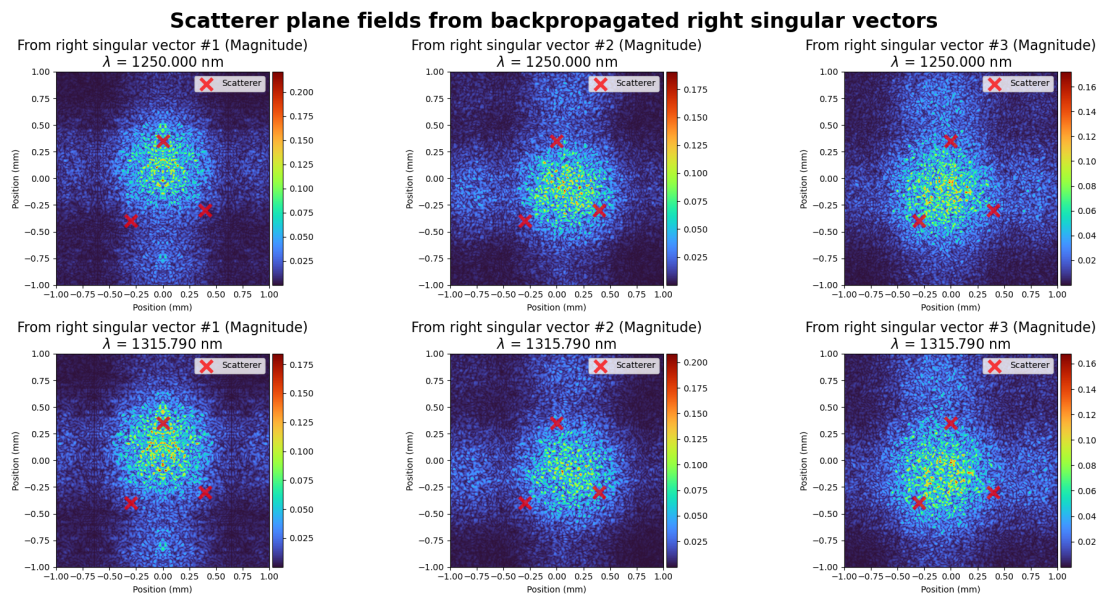


Figure 8.7: Scatterer plane fields from backpropagated right-singular vectors (non-synthetic wavelength case)

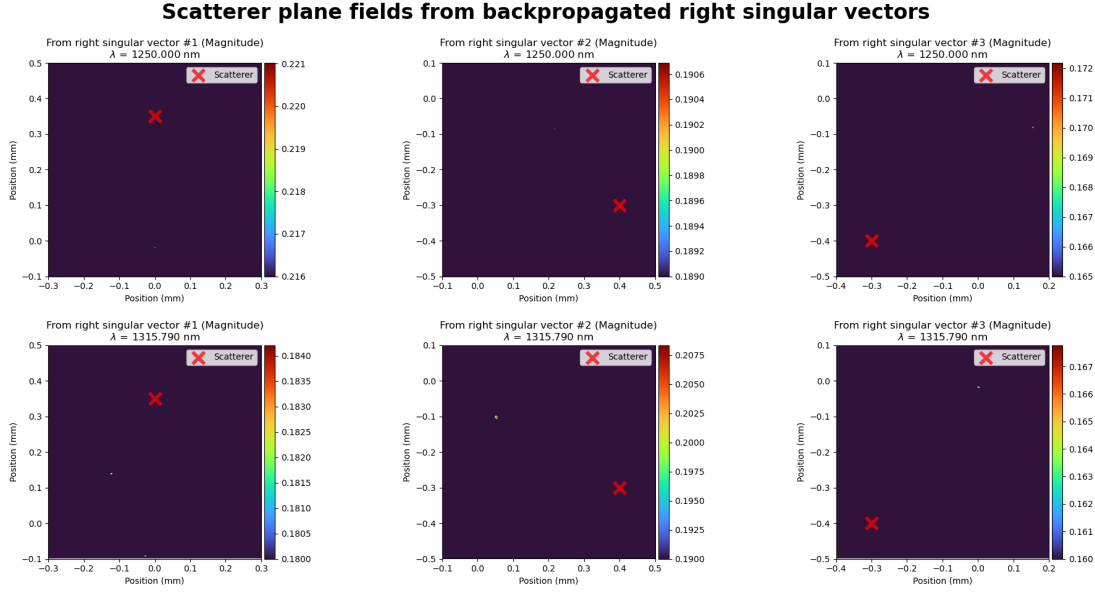


Figure 8.8: Field maximums in plots in Figure 8.7

8.6.2 Synthetic wavelengths case

Synthetic wavelengths can be utilized to alleviate some of the difficulties experienced with trying to image via backpropagation without a model for the aberrating layer. In order to do this, SLM output fields from the right-singular vectors were fed into a model that is nearly identical to the one for the non-synthetic wavelengths case described in Subsection 8.6.1, save for an extra synthetic field synthesis step after the thin lens output. A block diagram of the model used in this case, the synthetic wavelengths case, is shown in Figure 8.9.

Figure 8.10 provides an illustration of what is happening. Note that the parameters in this figure are the same as those for Figure 8.1 in Section 8.3, i.e. that $f = 50 \text{ mm}$, $D_{\text{aperture}} = 10 \text{ mm}$.³⁴ It can be seen from that figure that the SLM output fields for two wavelengths—in this case 1250 nm and approximately 1315.790 nm—are propagated through the system up until the output of the thin lens model. These fields are denoted as $u_{\text{out}}(x, y; \lambda_1)$ and $u_{\text{out}}(x, y; \lambda_2)$ respectively. Then, via computation, the fields $u_{\text{out}}(x, y; \lambda_1)$ and $u_{\text{out}}(x, y; \lambda_2)$

³⁴Note that not all of the parameters shown in Figure 8.1 are present in Figure 8.10.

are then combined into synthetic fields according to the equation

$$u_{synth}(x, y; \Lambda) = u_{out}(x, y; \lambda_1) \odot u_{out}^*(x, y; \lambda_2), \quad (8.3)$$

where \odot denotes pointwise multiplication, $\lambda_1 = 1250\text{ nm}$, $\lambda_2 \approx 1315.790\text{ nm}$, and the synthetic wavelength Λ is equal to $\frac{\lambda_1 \lambda_2}{|\lambda_1 - \lambda_2|} = 0.025\text{ mm}$. Note that in general, one should have $\lambda_1 < \lambda_2$. The synthetic fields for various right-singular vectors are shown in Figure 8.11. Although noisy, it appears that the phase plots in that figure may be showing spherical wavefronts, which would be consistent with what is seen later in Figure 8.12.³⁵

This synthetic fields $u_{synth}(x, y; \Lambda)$ are then backpropagated to the scatterer plane using a 50 mm ASM propagator component—just as with the non-synthetic wavelengths case in Subsection 8.6.1, the aberrating layer component that was present in the model used to obtain the transfer matrix has been replaced with free space in this case, the synthetic wavelengths case. Note that this backpropagation occurs at the synthetic wavelength, i.e. the wavelength of the light is taken to be the synthetic wavelength in the computations. In this case, the synthetic wavelength is $\Lambda = 0.025\text{ mm}$. The results of this backpropagation are shown in Figure 8.12. It can be seen that the fields focus on and are centered on individual scatterers, unlike what was seen in Figure 8.7 in Section 8.6.1 where the fields are not focused and not centered on individual scatterers. Now, note that the spots where the field is focused in Figure 8.12 are somewhat large compared to the scatterers. This is likely due to a mixture of the length of the synthetic wavelength and the limited numerical aperture from the synthetic fields shown in Figure 8.11.³⁶

Figure 8.13 shows where the fields in Figure 8.12 reach their maximums.³⁷ Compared to

³⁵Consistent insofar as the backpropagated synthetic fields end up converging to a vaguely pointlike area (the term “pointlike” is being used very loosely here) in Figure 8.12, which could be consistent with a spherical-like wavefront converging.

³⁶The synthetic fields that were backpropagated 50 mm by the ASM propagator component appear to be roughly $2\text{ mm} \times 2\text{ mm}$ in extent. Since the propagation distance was 50 mm, the numerical aperture is limited, which should limit how sharply one can focus. Using a smaller synthetic wavelength or having a better numerical aperture should improve how sharply the fields focus on single spots.

³⁷As with Figure 8.8, this was done by scaling the lower limit on the color axis to cut off all points in the field except for those with the highest magnitudes.

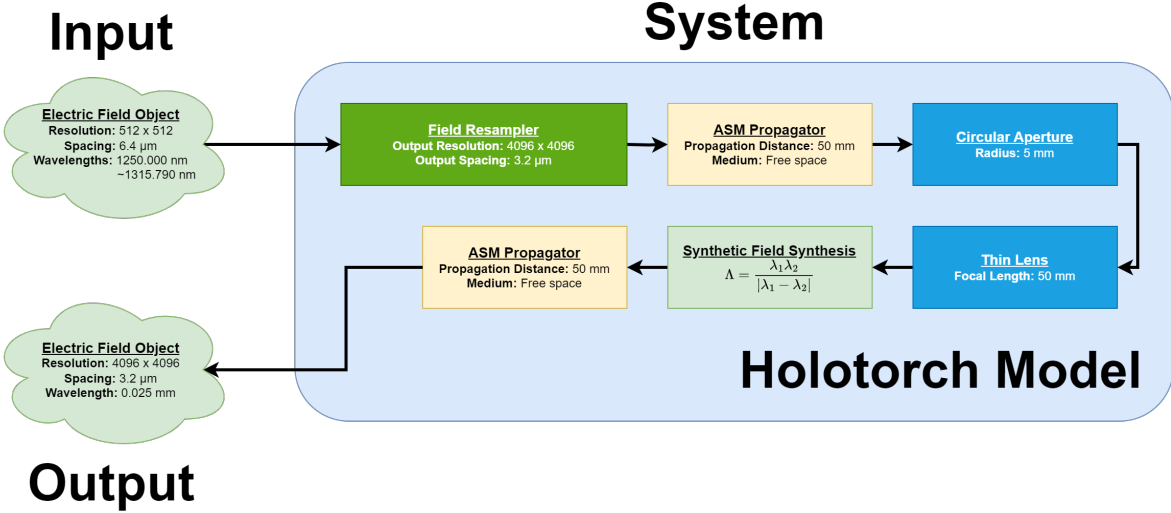


Figure 8.9: Block diagram of synthetic wavelength back-propagation

Figure 8.8, the fields maximums in Figure 8.13 are consistently close to the scatterer location. Thus, it appears that one can use the locations of field maximums in the backpropagated synthetic fields in the scatterer plane to locate scatterers.

In summary, from Figures 8.12 and 8.13, it can be seen that using synthetic wavelengths allows one to perform selective focusing on scatterers. This was done without modeling the aberrating layer, which one oftentimes does not have a precise model for. Thus, it appears as if using synthetic wavelengths allows one to locate scatterers and perform selective focusing even without having a model for an aberrating layer.

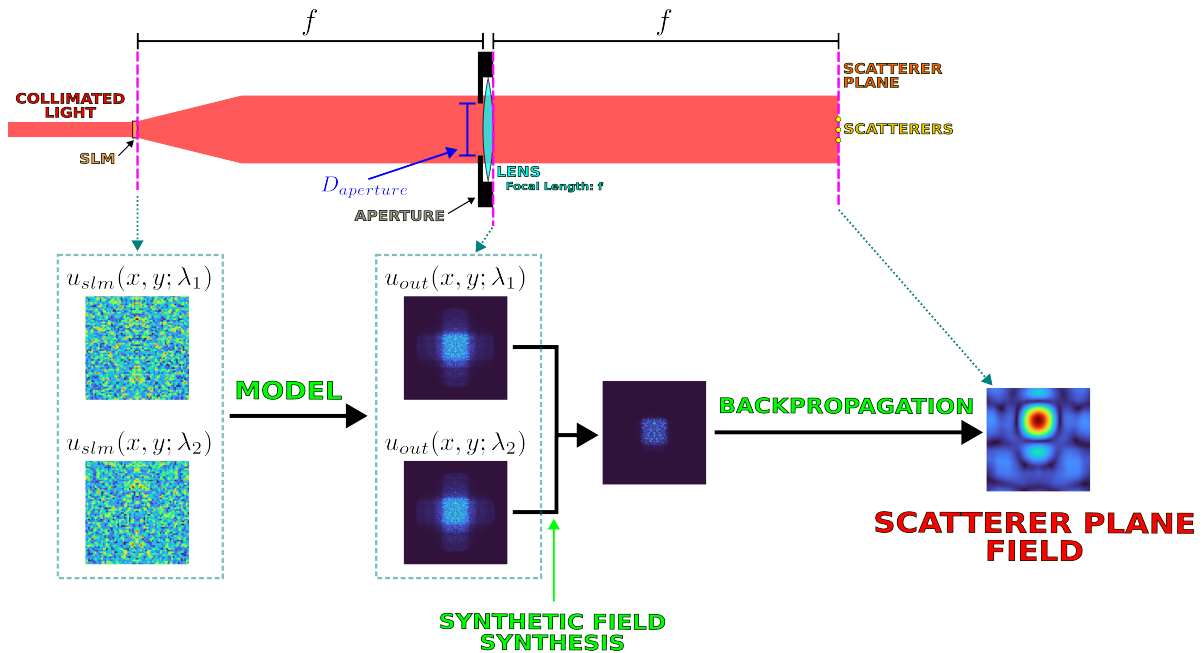


Figure 8.10: Diagram illustrating synthetic field generation and synthetic field backpropagation

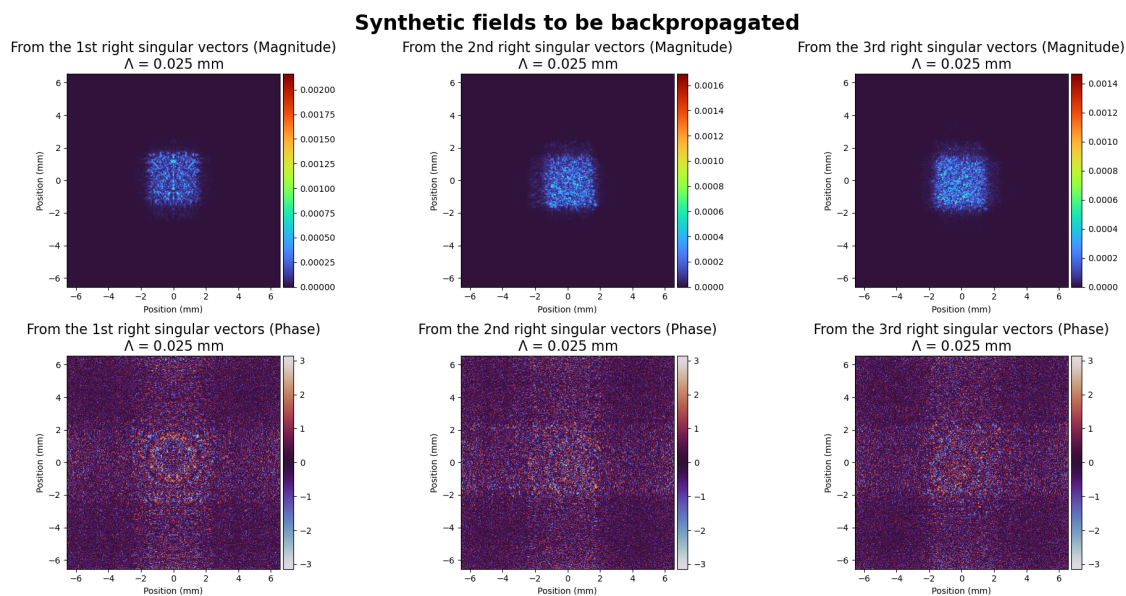


Figure 8.11: Synthetic fields before backpropagation

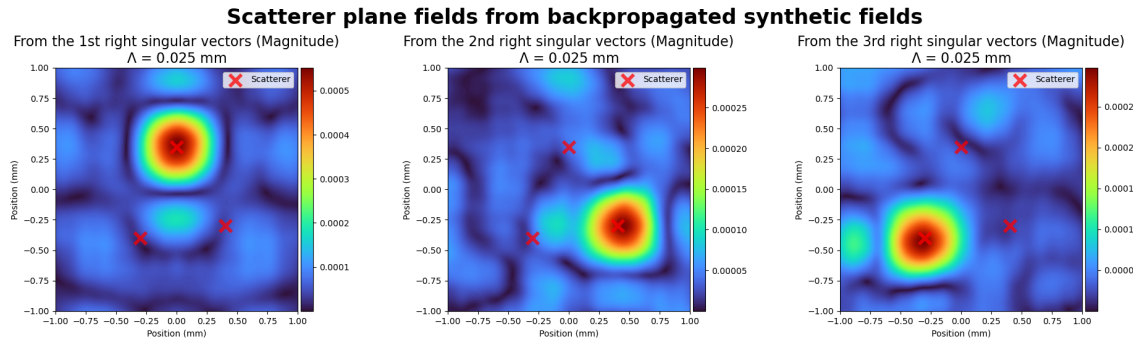


Figure 8.12: Scatterer plane fields from backpropagated right-singular vectors (synthetic wavelength case)

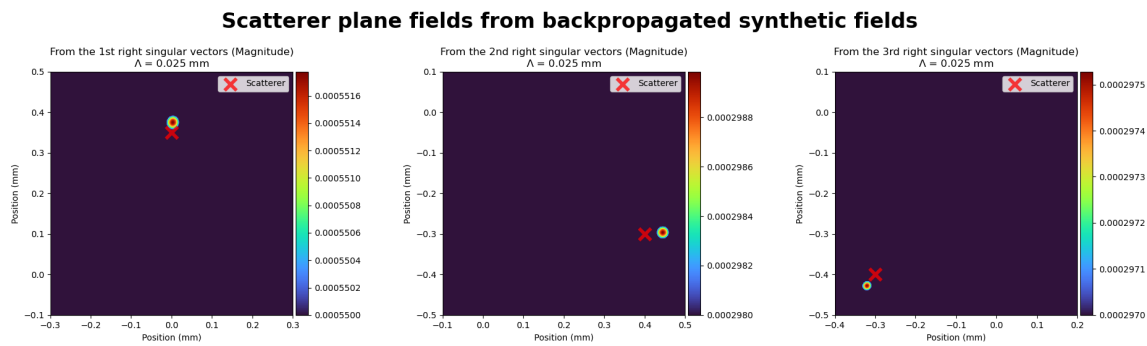


Figure 8.13: Field maximum in plots in Figure 8.12

8.6.3 Some additional comments

It should be noted that no eigenstructure demixing was done³⁸ for the synthetic wavelengths case detailed in Subsection 8.6.2 (see Section 3.5 for an explanation of eigenstructure mixing and demixing). Eigenstructure mixing does not seem to have occurred for the singular vectors shown in Figure 8.12. This can be verified by looking at the results of propagating the SLM output fields derived from the right-singular vectors from DORT, shown in Figure 8.4, from the SLM output plane to the scatterer plane input in Figure 8.1. Note that the aberrating layer is present and modeled³⁹ here, unlike earlier in Subsections 8.6.1 and 8.6.2. Doing this propagation, the results of which are shown⁴⁰ in Figure 8.14, it can be seen that for $1 \leq i \in \mathbb{Z} \leq 5$, the i^{th} non-synthetic singular vectors across wavelengths appear to correspond to the same scatterer and scattering pattern⁴¹ as the scatterer that is being focused on and the scattering pattern appear to be the same for the backpropagated i^{th} non-synthetic right-singular vectors across wavelengths. Thus, it does not appear that eigenstructure mixing has occurred for the first five non-synthetic singular vectors at either wavelength. Because no eigenstructure mixing seems to have occurred for those singular vectors, there was no need to perform eigenstructure demixing as only the results from the first three singular vectors are shown prior to this point in this thesis.

Additionally, as an aside, it can be noted that non-synthetic right-singular vectors beyond the 3rd non-synthetic right-singular vectors⁴² correspond to additional scattering patterns of the scatterers. When backpropagating non-synthetic right-singular vectors from DORT **with** the aberrating layer model present, i.e. backpropagating non-synthetic right-singular vectors

³⁸The code for this thesis does have a rudimentary and imperfect eigenstructure demixing function implemented, however. For more information on this eigenstructure demixing function, please refer to the publicized code for this thesis, which is linked to in “[Online Availability](#)” near the beginning of this thesis.

³⁹Since this experiment was done in simulation, there was an explicit computational model for the aberrating layer. In general, i.e. for real world experiments, one might not have an explicit computational model for the aberrating layer.

⁴⁰Note that the views are “zoomed in” in Figure 8.14.

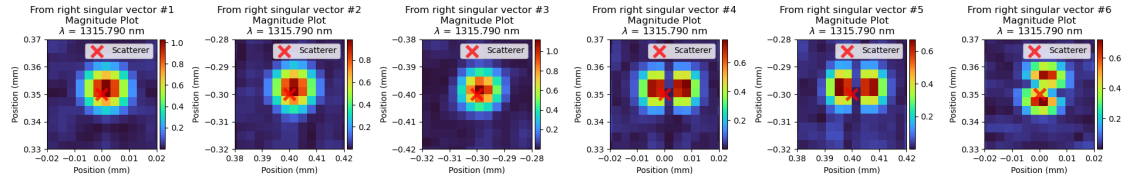
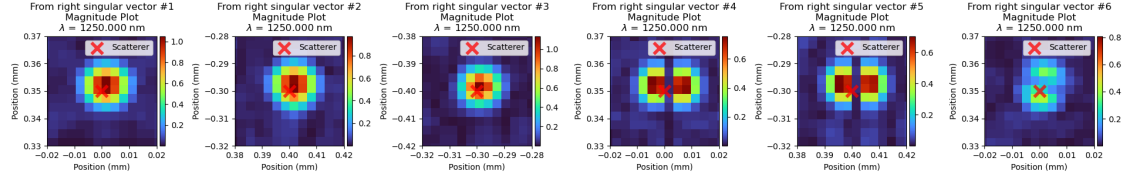
⁴¹The phase “scattering pattern” is used in [16]. See [16] to get a sense of what is meant by the phrase “scattering pattern”.

⁴²Results for only the first three singular vectors are shown in Figure 8.12.

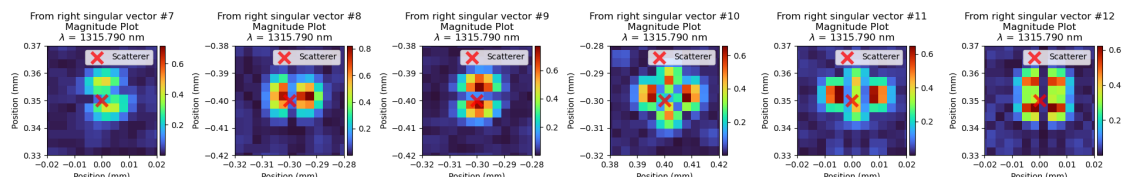
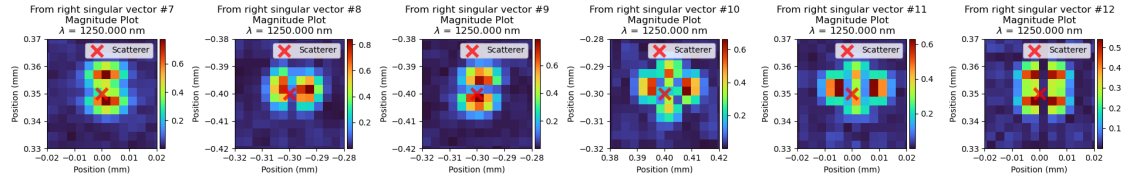
from the SLM output plane to the scatterer plane input shown in Figure 8.1, scattering patterns⁴³ similar to the ones seen in [16] show up—see Figure 8.14 for an illustration.

Finally, although the focusing is sharper in Figure 8.14 relative to the other cases in Subsections 8.6.1 and 8.6.2, it requires knowing the aberrating medium precisely. One needs a precise model of the aberrating medium to do the sort of focusing seen in Figure 8.14. Thus, the results shown in Figure 8.14 are likely not attainable in practice via numerical backpropagation as getting an explicit model of an aberrating medium in practice is likely difficult.

⁴³See [16] to get an idea of what is meant by the phrase “scattering patterns”.

Backpropagated fields (with aberrating layer model)

(a) Singular vectors #1-6

Backpropagated fields (with aberrating layer model)

(b) Singular vectors #7-12

Figure 8.14: Results of backpropagating non-synthetic singular vectors with the aberrating layer being modeled

8.7 Simulation limitations

The simulation is subject to a number of limitations. First off, the Holotorch library [2], and hence this simulation, deals with *scalar* wave propagation. However, for the wavelengths in this simulation (1250 nm and approximately 1315.790 nm, so near-infrared), light behaves as an electromagnetic wave. However, electromagnetic waves are vector waves, not scalar waves, and thus modeling light as a scalar waves is not entirely accurate. Despite that, as stated in Section 3.2 of [32], treating light as a scalar wave is oftentimes a valid approximation. For more information and relevant references on the applicability of treating light as a scalar wave, see the end of Section 3.1 in [32]⁴⁴ and all of Section 3.2 in [32]. It is also worth noting that the polarization of light is not being considered in this experiment, so the need for a vector treatment of waves is lessened.⁴⁵

Another limitation is the aberrating layer model. As stated before, the aberrating layer model models a screen of random thickness and assumes that incident rays/wavefronts enter and exit at the same transverse location. This is not entirely accurate as the hypothetical aberrating layer is not infinitely thin. Still, this model can be good for sufficiently thin structures, according to Section 7.1.1 of [5]. However, it is, to the author of this thesis, unknown whether the thickness of the modeled aberrating layer ($200\ \mu\text{m}$) is thin enough for the model to be a good approximation. For more information on the aberrating layer model, see Subsection 8.4.1.

It can also be noted that the aberrating layer model roughly approximates a diffuser. However, diffusers can have thicknesses on the order of millimeters—the aberrating layer model models a slab that has a rough surface and a maximum thickness of $200\ \mu\text{m}$. This could introduce further mismatch between the model and a real setup with a diffuser.

⁴⁴At the end of Section 3.1 in [32], “Ref. [29]” was said to give a “more complete discussion of the applicability of scalar theory in instrumental optics”. An interested reader may want to refer to that source.

⁴⁵If one needs to consider the vector nature of light, there may be a way to do so in Holotorch. As it is now, Holotorch [2] represents light/electric fields as six-dimensional tensors. One could choose a dimension that is otherwise of size 1 and expand it to size 3, where each slice along that expanded dimension corresponds to an X, Y, or Z polarization component of the electric field. Code could then be written to take the components of the electric field into account.

There are also limitations with the way that the scatterers in the scatterer plane are modeled. Scatterers are modeled as opaque spots on an amplitude mask. This is a simplified way of modeling scatterers and may not capture the intricacies of scattering events. For more information on the scatterer model, see Subsection 8.4.3.

Furthermore, partial partial reflection and partial transmission from the beamsplitter is not modeled. This is not matched with reality as beamsplitters partially reflect and partially transmit incoming waves. However, only one path of the beamsplitter is being considered, and the attenuation that would result from the beamsplitter should probably not affect the simulation much. Therefore, the fact that the beamsplitter is not fully modeled should hopefully not have affected the results much.

Another limitation comes with the lens model. Reflection off of the lens is not modeled. Moreover, the thin lens approximation is used, so the thickness of the lens is neglected. The circular aperture that is against the lens is also modeled as being infinitely thin, which is not aligned with reality; apertures are not infinitely thin.

Moreover, the ASM propagator components assume that propagation takes place through free space. However, actual experiments usually take place in air. It can be noted, however, that air often has a refractive index very near that of free space, to the point that the refractive index could probably be assumed to be $n = 1$ without much error in many cases. While it is possible that trying to model the intricacies of air as a medium might yield little in the way of additional accuracy, a more rigorous experiment might take into account the index of refraction and absorbance of air at the wavelengths used in the experiment.

8.8 Other potential limitations

In the experiment in this chapter (Chapter 8), the synthetic wavelength used was $\Lambda = 0.025$ mm. This small of a synthetic wavelength was used to reduce the size of the spot that was focused on after backpropagating synthetic fields (see Figure 8.12). Using this small of

a synthetic wavelength worked in the simulated experiment in this chapter (Chapter 8), as demonstrated by the results described in Subsection 8.6.2. It can be noted that the surface height standard deviation of the simulated aberrating layer is $1.3\text{ }\mu\text{m}$, which means that the path length aberrations should have largely remained below the $\Lambda/4$ limit given in [7]—this could potentially explain why using a synthetic wavelength of $\Lambda = 0.025\text{ mm}$ worked in the simulated experiment in this chapter (Chapter 8).

However, in [7], longer synthetic wavelengths than $\Lambda = 0.025\text{ mm}$ were used—the smallest synthetic wavelength shown in Figures 2 and 3 in [7] is $\Lambda = 0.28\text{ mm}$, which is an order of magnitude larger than what was used in the experiment presented in this chapter (Chapter 8). In [7], it is noted that optical fields at the two wavelengths become less correlated as the synthetic wavelength becomes smaller. Moreover, [7] did real (not simulated) experiments and ran into issues with speckle noise with smaller synthetic wavelengths, as demonstrated in Figures 2 and 3 of [7].

Thus, it is possible that the use of a small synthetic wavelength (e.g. $\Lambda = 0.025\text{ mm}$) could be problematic if the experiment presented in this chapter (Chapter 8) were to be translated into a real life experiment. However, it should be noted that the method used in [7] for obtaining images is different from the method used in the experiment presented in this chapter (Chapter 8) for obtaining images. Additionally, the experiment presented in this chapter (Chapter 8) imaged small, discrete scatterers as opposed to larger objects, like what was done in [7]. Given the differences between the experiment presented in this chapter (Chapter 8) and [7], it may be possible that a different set of limitations applied in [7]. However, it is also possible that the same limitations do apply and that the experiment in this chapter (Chapter 8) was not sufficiently realistic. It ultimately remains an open question—at least to the author of this thesis at the time of this writing—as to whether or not one would encounter issues with using small synthetic wavelengths (e.g. $\Lambda = 0.025\text{ mm}$) if one were to translate the experiment presented in this chapter (Chapter 8) into a real experiment.

Another potential limitation is that in practice, one might not know which plane the scatterers lie in or the scatterers might not lie in a plane. In the experiment in this chapter (Chapter 8), all of the scatterers lied in the plane that was exactly one focal length behind the lens. The backpropagation in the experiment in this chapter (Chapter 8) was done with explicit knowledge of what plane the scatters lied in. With this knowledge, the fields were able to be backpropagated to the plane that the scatterers lied in. In cases where the plane(s) that the scatterers lie in is unknown, one might have to look at the backpropagated fields in multiple different planes in order to image and locate scatterers.

8.9 Summary and observations

In this chapter (Chapter 8), an experiment involving focusing through an aberrating medium via numerical backpropagation of fields from DORT was done. Specifically, the backpropagation was done without modeling the aberrating medium and instead modeling it as free space.

Backpropagation without synthetic wavelengths and without modeling the aberrating medium gave results that did not look like selective focusing (see Figure 8.7). The fields in the scatter plane were noisy, unfocused, and were not centered on individual scatterers. It is evident that not modeling the aberrating medium prevented the backpropagated fields from being focused on individual scatterers.

Using synthetic wavelengths allowed one to get focusing in the scatterer plane even without modeling the aberrating medium (see Figure 8.12). Focused spots appeared in the backpropagated scatterer plane field, and these spots were centered on individual scatterers. The size of these spots was large compared to the size of the scatterers presumably due to the limited numerical aperture implied by the backpropagated synthetic field⁴⁶ (see Figure 8.11) and the length of the synthetic wavelength.

⁴⁶See Footnote 36.

From this experiment, it appears that not modeling the aberrating medium causes conventional DORT, i.e. DORT without synthetic wavelengths, to fail to image small, discrete scatterers⁴⁷. However, from this experiment, it also appears that using DORT in conjunction with synthetic wavelengths allows one to ignore the presence of an aberrating medium and image small, discrete scatterers⁴⁸. Thus, it would seem that DORT combined with synthetic wavelengths succeeded where DORT alone failed.

Without a physical experiment, it may be premature to claim that the method described in this chapter (Chapter 8) involving combining DORT and synthetic wavelengths is efficacious. However, based on the results of the experiment detailed in this chapter (Chapter 8), it seems that combining DORT and synthetic wavelengths can potentially allow one to image small, discrete scatterers through an aberrating medium without needing a model for the aberrating medium. This is a useful ability as one does not always have an explicit model for aberrating media.

⁴⁷These scatterers take the form of small (on the order of 0.01 mm in diameter), opaque, circular spots in a plane.

⁴⁸See Footnote 47.

Chapter 9

Conclusion and Future Work

9.1 Conclusion

In this thesis, various simulated experiments combining the DORT technique with synthetic wavelengths were carried out. Although the simulated experiments done in Chapters 7 and 8 were different, both relied on the same fundamental idea: singular vectors from DORT defined signals/fields that could be used to derive synthetic signals/fields that, when backpropagated, would focus on individual scatterers. Henceforth, the technique of deriving synthetic signals/fields from singular vectors from DORT shall be referred to as “Synthetic Wavelength DORT”, or “SW-DORT” for short.

SW-DORT showed promise eliminating spatial aliasing in backpropagated fields. The use of a longer wavelength allowed the $< \lambda/2$ inter-element spacing requirement necessary for there to be no spatial aliasing to be satisfied. This resulted in less ambiguous images than those obtained via conventional DORT and backpropagation.

SW-DORT also showed promise in imaging small, discrete scatterers¹ through aberrating media without needing an explicit model of the aberrating medium. Even in the presence of aberrations, backpropagating synthetic fields from SW-DORT still gave images of individual

¹The scatterers in question are small (on the order of 0.01 mm in diameter), opaque, circular spots in a plane.

scatterers. Conventional DORT failed in these cases.

Ultimately, these simulated experiments provide indications of the potential efficacy of SW-DORT. It appears that in certain situations, augmenting the DORT technique with synthetic wavelengths improves results. Based on the results of the simulated experiments, SW-DORT may be able to mitigate spatial aliasing in backpropagated field images and image through aberrating media. Both of these capabilities could potentially be useful, and the latter capability is a capability that is often sought after. Even though the experiments detailed in this thesis were not physical experiments, the results obtained from those experiments are promising and could pave the way for physical experiments down the line.

9.2 Future work

This thesis leaves some room for future work. One such work could be to validate the DORT equations, which are presented in Chapter 4. The MATLAB experiment code in Chapter 7 could be modified to calculate the $\mathbf{B}(\lambda)$, $\mathbf{S}(\lambda)$, and $\mathbf{F}(\lambda)$ matrices² (note that the aforementioned code is available online; see Footnote 2 for more information). Then, after calculating those matrices (i.e. the $\mathbf{B}(\lambda)$, $\mathbf{S}(\lambda)$, and $\mathbf{F}(\lambda)$ matrices), one could check to see how accurate Equations B.24, B.26, B.35, and B.38 are. When doing this, one should keep in mind that the aforementioned DORT equations (i.e. Equations B.24, B.26, B.35, and B.38) assume a structure/ordering for the $\mathbf{B}(\lambda)$, $\mathbf{S}(\lambda)$, and $\mathbf{F}(\lambda)$ matrices. This structure/ordering is specified in Appendix Subsection B.1.2. One should be cognizant of this fact when trying to validate the DORT equations (i.e. Equations B.24, B.26, B.35, and B.38).

The analysis in Chapter 6 could be made more general by explicitly investigating a case with multiple different scatterers, as opposed to just one scatterer. One could also do a similar analysis with vectorial—as opposed to scalar—waves.

The Holotorch simulation could also be made more accurate. Section 8.7 details ways in

²The MATLAB experiment code in Chapter 7 is available online. See “[Online Availability](#)” near the beginning of this thesis for more information on where to find the code.

which the simulation was limited in its accuracy. One avenue for exploration could be to use a different model for the aberrating layer. For instance, [31] gives a couple of possible alternative models. Another avenue for exploration could be to simulate vectorial waves³, as opposed to treating waves as scalar waves in the Holotorch simulations. One can refer to Section 8.7 for other potential means of improving the simulation.

Some other future work could be to, in simulation, try to image scatterers that are not small and discrete through aberrating media using SW-DORT. For example, one could try to image a scatterer that takes the form of a line as opposed to just a dot. This was attempted without much success and thus was not reported elsewhere in this thesis—however, perhaps further efforts would yield better results. Should one find success in simulation, one could then try to move on to real-life physical experiments.

Another potential future work is to do a physical experiment to demonstrate SW-DORT with small, discrete scatterers. In Chapter 8, the transfer matrix was obtained via simulation. However, using a real, measured transfer matrix would be desirable as there is always some mismatch between simulation and reality.⁴ If the experiment in Chapter 8 could be repeated with a real, measured transfer matrix, one would have experimental verification of SW-DORT. Thus, performing a similar experiment to that done in Chapter 8 in real-life with a physical setup⁵ and getting similar results to those reported in Chapter 8 would be a desirable next step.

³For an idea on how to do this, see Footnote 45 in Section 8.7.

⁴As an aside, there is also always some mismatch between measurement and reality as well.

⁵The backpropagation part of that experiment would still be done in simulation, however.

References

- [1] “Holofork.” <https://github.com/mich-lee/holofork>, 2023. Commit 16772c500acd761ab7756767b4167888257249d2.
- [2] F. Schiffers, O. S. Cossairt, and N. Matsuda, “Holotorch.” <https://github.com/facebookresearch/holotorch>, 2022. Commit cf1a80b3172684520b266cf03f9ba0163b5c1826.
- [3] M. Fink and C. Prada, *Detection and Imaging in Complex Media with the D.O.R.T. Method*, pp. 107–134. Springer Berlin Heidelberg, 2002. From the book titled *Imaging of Complex Media with acoustic and seismic waves*.
- [4] M. E. Yavuz, *Time reversal based signal processing techniques for ultrawideband electromagnetic sensing in random media*. PhD thesis, The Ohio State University, 2007.
- [5] J. W. Goodman, *Statistical Optics*. Wiley, 2nd ed., 2015. Sections 7.1.1 and 8.2.
- [6] S. Yoon, M. Kim, M. Jang, Y. Choi, W. Choi, S. Kang, and W. Choi, “Deep optical imaging within complex scattering media,” *Nature Reviews Physics*, vol. 2, p. 141–158, Feb 2020.
- [7] F. Willomitzer, P. V. Rangarajan, F. Li, M. M. Balaji, M. P. Christensen, and O. Cossairt, “Fast non-line-of-sight imaging with high-resolution and wide field of view using synthetic wavelength holography,” *Nature Communications*, vol. 12, p. 6647, Nov 2021.
- [8] A. Badon, D. Li, G. Lerosey, C. Boccara, M. Fink, and A. Aubry, “Overcoming multiple scattering for detection and imaging in strongly scattering media,” *Imaging and Applied Optics 2015*, 2015.
- [9] A. Badon, D. Li, G. Lerosey, A. C. Boccara, M. Fink, and A. Aubry, “Smart optical coherence tomography for ultra-deep imaging through highly scattering media,” *Science Advances*, vol. 2, Nov 2016.
- [10] C. A. Metzler, M. K. Sharma, S. Nagesh, R. G. Baraniuk, O. Cossairt, and A. Veeraraghavan, “Coherent inverse scattering via transmission matrices: Efficient phase retrieval algorithms and a public dataset,” *2017 IEEE International Conference on Computational Photography (ICCP)*, 2017.
- [11] A. Drémeau, A. Liutkus, D. Martina, O. Katz, C. Schülke, F. Krzakala, S. Gigan,

- and L. Daudet, “Reference-less measurement of the transmission matrix of a highly scattering material using a dmd and phase retrieval techniques,” *Optics Express*, vol. 23, no. 9, pp. 11898–11911, 2015.
- [12] M. K. Sharma, C. A. Metzler, S. Nagesh, R. G. Baraniuk, O. Cossairt, and A. Veeraraghavan, “Inverse scattering via transmission matrices: Broadband illumination and fast phase retrieval algorithms,” *IEEE Transactions on Computational Imaging*, vol. 6, p. 95–108, 2020.
- [13] S. M. Popoff, G. Lerosey, R. Carminati, M. Fink, A. C. Boccara, and S. Gigan, “Measuring the transmission matrix in optics: An approach to the study and control of light propagation in disordered media,” *Physical Review Letters*, vol. 104, no. 10, 2010.
- [14] A. Dubois, L. Vabre, A.-C. Boccara, and E. Beaurepaire, “High-resolution full-field optical coherence tomography with a linnik microscope,” *Applied Optics*, vol. 41, no. 4, p. 805, 2002.
- [15] A. Dremeau and F. Krzakala, “Phase recovery from a bayesian point of view: The variational approach,” *2015 IEEE International Conference on Acoustics, Speech and Signal Processing (ICASSP)*, 2015.
- [16] S. M. Popoff, A. Aubry, G. Lerosey, M. Fink, A. C. Boccara, and S. Gigan, “Exploiting the time-reversal operator for adaptive optics, selective focusing, and scattering pattern analysis,” *Physical Review Letters*, vol. 107, no. 26, 2011.
- [17] M. Fink, “Time reversal of ultrasonic fields - part i: Basic principles,” *IEEE Transactions on Ultrasonics, Ferroelectrics and Frequency Control*, vol. 39, no. 5, p. 555–566, 1992.
- [18] C. Prada and M. Fink, “Eigenmodes of the time reversal operator: A solution to selective focusing in multiple-target media,” *Wave Motion*, vol. 20, no. 2, p. 151–163, 1994.
- [19] M. Yavuz and F. Teixeira, “Ultrawideband microwave sensing and imaging using time-reversal techniques: A review,” *Remote Sensing*, vol. 1, no. 3, p. 466–495, 2009.
- [20] S. K. Hong, “Effects of target resonances on ultrawideband-dort,” *Journal of Electromagnetic Waves and Applications*, vol. 32, no. 13, p. 1710–1732, 2018.
- [21] C. Prada, S. Manneville, D. Spoliansky, and M. Fink, “Decomposition of the time reversal operator: Detection and selective focusing on two scatterers,” *The Journal of the Acoustical Society of America*, vol. 99, no. 4, p. 2067–2076, 1996.
- [22] J.-L. Robert, M. Burcher, C. Cohen-Bacrie, and M. Fink, “Time reversal operator decomposition with focused transmission and robustness to speckle noise: Application to microcalcification detection,” *The Journal of the Acoustical Society of America*, vol. 119, no. 6, p. 3848–3859, 2006.
- [23] J. M. Faia, K. W. McClintick, and S. K. Hong, “Application of dort and pulse inversion

- to detection and selective electromagnetic focusing on nonlinear elements," *32nd URSI General Assembly and Scientific Symposium of the International Union of Radio Science (URSI-GASS)*, 2017.
- [24] C. Prada, M. Tanter, and M. Fink, "Flaw detection in solid with the d.o.r.t. method," *1997 IEEE Ultrasonics Symposium Proceedings. An International Symposium (Cat. No.97CH36118)*, 1997.
 - [25] Y. Wu, F. Li, F. Willomitzer, A. Veeraraghavan, and O. Cossairt, "WISHED: Wave-front imaging sensor with high resolution and depth ranging," *2020 IEEE International Conference on Computational Photography (ICCP)*, 2020.
 - [26] H. Lev-Ari and A. J. Devaney, "The time-reversal technique re-interpreted: Subspace-based signal processing for multi-static target location," *Proceedings of the 2000 IEEE Sensor Array and Multichannel Signal Processing Workshop*, 2000.
 - [27] A. M. Smith, M. C. Mancini, and S. Nie, "Second window for in vivo imaging," *Nature Nanotechnology*, vol. 4, p. 710–711, Nov 2009.
 - [28] D. G. Voelz, *Computational Fourier Optics: A MATLAB Tutorial*. SPIE, 2011.
 - [29] R. Navarro, J. A. Méndez-Morales, and J. Santamaría, "Optical quality of the eye lens surfaces from roughness and diffusion measurements," *Journal of the Optical Society of America A*, vol. 3, p. 228–234, Feb 1986.
 - [30] "A review of surface roughness concepts, indices and applications -sate [sic] of the art-." Available at https://www.newfor.net/wp-content/uploads/2015/02/DL15-NEWFOR_Roughness_state_of_the_art.pdf.
 - [31] M. Qiao and X. Yuan, "Realistic phase screen model for forward multiple-scattering media," *Optics Letters*, vol. 45, p. 1031, Feb 2020.
 - [32] J. W. Goodman, *Introduction to Fourier Optics*. Roberts & Company Publishers, 3rd ed., 2005.
 - [33] J. D. Jackson, *Classical Electrodynamics*. Wiley, 3rd ed., 1999.

Appendices

Appendix A

Miscellaneous Appendix Sections

A.1 Green's function for the Helmholtz equation

Referring to Section 6.4 in [33], the inhomogeneous Helmholtz wave equation can be written as

$$(\nabla^2 + k^2) U(\vec{r}; \omega) = -4\pi f(\vec{r}; \omega) \quad (\text{A.1})$$

assuming a homogeneous, dispersionless, isotropic, and unbounded medium.¹ In Equation A.1, $k = \omega/v_{prop}$ is the wavenumber corresponding to the angular frequency ω , where v_{prop} is the speed of propagation in the medium. For a given k , one has a Green's function $G(\vec{r}, \vec{r}_{source}; \omega)$ which satisfies

$$(\nabla^2 + k^2) G(\vec{r}, \vec{r}_{source}; \omega) = -4\pi\delta(\vec{r} - \vec{r}_{source}). \quad (\text{A.2})$$

¹The author of this thesis is unsure about whether or not some of these assumptions—i.e. a homogeneous, dispersionless, and unbounded medium—are strictly necessary for Equation A.1 to be true. However, Section 6.4 of [33] makes these assumptions—i.e. a homogeneous, dispersionless, and unbounded medium—prior to giving its Equation 6.35, which is the equivalent of Equation A.1 in this thesis. Therefore, a homogeneous, dispersionless, unbounded medium is assumed here. In addition to the assumptions mentioned in [33]—i.e. a homogeneous, dispersionless, and unbounded medium—an isotropic medium is also assumed here as anisotropic behavior might otherwise complicate matters.

$G(\vec{r}, \vec{r}_{source}; \omega)$ has the general form

$$G(\vec{r}, \vec{r}_{source}; \omega) = A \frac{e^{+jk\|\vec{r} - \vec{r}_{source}\|}}{\|\vec{r} - \vec{r}_{source}\|} + B \frac{e^{-jk\|\vec{r} - \vec{r}_{source}\|}}{\|\vec{r} - \vec{r}_{source}\|} \quad (\text{A.3})$$

where $A + B = 1$. Assuming the convention that time phasors rotate *clockwise*², the $A \frac{e^{+jk\|\vec{r} - \vec{r}_{source}\|}}{\|\vec{r} - \vec{r}_{source}\|}$ term in Equation A.3 corresponds to an outgoing wave and the $B \frac{e^{-jk\|\vec{r} - \vec{r}_{source}\|}}{\|\vec{r} - \vec{r}_{source}\|}$ term in Equation A.3 corresponds to an incoming wave. If one assumes that one has a source that emits a wave, then $B = 0$ and Equation A.3 becomes

$$G(\vec{r}, \vec{r}_{source}; \omega) = \frac{e^{+jk\|\vec{r} - \vec{r}_{source}\|}}{\|\vec{r} - \vec{r}_{source}\|} \quad (\text{A.4})$$

since B was taken to be 0 and $A + B = 1$. It can also be noted that Equation A.4 is of the same form found in Equation 3-15 in [32].

A.2 Fields resulting from transmitting from transmitters

Suppose one had a sequence of points $(\vec{r}_i)_{i=1}^N$ corresponding to the locations of point sources, i.e. point sources of waves, and an observation point \vec{r} . Suppose one's medium was governed by a scalar wave equation, specifically the (scalar) Helmholtz equation given in Appendix Section A.1, $(\nabla^2 + k^2)U(\vec{r}; \omega) = -4\pi f(\vec{r}; \omega)$ —assuming a scalar wave equation of that form, and assuming a homogeneous, dispersionless, isotropic, and unbounded medium with sources that produce outgoing waves, one has Green's functions of the form $G(\vec{r}, \vec{r}_{source}; \omega) = \frac{\exp(+jk\|\vec{r} - \vec{r}_{source}\|)}{\|\vec{r} - \vec{r}_{source}\|}$ where $(\nabla^2 + k^2)G(\vec{r}, \vec{r}_{source}; \omega) = -4\pi\delta(\vec{r} - \vec{r}_{source})$, \vec{r} is an arbitrary observation location, and \vec{r}_{source} is an arbitrary source location.

One can make a column vector of the Green's functions going from sources at points

²Note that this is the convention taken in Section 6.4 in [33].

$(\vec{\mathbf{r}}_i)_{i=1}^N$ to the observation point $\vec{\mathbf{r}}$. Such a vector would look like

$$\vec{\mathbf{g}}(\vec{\mathbf{r}}; \omega) = \begin{bmatrix} \frac{\exp(+jkR_1)}{R_1} \\ \frac{\exp(+jkR_2)}{R_2} \\ \vdots \\ \frac{\exp(+jkR_N)}{R_N} \end{bmatrix} \quad (\text{A.5})$$

where $R_i = \|\vec{\mathbf{r}} - \vec{\mathbf{r}}_i\|$.

As an aside, note that by reciprocity, if the source points became observation points and the observation point became a source point, one would get the same vector of Green's functions as what is in Equation A.5, except Equation A.5 would be a vector representing the Green's functions going from a source at point $\vec{\mathbf{r}}$ to observation points at points $(\vec{\mathbf{r}}_i)_{i=1}^N$. Switching a source and observation point does not affect the Green's function in this case (i.e. the case of a scalar wave equation/scalar Helmholtz equation where the medium is homogeneous, dispersionless, isotropic, and unbounded) as $G(\vec{\mathbf{r}}, \vec{\mathbf{r}}_{source}; \omega) = G(\vec{\mathbf{r}}_{source}, \vec{\mathbf{r}}; \omega)$.³

Now, suppose that the sequence of point sources at $(\vec{\mathbf{r}}_i)_{i=1}^N$ has a corresponding sequence of complex amplitudes $(\tilde{A}_i(\omega))_{i=1}^N$. $f(\vec{\mathbf{r}}, \omega)$ in the inhomogeneous (scalar) Helmholtz equation $(\nabla^2 + k^2)U(\vec{\mathbf{r}}, \omega) = -4\pi f(\vec{\mathbf{r}}, \omega)$ would then become $f(\vec{\mathbf{r}}, \omega) = \sum_{i=1}^N \tilde{A}_i(\omega) \delta(\vec{\mathbf{r}} - \vec{\mathbf{r}}_i)$. For this $f(\vec{\mathbf{r}}, \omega)$, one has the field

$$U(\vec{\mathbf{r}}, \omega) = \sum_{i=1}^N \tilde{A}_i(\omega) G(\vec{\mathbf{r}}, \vec{\mathbf{r}}_i; \omega). \quad (\text{A.6})$$

Note that $U(\vec{\mathbf{r}}, \omega) = \sum_{i=1}^N \tilde{A}_i(\omega) G(\vec{\mathbf{r}}, \vec{\mathbf{r}}_i; \omega)$ is a solution of $(\nabla^2 + k^2)U(\vec{\mathbf{r}}, \omega) = -4\pi f(\vec{\mathbf{r}}, \omega)$

³This follows because $G(\vec{\mathbf{r}}, \vec{\mathbf{r}}_{source}; \omega) = \frac{\exp(+jk\|\vec{\mathbf{r}} - \vec{\mathbf{r}}_{source}\|)}{\|\vec{\mathbf{r}} - \vec{\mathbf{r}}_{source}\|}$ and $\|\vec{\mathbf{r}} - \vec{\mathbf{r}}_{source}\| = \|\vec{\mathbf{r}}_{source} - \vec{\mathbf{r}}\|$

for $f(\vec{\mathbf{r}}; \omega) = \sum_{i=1}^N \tilde{A}_i(\omega) \delta(\vec{\mathbf{r}} - \vec{\mathbf{r}}_i)$. This can be verified by noting that

$$\begin{aligned} (\nabla^2 + k^2) U(\vec{\mathbf{r}}; \omega) &= (\nabla^2 + k^2) \left[\sum_{i=1}^N \tilde{A}_i(\omega) G(\vec{\mathbf{r}}, \vec{\mathbf{r}}_i; \omega) \right] \\ &\vdots = \sum_{i=1}^N \tilde{A}_i(\omega) (\nabla^2 + k^2) G(\vec{\mathbf{r}}, \vec{\mathbf{r}}_i; \omega) \\ &\vdots = \sum_{i=1}^N \tilde{A}_i(\omega) [4\pi \delta(\vec{\mathbf{r}} - \vec{\mathbf{r}}_i)] \\ &\vdots = 4\pi \sum_{i=1}^N \tilde{A}_i(\omega) \delta(\vec{\mathbf{r}} - \vec{\mathbf{r}}_i) \\ (\nabla^2 + k^2) U(\vec{\mathbf{r}}; \omega) &= 4\pi f(\vec{\mathbf{r}}; \omega), \end{aligned}$$

where the fact that $(\nabla^2 + k^2) G(\vec{\mathbf{r}}, \vec{\mathbf{r}}_{source}; \omega) = -4\pi \delta(\vec{\mathbf{r}} - \vec{\mathbf{r}}_{source})$ for arbitrary source locations $\vec{\mathbf{r}}_{source}$ and the linearity of the $\nabla^2 + k^2$ operator was used.

Now, substituting in the expression for $G(\vec{\mathbf{r}}, \vec{\mathbf{r}}_i; \omega)$ into Equation A.6, one can write

$$U(\vec{\mathbf{r}}, \omega) = \sum_{i=1}^N \tilde{A}_i(\omega) \frac{\exp(+jkR_i)}{R_i} = \sum_{i=1}^N \tilde{A}_i(\omega) \frac{\exp(+jk\|\vec{\mathbf{r}} - \vec{\mathbf{r}}_i\|)}{\|\vec{\mathbf{r}} - \vec{\mathbf{r}}_i\|}, \quad (\text{A.7})$$

where $R_i = \|\vec{\mathbf{r}} - \vec{\mathbf{r}}_i\|$. Equivalently, from Equation A.7, the resulting field at point $\vec{\mathbf{r}}$ can be expressed as

$$U(\vec{\mathbf{r}}, \omega) = [\vec{\mathbf{g}}(\vec{\mathbf{r}}; \omega)]^\top \begin{bmatrix} \tilde{A}_1(\omega) \\ \tilde{A}_2(\omega) \\ \vdots \\ \tilde{A}_N(\omega) \end{bmatrix} = \begin{bmatrix} \exp(+jkR_1) & \frac{\exp(+jkR_2)}{R_2} & \dots & \frac{\exp(+jkR_N)}{R_N} \end{bmatrix} \begin{bmatrix} \tilde{A}_1(\omega) \\ \tilde{A}_2(\omega) \\ \vdots \\ \tilde{A}_N(\omega) \end{bmatrix}. \quad (\text{A.8})$$

where $\vec{\mathbf{g}}(\vec{\mathbf{r}}; \omega)$ was defined in Equation A.5.

Appendix B

Derivation of the DORT Equations

NOTE:

This section relies on definitions from Chapter 3. Please refer to that chapter as needed.

B.1 Derivation assumptions

This appendix section (Appendix Section B.1) will list out the assumptions that underlie the derivation in this appendix (Appendix B).

B.1.1 Basic assumptions

Suppose one had a transfer matrix $\mathbf{H}(\lambda)$ that related the fields transmitted by a set of transmitting transducers to the fields incident on a set of receiving transducers. Additionally, suppose that the transfer matrix follows the model described in Section 3.3, thus one can express $\mathbf{H}(\lambda)$ as $\mathbf{H}(\lambda) = \mathbf{B}(\lambda)\mathbf{S}(\lambda)\mathbf{F}(\lambda)$, where $\mathbf{B}(\lambda)$ is a $M \times D$ complex-valued matrix where $M \geq D$, $\mathbf{S}(\lambda)$ is a $D \times D$ complex-valued matrix, and $\mathbf{F}(\lambda)$ is a complex-valued $D \times N$ matrix where $N \geq D$. Consequently, $\mathbf{H}(\lambda)$ is an $M \times N$ matrix.

Also suppose that the scatterers are ideally-resolved (see Section 3.4 for a definition and more information on the term “ideally-resolved”). This means that $\mathbf{S}(\lambda)$ is a diagonal matrix, the rows of $\mathbf{F}(\lambda)$ are mutually orthogonal, and the columns of $\mathbf{B}(\lambda)$ are mutually orthogonal.

The ideally-resolved assumption also implies that none of the rows of $\mathbf{F}(\lambda)$ consist of all zeros, and none of the columns of $\mathbf{B}(\lambda)$ consist of all zeros.

B.1.2 An additional assumption

Under the assumptions given in the previous appendix subsection, Appendix Subsection B.1.1, for a given $\mathbf{H}(\lambda)$ where $\mathbf{H}(\lambda) = \mathbf{B}(\lambda)\mathbf{S}(\lambda)\mathbf{F}(\lambda)$, the matrices $\mathbf{F}(\lambda)$, $\mathbf{S}(\lambda)$, and $\mathbf{B}(\lambda)$ are not unique (assuming that $D > 1$). *In other words, one can have multiple different valid $\mathbf{F}(\lambda)$, $\mathbf{S}(\lambda)$, and $\mathbf{B}(\lambda)$ matrices that give the same transfer matrix $\mathbf{H}(\lambda)$.*

This is because in the previous appendix subsection, Appendix Subsection B.1.1, it was established that the $\mathbf{S}(\lambda)$ matrix was a diagonal matrix. Since $\mathbf{S}(\lambda)$ matrix is a diagonal matrix, by Theorem 5, the individual matrices in the product $\mathbf{B}(\lambda)\mathbf{S}(\lambda)\mathbf{F}(\lambda)$ can be rearranged while still giving the same overall product—put differently, there are multiple ways that one can structure the $\mathbf{F}(\lambda)$, $\mathbf{S}(\lambda)$, and $\mathbf{B}(\lambda)$ matrices while still satisfying $\mathbf{H}(\lambda) = \mathbf{B}(\lambda)\mathbf{S}(\lambda)\mathbf{F}(\lambda)$. This creates ambiguity in how to define these matrices.

Due to the fact that the singular value decomposition typically orders the singular values in decreasing order¹, it turns out that a specific “ordering”/structure is for $\mathbf{F}(\lambda)$, $\mathbf{S}(\lambda)$, and $\mathbf{B}(\lambda)$ is desirable. To articulate what this “desirable structure” is, let us first define “apparent reflectivity”. “Apparent reflectivity” was defined in [3], and using the notation of this thesis, is defined as

$$\rho_i(\lambda) = |S_{i,i}(\lambda)| \left(\sqrt{\sum_{\ell=1}^N |F_{i,\ell}(\lambda)|^2} \right) \left(\sqrt{\sum_{\ell=1}^M |B_{\ell,i}(\lambda)|^2} \right). \quad (\text{B.1})$$

The desirable structure is one where the apparent reflectivities are ordered in decreasing order (i.e. decreasing magnitude as one increases i). Note that the subscript i references specific locations in the $\mathbf{F}(\lambda)$, $\mathbf{S}(\lambda)$, and $\mathbf{B}(\lambda)$ matrices (see Equation B.1). Also note that

¹I.e. the diagonal elements of the $\Sigma(\lambda)$ matrix decrease as one goes from the upper-left to lower-right corner of that matrix.

the model should still make sense: for each $1 \leq i \in \mathbb{Z} \leq D$, $S_{i,i}(\lambda)$, $\mathbf{F}_{i,*}(\lambda)$, and $\mathbf{B}_{*,i}(\lambda)$ should all correspond to the same scatterer. Within that constraint, i.e. the one about $S_{i,i}(\lambda)$, $\mathbf{F}_{i,*}(\lambda)$, and $\mathbf{B}_{*,i}(\lambda)$ corresponding to the same scatterer, one should assume that $\mathbf{F}(\lambda)$, $\mathbf{S}(\lambda)$, and $\mathbf{B}(\lambda)$ are structured in such a way to get the aforementioned decreasing ordering of apparent reflectivities.

Now, finally, suppose that the matrices $\mathbf{F}(\lambda)$, $\mathbf{S}(\lambda)$, and $\mathbf{B}(\lambda)$ are structured in the manner described in the previous paragraph. Note that given any initial $\mathbf{F}(\lambda)$, $\mathbf{S}(\lambda)$, and $\mathbf{B}(\lambda)$, one can create that structure—this follows from Theorem 5.² Also note that assuming such a structure for $\mathbf{F}(\lambda)$, $\mathbf{S}(\lambda)$, and $\mathbf{B}(\lambda)$ is acceptable as the transfer matrix $\mathbf{H}(\lambda)$ /the product $\mathbf{H}(\lambda) = \mathbf{B}(\lambda)\mathbf{S}(\lambda)\mathbf{F}(\lambda)$ is typically the only entity that “exists”, insofar as $\mathbf{H}(\lambda)$ is typically the only matrix in $\mathbf{H}(\lambda) = \mathbf{B}(\lambda)\mathbf{S}(\lambda)\mathbf{F}(\lambda)$ that is directly measured. The rest, i.e. the individual $\mathbf{F}(\lambda)$, $\mathbf{S}(\lambda)$, and $\mathbf{B}(\lambda)$ matrices, are just models that are typically not directly measured—models that one is free to change provided that $\mathbf{H}(\lambda)$ remains unchanged. Thus, so long as $\mathbf{H}(\lambda)$ remains the same, one can choose whatever $\mathbf{F}(\lambda)$, $\mathbf{S}(\lambda)$, and $\mathbf{B}(\lambda)$ matrices are convenient, so long as the choices are still physically meaningful to one’s situation.

B.2 Rewriting various matrices/matrix products in different forms

In order to perform this derivation, it is necessary to express a number of matrices/matrix products in different forms. This appendix section (Appendix Section B.2) will derive these different forms.

²One can repeatedly do the “swapping” operation described in Theorem 5 to get the desired structure.

B.2.1 Part 1

One can decompose $\mathbf{H}(\lambda)$ as $\mathbf{H}(\lambda) = \mathbf{U}(\lambda)\Sigma(\lambda)\mathbf{V}(\lambda)$ using a singular value decomposition. The matrices $\mathbf{U}(\lambda)$ and $\mathbf{V}(\lambda)$ are unitary matrices, and the matrix $\Sigma(\lambda)$ is a non-negative, real-valued diagonal matrix.

Because $\mathbf{H}(\lambda) = \mathbf{U}(\lambda)\Sigma(\lambda)\mathbf{V}(\lambda)$ as per the singular value decomposition, it follows that

$$\mathbf{H}^\dagger(\lambda)\mathbf{H}(\lambda) = \mathbf{V}(\lambda)\Sigma^\dagger(\lambda)\Sigma(\lambda)\mathbf{V}^\dagger(\lambda) \quad (\text{B.2})$$

and

$$\mathbf{H}(\lambda)\mathbf{H}^\dagger(\lambda) = \mathbf{U}(\lambda)\Sigma(\lambda)\Sigma^\dagger(\lambda)\mathbf{U}^\dagger(\lambda). \quad (\text{B.3})$$

Note that the matrices $\Sigma^\dagger(\lambda)\Sigma(\lambda)$ and $\Sigma(\lambda)\Sigma^\dagger(\lambda)$ are diagonal matrices. Also note that $\mathbf{U}(\lambda)$, $\mathbf{U}^\dagger(\lambda)$, $\mathbf{V}(\lambda)$, and $\mathbf{V}^\dagger(\lambda)$ are unitary matrices.³

Now, let $\Lambda^{(v)}(\lambda) = \Sigma^\dagger(\lambda)\Sigma(\lambda)$ and $\Lambda^{(u)}(\lambda) = \Sigma(\lambda)\Sigma^\dagger(\lambda)$; then, substitute into Equations B.2 and B.3. This gives

$$\mathbf{H}^\dagger(\lambda)\mathbf{H}(\lambda) = \mathbf{V}(\lambda)\Lambda^{(v)}(\lambda)\mathbf{V}^\dagger(\lambda) \quad (\text{B.4})$$

and

$$\mathbf{H}(\lambda)\mathbf{H}^\dagger(\lambda) = \mathbf{U}(\lambda)\Lambda^{(u)}(\lambda)\mathbf{U}^\dagger(\lambda). \quad (\text{B.5})$$

Since $\mathbf{H}(\lambda)$ is an $M \times N$ matrix, the matrix $\Sigma(\lambda)$ obtained from taking the singular value decomposition of $\mathbf{H}(\lambda)$ must be, by definition, an $M \times N$ matrix. Thus, since $\Lambda^{(v)}(\lambda) = \Sigma^\dagger(\lambda)\Sigma(\lambda)$ and $\Lambda^{(u)}(\lambda) = \Sigma(\lambda)\Sigma^\dagger(\lambda)$, the matrices $\Lambda^{(v)}(\lambda)$ and $\Lambda^{(u)}(\lambda)$ have dimensions $N \times N$ and $M \times M$ respectively.

³By the definition of the singular value decomposition, $\mathbf{U}(\lambda)$ and $\mathbf{V}(\lambda)$ are unitary matrices. The conjugate transpose of a unitary matrix is also a unitary matrix, so $\mathbf{U}^\dagger(\lambda)$ and $\mathbf{V}^\dagger(\lambda)$ are unitary matrices as well.

Applying Theorem 6 to $\Lambda^{(v)}(\lambda) = \Sigma^\dagger(\lambda)\Sigma(\lambda)$ and $\Lambda^{(u)}(\lambda) = \Sigma(\lambda)\Sigma^\dagger(\lambda)$ gives⁴

$$\Lambda_{i,j}^{(v)}(\lambda) = \begin{cases} \Sigma_{i,i}^2(\lambda), & \text{for } (i = j) \wedge [i, j \leq \min(M, N)] \\ 0, & \text{otherwise} \end{cases}, \quad \text{where } (i, j \in \mathbb{Z}) \wedge (1 \leq i, j \leq N), \quad (\text{B.6})$$

and

$$\Lambda_{i,j}^{(u)}(\lambda) = \begin{cases} \Sigma_{i,i}^2(\lambda), & \text{for } (i = j) \wedge [i, j \leq \min(M, N)] \\ 0, & \text{otherwise} \end{cases}, \quad \text{where } (i, j \in \mathbb{Z}) \wedge (1 \leq i, j \leq M). \quad (\text{B.7})$$

Note that for $\Lambda_{i,j}^{(v)}(\lambda)$ in Equation B.6, the i and j indices are integers ranging from 1 to N ; in contrast, for $\Lambda_{i,j}^{(u)}(\lambda)$ in Equation B.7, the i and j indices are integers ranging from 1 to M .

B.2.2 Part 2

Since $\mathbf{H}(\lambda) = \mathbf{B}(\lambda)\mathbf{S}(\lambda)\mathbf{F}(\lambda)$ (as stated in Appendix Subsection B.1.1), we can write

$$\mathbf{H}^\dagger(\lambda)\mathbf{H}(\lambda) = \mathbf{F}^\dagger(\lambda)\mathbf{S}^\dagger(\lambda)\mathbf{B}^\dagger(\lambda)\mathbf{B}(\lambda)\mathbf{S}(\lambda)\mathbf{F}(\lambda) \quad (\text{B.8})$$

and

$$\mathbf{H}(\lambda)\mathbf{H}^\dagger(\lambda) = \mathbf{B}(\lambda)\mathbf{S}(\lambda)\mathbf{F}(\lambda)\mathbf{F}^\dagger(\lambda)\mathbf{S}^\dagger(\lambda)\mathbf{B}^\dagger(\lambda). \quad (\text{B.9})$$

These equations can be simplified. To start, first note that $\mathbf{F}(\lambda)$ can be written as $\mathbf{F}(\lambda) = \Delta^{(f)}(\lambda)\hat{\mathbf{F}}(\lambda)$ where $\Delta^{(f)}(\lambda)$ is a $D \times D$ matrix and is defined element-wise as

$$\Delta_{i,j}^{(f)}(\lambda) = \begin{cases} \sqrt{\sum_{\ell=1}^N |F_{i,\ell}(\lambda)|^2}, & \text{for } i = j \\ 0, & \text{for } i \neq j \end{cases} \quad (\text{B.10})$$

⁴This step is done by noting that $\Sigma(\lambda)$ is a non-negative real-valued diagonal matrix and making simplifications based on that.

and the rows of $\hat{\mathbf{F}}(\lambda)$ are defined as $\hat{\mathbf{F}}_{k,*}(\lambda) = \mathbf{F}_{k,*}(\lambda)/\Delta_{k,k}^{(f)}(\lambda)$. Similarly, $\mathbf{B}(\lambda)$ can be written as $\mathbf{B}(\lambda) = \hat{\mathbf{B}}(\lambda)\Delta^{(b)}(\lambda)$ where $\Delta^{(b)}(\lambda)$ is a $D \times D$ matrix and is defined element-wise as

$$\Delta_{i,j}^{(b)}(\lambda) = \begin{cases} \sqrt{\sum_{\ell=1}^M |B_{\ell,j}(\lambda)|^2}, & \text{for } i = j \\ 0, & \text{for } i \neq j \end{cases} \quad (\text{B.11})$$

and the columns of $\hat{\mathbf{B}}(\lambda)$ are defined as $\hat{\mathbf{B}}_{*,k}(\lambda) = \mathbf{B}_{*,k}(\lambda)/\Delta_{k,k}^{(b)}(\lambda)$.⁵ It should be noted that because of the ideally-resolved assumption, none of the rows of $\mathbf{F}(\lambda)$ and none of the columns of $\mathbf{B}(\lambda)$ consist solely of zeros, which implies that $\Delta_{k,k}^{(f)}(\lambda) \neq 0$ and $\Delta_{k,k}^{(b)}(\lambda) \neq 0$ —thus, one does not run into any division-by-zero issues when defining $\hat{\mathbf{F}}(\lambda)$ and $\hat{\mathbf{B}}(\lambda)$.

Now, as per the previous definitions, the rows (resp. columns) of $\hat{\mathbf{F}}(\lambda)$ (resp. $\hat{\mathbf{B}}(\lambda)$) are normalized. Moreover, because of the ideally-resolved scatterer assumption, the rows (resp. columns) of $\hat{\mathbf{F}}(\lambda)$ (resp. $\hat{\mathbf{B}}(\lambda)$) are mutually orthogonal.

Because $\hat{\mathbf{F}}(\lambda)$ has mutually orthogonal rows with unit magnitude, it follows that $\hat{\mathbf{F}}(\lambda)\hat{\mathbf{F}}^\dagger(\lambda)$ is the $D \times D$ identity matrix. Similarly, because $\hat{\mathbf{B}}(\lambda)$ has mutually orthogonal columns with unit magnitude, it follows that $\hat{\mathbf{B}}^\dagger(\lambda)\hat{\mathbf{B}}(\lambda)$ is the $D \times D$ identity matrix.

One can substitute $\mathbf{F}(\lambda) = \Delta^{(f)}(\lambda)\hat{\mathbf{F}}(\lambda)$ and $\mathbf{B}(\lambda) = \hat{\mathbf{B}}(\lambda)\Delta^{(b)}(\lambda)$ into Equations B.8 and B.9, and make use of the facts stated in the previous paragraph. After doing so, it can be seen that $\mathbf{H}^\dagger(\lambda)\mathbf{H}(\lambda)$ can be simplified to

$$\mathbf{H}^\dagger(\lambda)\mathbf{H}(\lambda) = \hat{\mathbf{F}}^\dagger(\lambda)\Lambda^{(f)}(\lambda)\hat{\mathbf{F}}(\lambda) \quad (\text{B.12})$$

where $\Lambda^{(f)}(\lambda) = [\Delta^{(f)}(\lambda)]^\dagger \mathbf{S}^\dagger(\lambda) [\Delta^{(b)}(\lambda)]^\dagger \Delta^{(b)}(\lambda) \mathbf{S}(\lambda) \Delta^{(f)}(\lambda)$. Similarly, $\mathbf{H}(\lambda)\mathbf{H}^\dagger(\lambda)$ can be simplified to

$$\mathbf{H}(\lambda)\mathbf{H}^\dagger(\lambda) = \hat{\mathbf{B}}(\lambda)\Lambda^{(b)}(\lambda)\hat{\mathbf{B}}^\dagger(\lambda) \quad (\text{B.13})$$

where $\Lambda^{(b)}(\lambda) = \Delta^{(b)}(\lambda)\mathbf{S}(\lambda)\Delta^{(f)}(\lambda) [\Delta^{(f)}(\lambda)]^\dagger \mathbf{S}^\dagger(\lambda) [\Delta^{(b)}(\lambda)]^\dagger$. It should be noted that, as

⁵The step of factoring matrices as $\mathbf{F}(\lambda) = \Delta^{(f)}(\lambda)\hat{\mathbf{F}}(\lambda)$ and $\mathbf{B}(\lambda) = \hat{\mathbf{B}}(\lambda)\Delta^{(b)}(\lambda)$ was done in [3].

per earlier definitions, $\Lambda^{(f)}(\lambda)$ and $\Lambda^{(b)}(\lambda)$ are diagonal matrices with dimensions $D \times D$.

Note that the matrices $\hat{\mathbf{F}}(\lambda)$ and $\hat{\mathbf{B}}(\lambda)$ are ***not*** unitary matrices because they are not square matrices. However, applying Theorem 4 and Corollary 4.1 to Equations B.12 and B.13 respectively, one can choose matrices $\tilde{\mathbf{F}}(\lambda)$, $\tilde{\mathbf{B}}(\lambda)$, $\tilde{\Lambda}^{(f)}(\lambda)$, and $\tilde{\Lambda}^{(b)}(\lambda)$ that satisfy $\mathbf{H}^\dagger(\lambda)\mathbf{H}(\lambda) = \hat{\mathbf{F}}^\dagger(\lambda)\Lambda^{(f)}(\lambda)\hat{\mathbf{F}}(\lambda) = \tilde{\mathbf{F}}^\dagger(\lambda)\tilde{\Lambda}^{(f)}(\lambda)\tilde{\mathbf{F}}(\lambda)$ and $\mathbf{H}(\lambda)\mathbf{H}^\dagger(\lambda) = \hat{\mathbf{B}}(\lambda)\Lambda^{(b)}(\lambda)\hat{\mathbf{B}}^\dagger(\lambda) = \tilde{\mathbf{B}}(\lambda)\tilde{\Lambda}^{(b)}(\lambda)\tilde{\mathbf{B}}^\dagger(\lambda)$. $\tilde{\mathbf{F}}(\lambda)$ can be created by “padding” $\hat{\mathbf{F}}(\lambda)$ with orthonormal row vectors that span the orthogonal complement of the image of $f : \vec{\mathbf{x}} \mapsto \vec{\mathbf{x}}\hat{\mathbf{F}}(\lambda)$,⁶ where $\vec{\mathbf{x}}$ is a row vector, thus making $\tilde{\mathbf{F}}(\lambda)$ $N \times N$ in dimension. Similarly, $\tilde{\mathbf{B}}(\lambda)$ can be created by “padding” $\hat{\mathbf{B}}(\lambda)$ with orthonormal column vectors that span the orthogonal complement of the image of $f : \vec{\mathbf{x}} \mapsto \hat{\mathbf{B}}(\lambda)\vec{\mathbf{x}}$,⁷ where $\vec{\mathbf{x}}$ is a column vector, thus making $\tilde{\mathbf{B}}(\lambda)$ $M \times M$ in dimension. We shall choose to “pad” $\hat{\mathbf{F}}(\lambda)$ and $\hat{\mathbf{B}}(\lambda)$ in this previously defined manner to create $\tilde{\mathbf{F}}(\lambda)$ and $\tilde{\mathbf{B}}(\lambda)$.⁸

Since $\hat{\mathbf{F}}(\lambda)$ has orthonormal rows and $\hat{\mathbf{B}}(\lambda)$ has orthonormal columns, and the padded rows in $\tilde{\mathbf{F}}(\lambda)$ and padded columns in $\tilde{\mathbf{B}}(\lambda)$ are orthonormal vectors in the orthogonal complements of the images of $f : \vec{\mathbf{x}} \mapsto \vec{\mathbf{x}}\hat{\mathbf{F}}(\lambda)$ and $f : \vec{\mathbf{x}} \mapsto \hat{\mathbf{B}}(\lambda)\vec{\mathbf{x}}$ respectively—so the padded rows in $\tilde{\mathbf{F}}(\lambda)$ and padded columns in $\tilde{\mathbf{B}}(\lambda)$ are orthogonal to the rows of $\hat{\mathbf{F}}(\lambda)$ and columns of $\hat{\mathbf{B}}(\lambda)$ respectively—the rows and columns of $\tilde{\mathbf{F}}(\lambda)$ and $\tilde{\mathbf{B}}(\lambda)$ respectively are orthonormal. This means that $\tilde{\mathbf{F}}(\lambda)$ and $\tilde{\mathbf{B}}(\lambda)$ are ***unitary*** matrices. Additionally, $\tilde{\Lambda}^{(f)}(\lambda)$ and $\tilde{\Lambda}^{(b)}(\lambda)$ can, and shall, be created by padding $\Lambda^{(f)}(\lambda)$ and $\Lambda^{(b)}(\lambda)$ with zeros so that they are $N \times N$ and $M \times M$ in size respectively. Note that the aforementioned padding for $\tilde{\mathbf{F}}(\lambda)$, $\tilde{\mathbf{B}}(\lambda)$, $\tilde{\Lambda}^{(f)}(\lambda)$, and $\tilde{\Lambda}^{(b)}(\lambda)$ is done by padding the right and/or bottom parts of the matrices that they are derived from—the upper-left parts (that are not padding) of the matrices equal the original matrices.

It should be noted that substituting $\hat{\mathbf{F}}(\lambda)$, $\hat{\mathbf{B}}(\lambda)$, $\Lambda^{(f)}(\lambda)$, and $\Lambda^{(b)}(\lambda)$ with $\tilde{\mathbf{F}}(\lambda)$, $\tilde{\mathbf{B}}(\lambda)$,

⁶The image of $f : \vec{\mathbf{x}} \mapsto \vec{\mathbf{x}}\hat{\mathbf{F}}(\lambda)$ is the span of the rows of $\hat{\mathbf{F}}(\lambda)$.

⁷The image of $f : \vec{\mathbf{x}} \mapsto \hat{\mathbf{B}}(\lambda)\vec{\mathbf{x}}$ is the span of the columns of $\hat{\mathbf{B}}(\lambda)$.

⁸By Theorem 4 and Corollary 4.1, the “padding” can be arbitrary. Choosing to “pad” $\hat{\mathbf{F}}(\lambda)$ and $\hat{\mathbf{B}}(\lambda)$ in the manner described to create $\tilde{\mathbf{F}}(\lambda)$ and $\tilde{\mathbf{B}}(\lambda)$ was done for convenience as it would make $\tilde{\mathbf{F}}(\lambda)$ and $\tilde{\mathbf{B}}(\lambda)$ unitary matrices, which will be convenient later on in the proof. For justification on why $\tilde{\mathbf{F}}(\lambda)$ and $\tilde{\mathbf{B}}(\lambda)$ unitary matrices, see the next paragraph.

$\tilde{\Lambda}^{(f)}(\lambda)$, and $\tilde{\Lambda}^{(b)}(\lambda)$ respectively in Equations B.12 and B.13 is valid as the matrix products $\mathbf{H}^\dagger(\lambda)\mathbf{H}(\lambda)$ and $\mathbf{H}(\lambda)\mathbf{H}^\dagger(\lambda)$ remain unchanged—this follows from Theorem 4 and Corollary 4.1 combined with what was established previously. Making such substitutions into Equations B.12 and B.13 gives

$$\mathbf{H}^\dagger(\lambda)\mathbf{H}(\lambda) = \tilde{\mathbf{F}}^\dagger(\lambda)\tilde{\Lambda}^{(f)}(\lambda)\tilde{\mathbf{F}}(\lambda) \quad (\text{B.14})$$

and

$$\mathbf{H}(\lambda)\mathbf{H}^\dagger(\lambda) = \tilde{\mathbf{B}}(\lambda)\tilde{\Lambda}^{(b)}(\lambda)\tilde{\mathbf{B}}^\dagger(\lambda). \quad (\text{B.15})$$

Now, note that the diagonal elements of the diagonal matrices $\tilde{\Lambda}^{(f)}(\lambda)$ and $\tilde{\Lambda}^{(b)}(\lambda)$ are ordered in order of decreasing magnitude (with the upper-leftmost diagonal element having the greatest magnitude). This ordering naturally arises under the assumptions in Appendix Subsection B.1.2 in combination with how $\tilde{\Lambda}^{(f)}(\lambda)$ and $\tilde{\Lambda}^{(b)}(\lambda)$ were defined. Ordering in order of decreasing apparent reflectivity (as described/defined in Appendix Subsection B.1.2) implicitly gives the “correct” ordering on $\Lambda^{(f)}(\lambda) = [\Delta^{(f)}(\lambda)]^\dagger \mathbf{S}^\dagger(\lambda) [\Delta^{(b)}(\lambda)]^\dagger \Delta^{(b)}(\lambda) \mathbf{S}(\lambda) \Delta^{(f)}(\lambda)$ and $\Lambda^{(b)}(\lambda) = \Delta^{(b)}(\lambda) \mathbf{S}(\lambda) \Delta^{(f)}(\lambda) [\Delta^{(f)}(\lambda)]^\dagger \mathbf{S}^\dagger(\lambda) [\Delta^{(b)}(\lambda)]^\dagger$. It can be seen that the diagonal elements of $\Lambda^{(f)}(\lambda)$ and $\Lambda^{(b)}(\lambda)$ are just the squares of the apparent reflectivities, and that following the ordering described in Appendix Subsection B.1.2 orders the aforementioned diagonal elements in order of decreasing magnitude going from the top left to the bottom right of the matrices—see the definition of the constituent matrices in the matrix products $\Lambda^{(f)}(\lambda) = [\Delta^{(f)}(\lambda)]^\dagger \mathbf{S}^\dagger(\lambda) [\Delta^{(b)}(\lambda)]^\dagger \Delta^{(b)}(\lambda) \mathbf{S}(\lambda) \Delta^{(f)}(\lambda)$ and $\Lambda^{(b)}(\lambda) = \Delta^{(b)}(\lambda) \mathbf{S}(\lambda) \Delta^{(f)}(\lambda) [\Delta^{(f)}(\lambda)]^\dagger \mathbf{S}^\dagger(\lambda) [\Delta^{(b)}(\lambda)]^\dagger$ and the definition of apparent reflectivity, given in Equation B.1 in Appendix Subsection B.1.2, to verify this. Furthermore, the padding of $\Lambda^{(f)}(\lambda)$ and $\Lambda^{(b)}(\lambda)$ that is done to get $\tilde{\Lambda}^{(f)}(\lambda)$ and $\tilde{\Lambda}^{(b)}(\lambda)$ does not affect the ordering since the padding elements in $\tilde{\Lambda}^{(f)}(\lambda)$ and $\tilde{\Lambda}^{(b)}(\lambda)$ are equal to zero, the padding is on the right and bottom parts of the matrices, and the (diagonal) elements of $\Lambda^{(f)}(\lambda)$ and $\Lambda^{(b)}(\lambda)$ are non-negative by definition. Thus, $\tilde{\Lambda}^{(f)}(\lambda)$ and $\tilde{\Lambda}^{(b)}(\lambda)$ have the aforementioned

ordering of diagonal elements under the assumptions in Appendix Subsection B.1.2.

Also note that the first D diagonal entries of $\tilde{\Lambda}^{(f)}(\lambda)$ and $\tilde{\Lambda}^{(b)}(\lambda)$ equal the first D diagonal entries of $\Lambda^{(f)}(\lambda)$ and $\Lambda^{(b)}(\lambda)$ respectively, the first D rows of $\tilde{\mathbf{F}}(\lambda)$ equal the first D rows of $\hat{\mathbf{F}}(\lambda)$, and the first D columns of $\tilde{\mathbf{B}}(\lambda)$ equal the first D columns of $\hat{\mathbf{B}}(\lambda)$. This follows from how $\tilde{\mathbf{F}}(\lambda)$, $\tilde{\mathbf{B}}(\lambda)$, $\tilde{\Lambda}^{(f)}(\lambda)$, and $\tilde{\Lambda}^{(b)}(\lambda)$ were defined.

B.3 Some setup

Before moving on, some facts will be established in this appendix section (Appendix Section B.3). These facts will help in the derivation.

B.3.1 Eigenvalues and eigenvectors for matrices

In Appendix Section B.2, various matrices and matrix products were rewritten in alternate forms. These alternate forms will prove useful for the next parts of this derivation.

Before moving on with the derivation, however, certain facts need to be established. This appendix subsection will establish some of these facts.

Applying Theorem 1 to Equation B.14, it can be seen that $\left(\left(\tilde{\mathbf{F}}_{i,*}^*(\lambda)\right)^\top\right)_{i=1}^N$ are eigenvectors of $\mathbf{H}^\dagger(\lambda)\mathbf{H}(\lambda)$ associated with eigenvalues $\left(\tilde{\Lambda}_{i,i}^{(f)}(\lambda)\right)_{i=1}^N$, where each vector $\left(\tilde{\mathbf{F}}_{i,*}^*(\lambda)\right)^\top$ is an eigenvector of $\mathbf{H}^\dagger(\lambda)\mathbf{H}(\lambda)$ and is associated with the eigenvalue $\tilde{\Lambda}_{i,i}^{(f)}(\lambda)$. Applying Corollary 1.1 to Equation B.4, it can be seen that $\left(\mathbf{V}_{*,i}(\lambda)\right)_{i=1}^N$ are eigenvectors of $\mathbf{H}^\dagger(\lambda)\mathbf{H}(\lambda)$ associated with eigenvalues $\left(\Lambda_{i,i}^{(v)}(\lambda)\right)_{i=1}^N$, where each vector $\mathbf{V}_{*,i}(\lambda)$ is an eigenvector of $\mathbf{H}^\dagger(\lambda)\mathbf{H}(\lambda)$ and is associated with the eigenvalue $\Lambda_{i,i}^{(v)}(\lambda)$. Note that the sequences of eigenvalues $\left(\tilde{\Lambda}_{i,i}^{(f)}(\lambda)\right)_{i=1}^N$ and $\left(\Lambda_{i,i}^{(v)}(\lambda)\right)_{i=1}^N$ contain the same elements⁹ as those sequences both contain the eigenvalues for the matrix $\mathbf{H}^\dagger(\lambda)\mathbf{H}(\lambda)$. Additionally, note that $\mathbf{H}^\dagger(\lambda)\mathbf{H}(\lambda)$ has N eigenvalues.

Similarly, applying Corollary 1.1 to Equation B.15, it can be seen that $\left(\tilde{\mathbf{B}}_{*,i}(\lambda)\right)_{i=1}^M$

⁹Not necessarily in the same order, at least at this point in the derivation.

are eigenvectors of $\mathbf{H}(\lambda)\mathbf{H}^\dagger(\lambda)$ associated with eigenvalues $\left(\tilde{\Lambda}_{i,i}^{(b)}(\lambda)\right)_{i=1}^M$, where each vector $\tilde{\mathbf{B}}_{*,i}(\lambda)$ is an eigenvector of $\mathbf{H}(\lambda)\mathbf{H}^\dagger(\lambda)$ and is associated with the eigenvalue $\tilde{\Lambda}_{i,i}^{(b)}(\lambda)$. Applying Corollary 1.1 to Equation B.5, it can be seen that $\left(\mathbf{U}_{*,i}(\lambda)\right)_{i=1}^M$ are eigenvectors of $\mathbf{H}(\lambda)\mathbf{H}^\dagger(\lambda)$ associated with eigenvalues $\left(\Lambda_{i,i}^{(u)}(\lambda)\right)_{i=1}^M$, where each vector $\mathbf{U}_{*,i}(\lambda)$ is an eigenvector and is associated with the eigenvalue $\Lambda_{i,i}^{(u)}(\lambda)$. Note that the sequences of eigenvalues $\left(\tilde{\Lambda}_{i,i}^{(b)}(\lambda)\right)_{i=1}^M$ and $\left(\Lambda_{i,i}^{(u)}(\lambda)\right)_{i=1}^M$ contain the same elements¹⁰ as those sequences both contain the eigenvalues for the matrix $\mathbf{H}(\lambda)\mathbf{H}^\dagger(\lambda)$. Additionally, note that $\mathbf{H}(\lambda)\mathbf{H}^\dagger(\lambda)$ has M eigenvalues.

Now assume the standard convention for singular value decomposition, which orders the singular values in the $\Sigma(\lambda)$ matrix in order of decreasing magnitude going from the upper-leftmost corner to the lower-rightmost corner. Assuming that convention, it follows from Equations B.6 and B.7 that the diagonal entries of $\Lambda^{(v)}(\lambda)$ and $\Lambda^{(u)}(\lambda)$ are ordered in order of decreasing magnitude going from the upper-leftmost corner to the lower-rightmost corner. Also recall that by construction, the diagonal elements of $\tilde{\Lambda}^{(f)}(\lambda)$ and $\tilde{\Lambda}^{(b)}(\lambda)$ are arranged in order of decreasing magnitude.

Since the sequences of eigenvalues $\left(\tilde{\Lambda}_{i,i}^{(f)}(\lambda)\right)_{i=1}^N$ and $\left(\Lambda_{i,i}^{(v)}(\lambda)\right)_{i=1}^N$ contain the same elements and, as per the previous paragraph, these sequences are both ordered in order of decreasing magnitude, it follows that $\tilde{\Lambda}_{i,i}^{(f)}(\lambda) = \Lambda_{i,i}^{(v)}(\lambda)$ for $1 \leq i \in \mathbb{Z} \leq N$. Similarly, since the sequences of eigenvalues $\left(\tilde{\Lambda}_{i,i}^{(b)}(\lambda)\right)_{i=1}^M$ and $\left(\Lambda_{i,i}^{(u)}(\lambda)\right)_{i=1}^M$ contain the same elements and, as per the previous paragraph, these sequences are both ordered in order of decreasing magnitude, it follows that $\tilde{\Lambda}_{i,i}^{(b)}(\lambda) = \Lambda_{i,i}^{(u)}(\lambda)$ for $1 \leq i \in \mathbb{Z} \leq M$.

Because $\tilde{\Lambda}_{i,i}^{(f)}(\lambda) = \Lambda_{i,i}^{(v)}(\lambda)$, and because the eigenvectors $(\tilde{\mathbf{F}}_{i,*}^*(\lambda))^\top$ and $\mathbf{V}_{*,i}(\lambda)$ correspond to eigenvalues $\tilde{\Lambda}_{i,i}^{(f)}(\lambda)$ and $\Lambda_{i,i}^{(v)}(\lambda)$ respectively, the eigenvectors $(\tilde{\mathbf{F}}_{i,*}^*(\lambda))^\top$ and $\mathbf{V}_{*,i}(\lambda)$ correspond to the same eigenvalue—denote this eigenvalue as $\lambda_i^{(fv)}(\lambda)$, where $\lambda_i^{(fv)}(\lambda) = \tilde{\Lambda}_{i,i}^{(f)}(\lambda) = \Lambda_{i,i}^{(v)}(\lambda)$.

Additionally, because $\tilde{\Lambda}_{i,i}^{(b)}(\lambda) = \Lambda_{i,i}^{(u)}(\lambda)$, and because the eigenvectors $\tilde{\mathbf{B}}_{*,i}(\lambda)$ and $\mathbf{U}_{*,i}(\lambda)$

¹⁰Not necessarily in the same order, at least at this point in the derivation.

correspond to eigenvalues $\tilde{\Lambda}_{i,i}^{(b)}(\lambda)$ and $\Lambda_{i,i}^{(u)}(\lambda)$ respectively, the eigenvectors $\tilde{\mathbf{B}}_{*,i}(\lambda)$ and $\mathbf{U}_{*,i}(\lambda)$ correspond to the same eigenvalue—denote this eigenvalue as $\lambda_i^{(bu)}(\lambda)$, where $\lambda_i^{(bu)}(\lambda) = \tilde{\Lambda}_{i,i}^{(b)}(\lambda) = \Lambda_{i,i}^{(u)}(\lambda)$.

B.3.2 Relating singular values to eigenvalues

Recall from Appendix Subsection B.2.2 that $\tilde{\Lambda}^{(f)}(\lambda)$ and $\tilde{\Lambda}^{(b)}(\lambda)$ were created by padding the $D \times D$ diagonal matrices $\Lambda^{(f)}(\lambda)$ and $\Lambda^{(b)}(\lambda)$ with zeros on the right, bottom, and bottom-right sides. This means that $\tilde{\Lambda}^{(f)}(\lambda)$ and $\tilde{\Lambda}^{(b)}(\lambda)$ have at most D non-zero diagonal entries, and that those diagonal entries are located in the upper $D \times D$ quadrants of the matrices. Now recall that $\lambda_i^{(fv)}(\lambda) = \tilde{\Lambda}_{i,i}^{(f)}(\lambda) = \Lambda_{i,i}^{(v)}(\lambda)$ and $\lambda_i^{(bu)}(\lambda) = \tilde{\Lambda}_{i,i}^{(b)}(\lambda) = \Lambda_{i,i}^{(u)}(\lambda)$ (see Appendix Subsection B.3.1). Combining the facts stated in this paragraph with Equations B.6 and B.7 gives

$$\tilde{\Lambda}_{i,j}^{(f)}(\lambda) = \Lambda_{i,j}^{(v)}(\lambda) = \begin{cases} \Sigma_{i,i}^2(\lambda), & \text{for } (i = j) \wedge (i, j \leq D) \\ 0, & \text{otherwise} \end{cases}, \quad \text{where } (i, j \in \mathbb{Z}) \wedge (1 \leq i, j \leq N), \quad (\text{B.16})$$

and

$$\tilde{\Lambda}_{i,j}^{(b)}(\lambda) = \Lambda_{i,j}^{(u)}(\lambda) = \begin{cases} \Sigma_{i,i}^2(\lambda), & \text{for } (i = j) \wedge (i, j \leq D) \\ 0, & \text{otherwise} \end{cases}, \quad \text{where } (i, j \in \mathbb{Z}) \wedge (1 \leq i, j \leq M), \quad (\text{B.17})$$

as well as

$$\lambda_i^{(fv)}(\lambda) = \tilde{\Lambda}_{i,i}^{(f)}(\lambda) = \Lambda_{i,i}^{(v)}(\lambda) = \begin{cases} \Sigma_{i,i}^2(\lambda), & \text{for } i \leq D \\ \Sigma_{i,i}^2(\lambda) = 0, & \text{for } D < i \leq \min(M, N) \\ 0, & \text{for } \min(M, N) < i \leq N \end{cases}, \quad (\text{B.18})$$

and

$$\lambda_i^{(bu)}(\lambda) = \tilde{\Lambda}_{i,i}^{(b)}(\lambda) = \Lambda_{i,i}^{(u)}(\lambda) = \begin{cases} \Sigma_{i,i}^2(\lambda), & \text{for } i \leq D \\ \Sigma_{i,i}^2(\lambda) = 0, & \text{for } D < i \leq \min(M, N) \\ 0, & \text{for } \min(M, N) < i \leq M \end{cases}. \quad (\text{B.19})$$

Thus, $\mathbf{H}^\dagger(\lambda)\mathbf{H}(\lambda)$ has N eigenvalues, but only D non-zero eigenvalues. Similarly, $\mathbf{H}(\lambda)\mathbf{H}^\dagger(\lambda)$ has M eigenvalues, but only D non-zero eigenvalues.

Furthermore, for both $\mathbf{H}^\dagger(\lambda)\mathbf{H}(\lambda)$ and $\mathbf{H}(\lambda)\mathbf{H}^\dagger(\lambda)$, the eigenvalues are related to the singular values of $\mathbf{H}(\lambda)$ in the manner shown in Equations B.18 and B.19. Additionally, comparing Equations B.6 and B.7 to Equations B.16 and B.17, it can be seen that any singular values $\Sigma_{i,i}(\lambda)$ that are numbered above D have a value of 0—thus, only the first D singular values can be¹¹ non-zero; the remaining $\min(M, N) - D$ singular values must be 0 in value.

B.4 Deriving expressions for the singular vectors

B.4.1 Deriving an expression for the right-singular vectors

Let $\vec{x}_i(\lambda) = \left(\tilde{\mathbf{F}}_{i,*}^*(\lambda)\right)^\top$ be the complex conjugate of the i^{th} row of $\tilde{\mathbf{F}}(\lambda)$ in column vector form (i.e. transposed to a column vector), and let $\hat{\mathbf{v}}_k(\lambda) = \mathbf{V}_{*,k}(\lambda)$ be the k^{th} column of $\mathbf{V}(\lambda)$. Since $\mathbf{V}(\lambda)$ is a unitary matrix, its columns form a basis. Therefore, one can write $\vec{x}_i(\lambda)$ as a linear combination of the columns of $\mathbf{V}(\lambda)$ of the form

$$\vec{x}_i(\lambda) = \sum_{k=1}^N a_k^{(i)}(\lambda) \hat{\mathbf{v}}_k(\lambda). \quad (\text{B.20})$$

¹¹But are not necessarily

It now follows that

$$\mathbf{H}^\dagger(\lambda)\mathbf{H}(\lambda)\vec{\mathbf{x}}_i(\lambda) = \mathbf{H}^\dagger(\lambda)\mathbf{H}(\lambda) \left(\sum_{k=1}^N a_k^{(i)}(\lambda) \hat{\mathbf{v}}_k(\lambda) \right), \quad (\text{B.21})$$

where, as per Equations B.14 and B.4, $\mathbf{H}^\dagger(\lambda)\mathbf{H}(\lambda) = \tilde{\mathbf{F}}^\dagger(\lambda)\tilde{\mathbf{\Lambda}}^{(f)}(\lambda)\tilde{\mathbf{F}}(\lambda) = \mathbf{V}(\lambda)\mathbf{\Lambda}^{(v)}(\lambda)\mathbf{V}^\dagger(\lambda)$.

Now, from the previous appendix subsection (Appendix Subsection B.3.1), we know that the vectors $\vec{\mathbf{x}}_i(\lambda) = (\tilde{\mathbf{F}}_{i,*}^*(\lambda))^\top$ and $\hat{\mathbf{v}}_k(\lambda) = \mathbf{V}_{*,k}(\lambda)$ are eigenvectors of $\mathbf{H}^\dagger(\lambda)\mathbf{H}(\lambda)$ with corresponding eigenvalues $\lambda_i^{(fv)}(\lambda)$ and $\lambda_k^{(fv)}(\lambda)$ respectively. With this in mind, and recalling Equation B.20 from earlier, Equation B.21 can be manipulated as follows:

$$\begin{aligned} \lambda_i^{(fv)}(\lambda)\vec{\mathbf{x}}_i(\lambda) &= \sum_{k=1}^N \lambda_k^{(fv)}(\lambda) a_k^{(i)}(\lambda) \hat{\mathbf{v}}_k(\lambda) \\ \lambda_i^{(fv)}(\lambda) \sum_{k=1}^N a_k^{(i)}(\lambda) \hat{\mathbf{v}}_k(\lambda) &= \sum_{k=1}^N \lambda_k^{(fv)}(\lambda) a_k^{(i)}(\lambda) \hat{\mathbf{v}}_k(\lambda) \\ \sum_{k=1}^N [\lambda_i^{(fv)}(\lambda) - \lambda_k^{(fv)}(\lambda)] a_k^{(i)}(\lambda) \hat{\mathbf{v}}_k(\lambda) &= 0. \end{aligned}$$

Since $\{\hat{\mathbf{v}}_k(\lambda)\}_{k=0}^N$ form a set of orthonormal vectors¹², they are linearly independent. Therefore, from the last equation above, $[\lambda_i^{(fv)}(\lambda) - \lambda_k^{(fv)}(\lambda)] a_k^{(i)}(\lambda)$ must equal 0 for all k because of linear independence. This implies that for any k such that $\lambda_i(\lambda) \neq \lambda_k(\lambda)$, $a_k^{(i)}(\lambda) = 0$. Using this fact, the equation $\vec{\mathbf{x}}_i(\lambda) = (\tilde{\mathbf{F}}_{i,*}^*(\lambda))^\top$, and Equation B.20, one can write

$$\vec{\mathbf{x}}_i(\lambda) = (\tilde{\mathbf{F}}_{i,*}^*(\lambda))^\top = \sum_{\ell \in \{k \in \mathbb{Z} | (1 \leq k \leq N) \wedge [\lambda_i(\lambda) = \lambda_k(\lambda)]\}} a_\ell^{(i)}(\lambda) \hat{\mathbf{v}}_\ell(\lambda) \quad (\text{B.22})$$

Now, we will restrict our analysis to i associated with non-degenerate eigenvalues. For non-repeated eigenvalues, only one summand is non-zero in the summation shown in Equation B.22, namely the $\ell = i$ term. Also note that by definition, $|\vec{\mathbf{x}}_i(\lambda)| = 1$ and $|\hat{\mathbf{v}}_i(\lambda)| = 1$, which implies that $|a_i^{(i)}(\lambda)| = 1$ when only one term is in the summation. When $|a_i^{(i)}(\lambda)| = 1$,

¹²This is because the vectors $\{\hat{\mathbf{v}}_k(\lambda)\}_{k=0}^N$ are the columns of the unitary matrix $\mathbf{V}(\lambda)$.

$a_i^{(i)}(\lambda)$ can be written in the form $e^{j\alpha_i(\lambda)}$ —where $\alpha_i(\lambda)$ is an arbitrary real number—since all complex numbers with magnitude 1 can be written in that form. Therefore, taking Equation B.22 and considering the reasons listed in this paragraph, for i corresponding to non-degenerate eigenvalues, one can write

$$\begin{aligned} \left(\tilde{\mathbf{F}}_{i,*}^*(\lambda) \right)^\top &= e^{j\alpha_i(\lambda)} \hat{\mathbf{v}}_i(\lambda) \\ \hat{\mathbf{v}}_i(\lambda) &= e^{-j\alpha_i(\lambda)} \left(\tilde{\mathbf{F}}_{i,*}^*(\lambda) \right)^\top. \end{aligned}$$

Letting $\phi_i(\lambda)$ be another arbitrary real number that equals $-\alpha_i(\lambda)$, and then substituting $\phi_i(\lambda) = -\alpha_i(\lambda)$ and $\hat{\mathbf{v}}_i(\lambda) = \mathbf{V}_{*,i}(\lambda)$ into the last equation above, one then gets

$$\mathbf{V}_{*,i}(\lambda) = e^{j\phi_i(\lambda)} \left(\tilde{\mathbf{F}}_{i,*}^*(\lambda) \right)^\top. \quad (\text{B.23})$$

Additionally, note that by definition, $\hat{\mathbf{F}}_{i,*}(\lambda) = \mathbf{F}_{i,*}(\lambda)/\Delta_{i,i}^{(f)}(\lambda)$, and that the first D rows of $\tilde{\mathbf{F}}_{i,*}(\lambda)$ equal the first D rows of $\hat{\mathbf{F}}_{i,*}(\lambda)$ —this follows via construction (see Appendix Subsection B.2.2). Consequently, $\tilde{\mathbf{F}}_{i,*}(\lambda) = \hat{\mathbf{F}}_{i,*}(\lambda) = \mathbf{F}_{i,*}(\lambda)/\Delta_{i,i}^{(f)}(\lambda)$ for $1 \leq i \in \mathbb{Z} \leq D$ —the restriction of $1 \leq i \in \mathbb{Z} \leq D$ comes from the fact that $\mathbf{F}(\lambda)$ only has D rows, so $\hat{\mathbf{F}}_{i,*}(\lambda) = \mathbf{F}_{i,*}(\lambda)/\Delta_{i,i}^{(f)}(\lambda)$ would be undefined for $i > D$. Now, substituting $\tilde{\mathbf{F}}_{i,*}(\lambda) = \hat{\mathbf{F}}_{i,*}(\lambda) = \mathbf{F}_{i,*}(\lambda)/\Delta_{i,i}^{(f)}(\lambda)$ into Equation B.23 for $1 \leq i \in \mathbb{Z} \leq D$ and applying Equation B.10, one gets the expression

$$\mathbf{V}_{*,i}(\lambda) = \left[\frac{[\mathbf{F}_{i,*}^*(\lambda)]^\top}{\sqrt{\sum_{\ell=1}^N |F_{i,\ell}(\lambda)|^2}} \right] e^{j\phi_i(\lambda)}, \quad \text{for } 1 \leq i \in \mathbb{Z} \leq D, \quad (\text{B.24})$$

where $\phi_i(\lambda)$ is some real-valued number. Note that the equation above, Equation B.24, also does not apply for i corresponding to degenerate (i.e. repeated) eigenvalues of $\mathbf{H}^\dagger(\lambda)\mathbf{H}(\lambda)$.

B.4.2 Deriving an expression for the left-singular vectors

Let $\vec{x}_i(\lambda) = \tilde{\mathbf{B}}_{*,i}(\lambda)$ be the i^{th} column of $\tilde{\mathbf{B}}(\lambda)$, and let $\hat{\mathbf{u}}_k(\lambda) = \mathbf{U}_{*,k}(\lambda)$ be the k^{th} column of $\mathbf{U}(\lambda)$. Since $\mathbf{U}(\lambda)$ is a unitary matrix, its columns form a basis. Therefore, one can write $\vec{x}_i(\lambda)$ as a linear combination of the columns of $\mathbf{U}(\lambda)$ of the form $\vec{x}_i(\lambda) = \sum_{k=1}^N b_k^{(i)}(\lambda) \hat{\mathbf{u}}_k(\lambda)$. Additionally, from the previous appendix subsection (Appendix Subsection B.3.1), the vectors $\vec{x}_i(\lambda) = \tilde{\mathbf{B}}_{*,i}^*(\lambda)$ and $\hat{\mathbf{u}}_k(\lambda) = \mathbf{U}_{*,k}(\lambda)$ are eigenvectors of $\mathbf{H}(\lambda)\mathbf{H}^\dagger(\lambda)$ with corresponding eigenvalues $\lambda_i^{(bu)}(\lambda)$ and $\lambda_k^{(bu)}(\lambda)$ respectively.

It now follows that

$$\begin{aligned}\mathbf{H}(\lambda)\mathbf{H}^\dagger(\lambda)\vec{x}_i(\lambda) &= \mathbf{H}(\lambda)\mathbf{H}^\dagger(\lambda) \left(\sum_{k=1}^N b_k^{(i)}(\lambda) \hat{\mathbf{u}}_k(\lambda) \right) \\ \lambda_i^{(bu)}(\lambda)\vec{x}_i(\lambda) &= \sum_{k=1}^N \lambda_k^{(bu)}(\lambda) b_k^{(i)}(\lambda) \hat{\mathbf{u}}_k(\lambda) \\ \lambda_i^{(bu)}(\lambda) \sum_{k=1}^N b_k^{(i)}(\lambda) \hat{\mathbf{u}}_k(\lambda) &= \sum_{k=1}^N \lambda_k^{(bu)}(\lambda) b_k^{(i)}(\lambda) \hat{\mathbf{u}}_k(\lambda) \\ \sum_{k=1}^N \left[\lambda_i^{(bu)}(\lambda) - \lambda_k^{(bu)}(\lambda) \right] b_k^{(i)}(\lambda) \hat{\mathbf{u}}_k(\lambda) &= 0,\end{aligned}$$

where, as per Equations B.15 and B.5, $\mathbf{H}(\lambda)\mathbf{H}^\dagger(\lambda) = \tilde{\mathbf{B}}(\lambda)\tilde{\Lambda}^{(b)}(\lambda)\tilde{\mathbf{B}}^\dagger(\lambda) = \mathbf{U}(\lambda)\Lambda^{(u)}(\lambda)\mathbf{U}^\dagger(\lambda)$.

Following the similar steps to those taken in Appendix Subsection B.4.1—starting with the linear independence argument in that appendix subsection and proceeding up to the point where one reaches Equation B.23—one obtains

$$\mathbf{U}_{*,k}(\lambda) = e^{j\theta_i(\lambda)} \tilde{\mathbf{B}}_{*,i}(\lambda) \quad (\text{B.25})$$

Now, making the substitution $\tilde{\mathbf{B}}_{*,i}(\lambda) = \hat{\mathbf{B}}_{*,i}(\lambda) = \mathbf{B}_{*,i}(\lambda)/\Delta_{i,i}^{(b)}(\lambda)$ for $1 \leq i \in \mathbb{Z} \leq D$, one obtains

$$\mathbf{U}_{*,i}(\lambda) = \left[\frac{\mathbf{B}_{*,i}(\lambda)}{\sqrt{\sum_{\ell=1}^M |B_{\ell,i}(\lambda)|^2}} \right] e^{j\theta_i(\lambda)}, \text{ for } 1 \leq i \in \mathbb{Z} \leq D, \quad (\text{B.26})$$

where $\theta_i(\lambda)$ is some real-valued number. Note that i is being limited in this manner since $\mathbf{B}(\lambda)$ only has D columns, so $\hat{\mathbf{B}}_{*,i}(\lambda) = \mathbf{B}_{*,i}(\lambda)/\Delta_{i,i}^{(b)}(\lambda)$ would be undefined for $i > D$ —similar reasoning is also used in Appendix Subsection B.4.1. And, similarly to (but not exactly the same as) Equation B.24, Equation B.26 does not apply for i corresponding to degenerate (i.e. repeated) eigenvalues of $\mathbf{H}(\lambda)\mathbf{H}^\dagger(\lambda)$.

B.4.3 Equation validity in terms of singular values

Recall that Equations B.24 and B.26 do not apply for i corresponding to degenerate (i.e. repeated) eigenvalues of $\mathbf{H}^\dagger(\lambda)\mathbf{H}(\lambda)$ and $\mathbf{H}(\lambda)\mathbf{H}^\dagger(\lambda)$ respectively. Now, note that the eigenvalues of $\mathbf{H}^\dagger(\lambda)\mathbf{H}(\lambda)$ are given by Equation B.18, and that the first $\min(M, N)$ eigenvalues (i.e. $\lambda_i^{(fv)}$ where $1 \leq i \in \mathbb{Z} \leq \min(M, N)$) are equal to the squares of the singular values. Similarly, the eigenvalues of $\mathbf{H}(\lambda)\mathbf{H}^\dagger(\lambda)$ are given by Equation B.19, and that the first $\min(M, N)$ eigenvalues (i.e. $\lambda_i^{(bu)}$ where $1 \leq i \in \mathbb{Z} \leq \min(M, N)$) are equal to the squares of the singular values. Thus, Equations B.24 and B.26 do not apply for i such that the corresponding singular value $\Sigma_{i,i}(\lambda)$ is repeated.

Note that $\mathbf{H}^\dagger(\lambda)\mathbf{H}(\lambda)$ and $\mathbf{H}(\lambda)\mathbf{H}^\dagger(\lambda)$ have N and M eigenvalues respectively, and that there are $\min(M, N)$ singular values. Thus, $\mathbf{H}^\dagger(\lambda)\mathbf{H}(\lambda)$ and $\mathbf{H}(\lambda)\mathbf{H}^\dagger(\lambda)$ will have $N - \min(M, N)$ and $M - \min(M, N)$ eigenvalues that do not correspond to a singular value—these eigenvalues are equal to 0 as per Equations B.18 and B.19.

Therefore, if one has a lone non-repeated zero-valued singular value, one can potentially run into a situation where either Equation B.24 or B.26 is invalid for i corresponding to that singular value—the additional 0 eigenvalues that do not correspond to a singular value can cause a situation where one has a repeated eigenvalue if one has a singular value of 0 (which implies an eigenvalue of 0). For Equation B.24, this situation can happen when $\min(M, N) < N$, and for Equation B.26, this situation can happen when $\min(M, N) < M$.

B.5 Deriving an expression for the singular values

To derive an expression for $\Sigma(\lambda)$, first note that the i^{th} singular vectors $\mathbf{U}_{*,i}(\lambda)$ and $\mathbf{V}_{*,i}(\lambda)$ of $\mathbf{H}(\lambda)$ are related by the following expression:¹³

$$\sigma_i(\lambda) \mathbf{U}_{*,i}(\lambda) = \mathbf{H}(\lambda) \mathbf{V}_{*,i}(\lambda).$$

Substituting $\mathbf{H}(\lambda) = \mathbf{B}(\lambda)\mathbf{S}(\lambda)\mathbf{F}(\lambda)$ into the expression above and then substituting in Equation B.24 gives

$$\begin{aligned} \sigma_i(\lambda) \mathbf{U}_{*,i}(\lambda) &= \mathbf{B}(\lambda)\mathbf{S}(\lambda)\mathbf{F}(\lambda)\mathbf{V}_{*,i}(\lambda) \\ &= \mathbf{B}(\lambda)\mathbf{S}(\lambda)\mathbf{F}(\lambda) \left[\frac{[\mathbf{F}_{i,*}^*(\lambda)]^\top}{\sqrt{\sum_{\ell=1}^N |F_{i,\ell}(\lambda)|^2}} \right] e^{j\phi_i(\lambda)} \\ &= e^{j\phi_i(\lambda)} \frac{\mathbf{B}(\lambda)\mathbf{S}(\lambda)}{\sqrt{\sum_{\ell=1}^N |F_{i,\ell}(\lambda)|^2}} \begin{bmatrix} \sum_{\ell=1}^N F_{1,\ell}(\lambda) F_{i,\ell}^*(\lambda) \\ \sum_{\ell=1}^N F_{2,\ell}(\lambda) F_{i,\ell}^*(\lambda) \\ \vdots \\ \sum_{\ell=1}^N F_{D,\ell}(\lambda) F_{i,\ell}^*(\lambda) \end{bmatrix}. \end{aligned}$$

Note that the $\sum_{\ell=1}^N F_{1,\ell}(\lambda) F_{i,\ell}^*(\lambda)$, $\sum_{\ell=1}^N F_{2,\ell}(\lambda) F_{i,\ell}^*(\lambda)$, \dots , $\sum_{\ell=1}^N F_{D,\ell}(\lambda) F_{i,\ell}^*(\lambda)$ terms are just complex inner products¹⁴. Now, because it was assumed that the scatterers were ideally-resolved, the rows of $\mathbf{F}(\lambda)$ are mutually orthogonal. This means that only $\sum_{\ell=1}^N F_{i,\ell}(\lambda) F_{i,\ell}^*(\lambda)$

¹³In general, if $\vec{\mathbf{u}}$ and $\vec{\mathbf{v}}$ are singular vectors of a matrix \mathbf{M} , and σ is the singular value associated with those singular vectors, then the expression $\sigma\vec{\mathbf{u}} = \mathbf{M}\vec{\mathbf{v}}$ holds.

¹⁴Assuming that one is using the convention of complex inner products having conjugate linearity on their second argument.

is non-zero. Thus, one can write

$$\begin{aligned}
\sigma_i(\lambda) \mathbf{U}_{*,i}(\lambda) &= e^{j\phi_i(\lambda)} \frac{\mathbf{B}(\lambda) \mathbf{S}(\lambda)}{\sqrt{\sum_{\ell=1}^N |F_{i,\ell}(\lambda)|^2}} \left(\sum_{\ell=1}^N F_{i,\ell}(\lambda) F_{i,\ell}^*(\lambda) \right) \hat{\mathbf{e}}_i \\
&= e^{j\phi_i(\lambda)} \frac{\mathbf{B}(\lambda) \mathbf{S}(\lambda)}{\sqrt{\sum_{\ell=1}^N |F_{i,\ell}(\lambda)|^2}} \left(\sum_{\ell=1}^N |F_{i,\ell}(\lambda)|^2 \right) \hat{\mathbf{e}}_i \\
&= e^{j\phi_i(\lambda)} \frac{\mathbf{B}(\lambda) \mathbf{S}(\lambda)}{\sqrt{\sum_{\ell=1}^N |F_{i,\ell}(\lambda)|^2}} \left(\sqrt{\sum_{\ell=1}^N |F_{i,\ell}(\lambda)|^2} \right)^2 \hat{\mathbf{e}}_i \\
&= e^{j\phi_i(\lambda)} \left(\sqrt{\sum_{\ell=1}^N |F_{i,\ell}(\lambda)|^2} \right) \mathbf{B}(\lambda) \mathbf{S}(\lambda) \hat{\mathbf{e}}_i,
\end{aligned}$$

where $\hat{\mathbf{e}}_i$ is the i^{th} standard basis vector. Next, since $\mathbf{S}(\lambda)$ is a diagonal matrix, one can write

$$\sigma_i(\lambda) \mathbf{U}_{*,i}(\lambda) = e^{j\phi_i(\lambda)} S_{i,i}(\lambda) \left(\sqrt{\sum_{\ell=1}^N |F_{i,\ell}(\lambda)|^2} \right) \mathbf{B}(\lambda) \hat{\mathbf{e}}_i.$$

This can be further simplified to

$$\sigma_i(\lambda) \mathbf{U}_{*,i}(\lambda) = e^{j\phi_i(\lambda)} S_{i,i}(\lambda) \left(\sqrt{\sum_{\ell=1}^N |F_{i,\ell}(\lambda)|^2} \right) \mathbf{B}_{*,i}(\lambda)$$

Substituting in Equation B.26 gives

$$\sigma_i(\lambda) \left[\frac{\mathbf{B}_{*,i}(\lambda)}{\sqrt{\sum_{\ell=1}^M |B_{\ell,i}(\lambda)|^2}} \right] e^{j\theta_i(\lambda)} = e^{j\phi_i(\lambda)} S_{i,i}(\lambda) \left(\sqrt{\sum_{\ell=1}^N |F_{i,\ell}(\lambda)|^2} \right) \mathbf{B}_{*,i}(\lambda). \quad (\text{B.27})$$

Keep in mind that the equation above (Equation B.27) relies on Equations B.24 and B.26, which are only valid for $1 \leq i \in \mathbb{Z} \leq D$. Thus, Equation B.27 is only valid for $1 \leq i \in \mathbb{Z} \leq D$.

B.5.1 Case 1

Assuming that $S_{i,i}(\lambda) = 0$ in Equation B.27, one gets

$$\sigma_i(\lambda) \left[\frac{\mathbf{B}_{*,i}(\lambda)}{\sqrt{\sum_{\ell=1}^M |B_{\ell,i}(\lambda)|^2}} \right] e^{j[\theta_i(\lambda) - \phi_i(\lambda)]} = 0. \quad (\text{B.28})$$

Equation B.28 was obtained by first dividing both sides of Equation B.27 by $e^{j\phi_i(\lambda)}$ and then substituting in $S_{i,i}(\lambda) = 0$.

Now, because ideally-resolved scatterers were assumed, $\mathbf{B}_{*,i}(\lambda)$ has at least one non-zero component. This means that one does not get a division by zero from the $\sqrt{\sum_{\ell=1}^M |B_{\ell,i}(\lambda)|^2}$ term in Equation B.28 as $\sqrt{\sum_{\ell=1}^M |B_{\ell,i}(\lambda)|^2} \neq 0$. Additionally, since Equation B.28 is a vector equation, the following scalar equations are implied:

$$\sigma_i(\lambda) \left[\frac{B_{k,i}(\lambda)}{\sqrt{\sum_{\ell=1}^M |B_{\ell,i}(\lambda)|^2}} \right] e^{j[\theta_i(\lambda) - \phi_i(\lambda)]} = 0, \text{ for } k \in \mathbb{Z} \text{ such that } 1 \leq k \leq M. \quad (\text{B.29})$$

These equations simplify to

$$\sigma_i(\lambda) B_{k,i} = 0, \text{ for } k \in \mathbb{Z} \text{ such that } 1 \leq k \leq M.$$

For $B_{k,i}(\lambda) = 0$, no useful constraints are given. However, when $B_{k,i}(\lambda) \neq 0$, dividing both sides by $B_{k,i}(\lambda)$ gives $\sigma_i(\lambda) = 0$. Because ideally-resolved scatterers were assumed, $\mathbf{B}_{*,i}(\lambda)$ has at least one non-zero component, meaning that one gets the constraint $\sigma_i(\lambda) = 0$ from at least one equation. Therefore, if $S_{i,i}(\lambda) = 0$, then $\sigma_i(\lambda) = 0$.

B.5.2 Case 2

Assuming that $S_{i,i}(\lambda) \neq 0$ in Equation B.27, one gets

$$\sigma_i(\lambda) e^{j\theta_i(\lambda)} e^{-j\phi_i(\lambda)} \mathbf{B}_{*,i}(\lambda) = |S_{i,i}(\lambda)| e^{j \operatorname{Arg}(S_{i,i}(\lambda))} \left(\sqrt{\sum_{\ell=1}^N |F_{i,\ell}(\lambda)|^2} \right) \left(\sqrt{\sum_{\ell=1}^M |B_{\ell,i}(\lambda)|^2} \right) \mathbf{B}_{*,i}(\lambda) \quad (\text{B.30})$$

where $\operatorname{Arg}(\dots)$ denotes the principal value of the argument. Note that $\operatorname{Arg}(0)$ is potentially undefined, depending on how one defines the Arg function—in our case, we will leave $\operatorname{Arg}(0)$ undefined. In order to avoid an undefined value for $\operatorname{Arg}(0)$, the case of $S_{i,i}(\lambda) = 0$ was handled separately earlier in this derivation.

Equation B.30 can now be expressed as

$$\sigma_i(\lambda) e^{[j([\theta_i(\lambda) - \phi_i(\lambda)] - \operatorname{Arg}(S_{i,i}(\lambda)))]} \mathbf{B}_{*,i}(\lambda) = |S_{i,i}(\lambda)| \left(\sqrt{\sum_{\ell=1}^N |F_{i,\ell}(\lambda)|^2} \right) \left(\sqrt{\sum_{\ell=1}^M |B_{\ell,i}(\lambda)|^2} \right) \mathbf{B}_{*,i}(\lambda). \quad (\text{B.31})$$

Since the equation above is a vector equation, a set of scalar equations is implied. Thus, using the equation above (Equation B.31), one can write the following:

$$\sigma_i(\lambda) e^{[j([\theta_i(\lambda) - \phi_i(\lambda)] - \operatorname{Arg}(S_{i,i}(\lambda)))]} B_{k,i}(\lambda) = |S_{i,i}(\lambda)| \left(\sqrt{\sum_{\ell=1}^N |F_{i,\ell}(\lambda)|^2} \right) \left(\sqrt{\sum_{\ell=1}^M |B_{\ell,i}(\lambda)|^2} \right) B_{k,i}(\lambda),$$

for $k \in \mathbb{Z}$ such that $1 \leq k \leq M$.

$$(\text{B.32})$$

For k such that $B_{k,i}(\lambda)$ is defined¹⁵ and $B_{k,i}(\lambda) = 0$, the equation above does not offer any useful constraints. For any and all k such that $B_{k,i}(\lambda)$ is defined and $B_{k,i}(\lambda) \neq 0$, dividing

¹⁵Note that Equation B.32 is only defined for $k \in \mathbb{Z}$ such that $1 \leq k \leq M$.

both sides of Equation B.32 by $B_{k,i}(\lambda)$ will give the same constraint, namely

$$\sigma_i(\lambda) e^{j(\theta_i(\lambda) - \phi_i(\lambda) - \text{Arg}(S_{i,i}(\lambda)))} = |S_{i,i}(\lambda)| \left(\sqrt{\sum_{\ell=1}^N |F_{i,\ell}(\lambda)|^2} \right) \left(\sqrt{\sum_{\ell=1}^M |B_{\ell,i}(\lambda)|^2} \right). \quad (\text{B.33})$$

Because ideally-resolved scatterers were assumed, $\mathbf{B}_{*,i}(\lambda)$ has at least one non-zero component, thus at least one of the scalar equations specified in Equation B.32 gives the constraint shown above in Equation B.33.

Taking the magnitude of both sides of Equation B.33 gives

$$|\sigma_i(\lambda)| = |S_{i,i}(\lambda)| \left(\sqrt{\sum_{\ell=1}^N |F_{i,\ell}(\lambda)|^2} \right) \left(\sqrt{\sum_{\ell=1}^M |B_{\ell,i}(\lambda)|^2} \right).$$

which, since singular values are always non-negative real numbers, gives

$$\sigma_i(\lambda) = |S_{i,i}(\lambda)| \left(\sqrt{\sum_{\ell=1}^N |F_{i,\ell}(\lambda)|^2} \right) \left(\sqrt{\sum_{\ell=1}^M |B_{\ell,i}(\lambda)|^2} \right). \quad (\text{B.34})$$

B.5.3 Combining cases

Note that Equation B.34 was derived from Equation B.30, which presupposes that $S_{i,i}(\lambda) \neq 0$. However, it was also shown in Appendix Subsection B.5.1 that the complementary case, $S_{i,i}(\lambda) = 0$, has $\sigma_i(\lambda) = 0$ —Equation B.34 works for this case as well as plugging in $S_{i,i}(\lambda) = 0$ into Equation B.34 gives $\sigma_i(\lambda) = 0$. Therefore, Equation B.34 works for both $S_{i,i}(\lambda) \neq 0$ and $S_{i,i}(\lambda) = 0$, thus one does not have to differentiate between the $S_{i,i}(\lambda) \neq 0$ and $S_{i,i}(\lambda) = 0$ cases in Equation B.34.

It should be noted that although Equation B.34 is in terms of $\sigma_i(\lambda)$, it also defined some of the elements of $\Sigma(\lambda)$. This is because $\Sigma(\lambda)$ matrix is a diagonal matrix of singular values (i.e. the terms $\sigma_i(\lambda)$) and $\Sigma_{i,i}(\lambda) = \sigma_i(\lambda)$. One can therefore make the substitution $\sigma_i(\lambda) = \Sigma_{i,i}(\lambda)$.

Now, because Equation B.34 was derived from Equations B.24 and B.26, which are only valid for $1 \leq i \in \mathbb{Z} \leq D$, Equation B.34 is only valid for $1 \leq i \in \mathbb{Z} \leq D$. However, for singular values numbered higher than D , one can use Equation B.18 (or equivalently, Equation B.19). It can be seen that singular values numbered higher than D equal zero.

Keeping the previous paragraphs in this appendix subsection (Appendix Subsection B.5.3) in mind, one gets the following expression for $\Sigma(\lambda)$:

$$\Sigma_{i,j}(\lambda) = \begin{cases} |S_{i,i}(\lambda)| \left(\sqrt{\sum_{\ell=1}^N |F_{i,\ell}(\lambda)|^2} \right) \left(\sqrt{\sum_{\ell=1}^M |B_{\ell,i}(\lambda)|^2} \right), & \text{for } (i = j) \wedge (i \leq D) \\ 0, & \text{for } (i \neq j) \vee (i > D). \end{cases} \quad (\text{B.35})$$

B.6 Obtaining constraints on singular vector phase terms

One can also come up with a constraints for the phase terms $\theta_i(\lambda)$ and $\phi_i(\lambda)$ in Equations B.24 and B.26. Such will be done here, in Appendix Section B.6.

First, consider the case where $S_{i,i}(\lambda) = 0$. By Equation B.34, which applies for the cases $S_{i,i}(\lambda) = 0$ and $S_{i,i}(\lambda) \neq 0$, it follows that $\sigma_i(\lambda) = 0$. Equation B.29 then simplifies to $0 = 0$, which does not add any constraints on $\theta_i(\lambda)$ and $\phi_i(\lambda)$ —any arbitrary value of $\theta_i(\lambda)$ and $\phi_i(\lambda)$ will work in this case. Thus, since Equation B.29 follows from Equation B.27 when $S_{i,i}(\lambda) = 0$, whenever Equation B.27 holds and $S_{i,i}(\lambda) = 0$, there are no constraints on the values of $\theta_i(\lambda)$ and $\phi_i(\lambda)$ other than the fact that they are real numbers.

Now consider the case where $S_{i,i}(\lambda) \neq 0$. Substituting Equation B.34 into Equation B.33

gives:

$$\begin{aligned}
 |S_{i,i}(\lambda)| & \left(\sqrt{\sum_{\ell=1}^N |F_{i,\ell}(\lambda)|^2} \right) \left(\sqrt{\sum_{\ell=1}^M |B_{\ell,i}(\lambda)|^2} \right) e^{[j([\theta_i(\lambda) - \phi_i(\lambda)] - \text{Arg}(S_{i,i}(\lambda)))]} \\
 & = |S_{i,i}(\lambda)| \left(\sqrt{\sum_{\ell=1}^N |F_{i,\ell}(\lambda)|^2} \right) \left(\sqrt{\sum_{\ell=1}^M |B_{\ell,i}(\lambda)|^2} \right).
 \end{aligned} \tag{B.36}$$

Note that by assumption, $S_{i,i}(\lambda) \neq 0$. This assumption is necessary because Equation B.33 is only valid for $S_{i,i}(\lambda) \neq 0$.¹⁶ Now, since $S_{i,i}(\lambda) \neq 0$, it follows that the absolute value $|S_{i,i}(\lambda)|$ is > 0 . Additionally, the ideally-resolved assumption means that $\vec{\mathbf{F}}_{i,*}(\lambda)$ and $\vec{\mathbf{B}}_{*,i}(\lambda)$ are not zero vectors, which implies that the $\sqrt{\sum_{\ell=1}^N |F_{i,\ell}(\lambda)|^2}$ and $\sqrt{\sum_{\ell=1}^M |B_{\ell,i}(\lambda)|^2}$ terms are (non-zero) positive real numbers.¹⁷ Since $|S_{i,i}(\lambda)|$, $\sqrt{\sum_{\ell=1}^N |F_{i,\ell}(\lambda)|^2}$, and $\sqrt{\sum_{\ell=1}^M |B_{\ell,i}(\lambda)|^2}$ are all positive real numbers, and the product of positive real numbers is a positive real number, the right-hand side of Equation B.36 is a (non-zero) positive real number.

Since the right-hand side of Equation B.36 is a (non-zero) positive real number, one can divide both sides of Equation B.36 by the right-hand side to get

$$e^{[j([\theta_i(\lambda) - \phi_i(\lambda)] - \text{Arg}(S_{i,i}(\lambda)))]} = 1. \tag{B.37}$$

Equation B.37 can only hold if $[\theta_i(\lambda) - \phi_i(\lambda)] - \text{Arg}(S_{i,i}(\lambda))$ is a multiple of 2π . Using this fact and doing some rearranging, it can be seen that the following must hold:

$$\theta_i(\lambda) - \phi_i(\lambda) = \text{Arg}(S_{i,i}(\lambda)) + 2\pi m_i(\lambda), \text{ for } 1 \leq i \leq D \text{ such that } S_{i,i}(\lambda) \neq 0, \tag{B.38}$$

and where $m_i(\lambda)$ is some integer.

¹⁶Equation B.33 is only valid for $S_{i,i}(\lambda) \neq 0$ because $S_{i,i}(\lambda) = 0$ gives an $\text{Arg}(0)$ term in Equation B.33, and $\text{Arg}(0)$ was stated to be undefined earlier.

¹⁷ $\sqrt{\sum_{\ell=1}^N |F_{i,\ell}(\lambda)|^2}$ and $\sqrt{\sum_{\ell=1}^M |B_{\ell,i}(\lambda)|^2}$ are the magnitudes of the vectors $\vec{\mathbf{F}}_{i,*}(\lambda)$ and $\vec{\mathbf{B}}_{*,i}(\lambda)$ respectively. Since those vectors are finite-dimensional vectors of complex numbers, and those vectors are non-zero by the ideally-resolved assumption, their magnitudes $\sqrt{\sum_{\ell=1}^N |F_{i,\ell}(\lambda)|^2}$ and $\sqrt{\sum_{\ell=1}^M |B_{\ell,i}(\lambda)|^2}$ must be positive real numbers.

Note that the equation above, Equation B.38 does not hold for $S_{i,i}(\lambda) = 0$. Moreover, as stated before, when $S_{i,i}(\lambda) = 0$, $\theta_i(\lambda)$ and $\phi_i(\lambda)$ can take on arbitrary real values. It should also be noted that because Equation B.38 was derived from Equations B.24 and B.26, which are only valid for $1 \leq i \in \mathbb{Z} \leq D$, Equation B.38 is only valid for $1 \leq i \in \mathbb{Z} \leq D$.

B.7 Summary of results

In this appendix (Appendix B), a number of equations were derived. The main results were Equations B.24, B.26, B.35, and B.38. These equations describe the result of taking the singular value decomposition of an $M \times N$ transfer matrix $\mathbf{H}(\lambda)$. These equations are reprinted below for convenience:

$$\mathbf{V}_{*,i}(\lambda) = \left[\frac{[\mathbf{F}_{i,*}^*(\lambda)]^\top}{\sqrt{\sum_{\ell=1}^N |F_{i,\ell}(\lambda)|^2}} \right] e^{j\phi_i(\lambda)}, \text{ for } 1 \leq i \in \mathbb{Z} \leq D \quad (\text{B.24})$$

$$\mathbf{U}_{*,i}(\lambda) = \left[\frac{\mathbf{B}_{*,i}(\lambda)}{\sqrt{\sum_{\ell=1}^M |B_{\ell,i}(\lambda)|^2}} \right] e^{j\theta_i(\lambda)}, \text{ for } 1 \leq i \in \mathbb{Z} \leq D \quad (\text{B.26})$$

$$\Sigma_{i,j}(\lambda) = \begin{cases} |S_{i,i}(\lambda)| \left(\sqrt{\sum_{\ell=1}^N |F_{i,\ell}(\lambda)|^2} \right) \left(\sqrt{\sum_{\ell=1}^M |B_{\ell,i}(\lambda)|^2} \right), & \text{for } (i = j) \wedge (i \leq D) \\ 0, & \text{for } (i \neq j) \vee (i > D). \end{cases} \quad (\text{B.35})$$

$$\theta_i(\lambda) - \phi_i(\lambda) = \operatorname{Arg}(S_{i,i}(\lambda)) + 2\pi m_i(\lambda), \text{ for } 1 \leq i \in \mathbb{Z} \leq D \text{ such that } S_{i,i}(\lambda) \neq 0, \quad (\text{B.38})$$

and where $m_i(\lambda)$ is some integer.

These equations are subject to a number of conditions. First off, all of these equations are based on the assumptions listed in Appendix Section B.1. Thus, these equations are not necessarily valid outside of the assumptions listed in Appendix Section B.1. Additionally, the standard ordering convention for singular values in the singular value decomposition is

assumed.¹⁸

Furthermore, Equations B.24 and B.26 do not apply for $i > D$. Those equations also do not apply for i corresponding to repeated singular values $\Sigma_{i,i}(\lambda)$, i.e. singular values that appear more than once.¹⁹ Additionally, if $\min(M, N) < N$, then Equation B.24 does not apply for i corresponding to non-repeated zero-valued singular values $\Sigma_{i,i}(\lambda)$. Similarly, if $\min(M, N) < M$, then Equation B.26 does not apply for i corresponding to non-repeated zero-valued singular values $\Sigma_{i,i}(\lambda)$.

In Equations B.24 and B.26, the terms $\phi_i(\lambda)$ and $\theta_i(\lambda)$ are real-valued and, when Equation B.38 is applicable, are subject to the constraint given in Equation B.38. The $m_i(\lambda)$ term in Equation B.38 is there to add necessary offsets of integer multiples of 2π , which help account for unwrapped phase.

Equations B.35 and B.38 are derived from both Equation B.24 and Equation B.26, and thus are subject to some of the same restrictions. Specifically, Equations B.35 and B.38 do not apply for i corresponding to repeated singular values $\Sigma_{i,i}(\lambda)$. Those equations also do not apply for non-repeated zero-valued singular values $\Sigma_{i,i}(\lambda)$ when $M \neq N$.²⁰ Moreover, Equation B.38 does not apply for $i > D$, although Equation B.35 does apply for $i > D$.

Finally, as a reminder, the matrices $\mathbf{B}(\lambda)$, $\mathbf{S}(\lambda)$, and $\mathbf{F}(\lambda)$ are $M \times D$, $D \times D$, and $D \times N$ matrices respectively; and $\mathbf{U}(\lambda)$, $\boldsymbol{\Sigma}(\lambda)$, and $\mathbf{V}(\lambda)$ are $M \times M$, $M \times N$, and $N \times N$ matrices respectively. These dimensions give additional constraints on the values that certain subscripts (e.g. i , j , et cetera) can take.

¹⁸In other words, the singular values from the singular value decomposition are ordered as $\sigma_1(\lambda) \geq \sigma_2(\lambda) \geq \dots$, and consequently $\Sigma_{1,1}(\lambda) \geq \Sigma_{2,2}(\lambda) \geq \dots$.

¹⁹For example, if $i \neq k$ and $\Sigma_{i,i}(\lambda) = \Sigma_{k,k}(\lambda)$, then $\Sigma_{i,i}(\lambda)$ and $\Sigma_{k,k}(\lambda)$ are repeated singular values.

²⁰This follows because Equations B.35 and B.38 are subject to the constraints of Equations B.24 and B.26, and the exclusions of single non-repeated zero-value singular values for Equations B.24 and B.26, when combined, become an exclusion of non-repeated zero-valued singular values when $M \neq N$.

Appendix C

Theorems and Proofs

Theorem 1. A matrix \mathbf{M} that can be unitarily diagonalized as $\mathbf{M} = \mathbf{A}^\dagger \mathbf{B} \mathbf{A}$ —where $\mathbf{A}, \mathbf{B} \in \mathbb{C}^{N \times N}$, \mathbf{A} is a unitary matrix, and \mathbf{B} is a diagonal matrix—has eigenvectors $\hat{\mathbf{v}}_i = (\mathbf{A}_{i,*})^\top = \mathbf{A}_{i,*}^\dagger$ associated with eigenvalues $B_{i,i}$.

Proof. Suppose one had a matrix \mathbf{M} that was unitarily diagonalized as $\mathbf{M} = \mathbf{A}^\dagger \mathbf{B} \mathbf{A}$, where \mathbf{A} is an $N \times N$ unitary matrix and \mathbf{B} is an $N \times N$ diagonal matrix. Let $\hat{\mathbf{a}}_i = (\mathbf{A}_{i,*})^\top = \mathbf{A}_{i,*}^\dagger$ be a column vector made from the i^{th} row of \mathbf{A} .

Now, using the convention that the complex inner product (complex dot product) is conjugate linear on the second argument, note that $\mathbf{A}\hat{\mathbf{a}}_i^*$ can be written as

$$\mathbf{A}\hat{\mathbf{a}}_i^* = \begin{bmatrix} \langle \hat{\mathbf{a}}_1, \hat{\mathbf{a}}_i \rangle \\ \langle \hat{\mathbf{a}}_2, \hat{\mathbf{a}}_i \rangle \\ \dots \\ \langle \hat{\mathbf{a}}_N, \hat{\mathbf{a}}_i \rangle \end{bmatrix} = \hat{\mathbf{e}}_i$$

where $\hat{\mathbf{e}}_i$ is the i^{th} standard basis vector. To see why this is the case, note that \mathbf{A} is unitary so its rows are orthonormal. Because the rows are orthonormal, due to mutual orthogonality, only the inner product on the i^{th} row is non-zero. Moreover, the inner product on the i^{th} row equals 1 because the rows have unit magnitude.

Going further, one can write $\mathbf{B}\mathbf{A}\hat{\mathbf{a}}_i^* = \mathbf{B}\hat{\mathbf{e}}_i = B_{i,i}\hat{\mathbf{e}}_i$. It then follows that $\mathbf{A}^\dagger\mathbf{B}\mathbf{A}\hat{\mathbf{a}}_i^* = B_{i,i}\mathbf{A}\hat{\mathbf{e}}_i = B_{i,i}\hat{\mathbf{a}}_i^*$. Therefore, one can write

$$\mathbf{M}\hat{\mathbf{a}}_i^* = \mathbf{A}^\dagger\mathbf{B}\mathbf{A}\hat{\mathbf{a}}_i^*,$$

which means that $\hat{\mathbf{a}}_i^* = (\mathbf{A}_{i,*})^\dagger$ is an eigenvector of \mathbf{M} with eigenvalue $B_{i,i}$. \square

Corollary 1.1. *A matrix \mathbf{M} that can be unitarily diagonalized as $\mathbf{M} = \mathbf{C}\mathbf{B}\mathbf{C}^\dagger$ —where $\mathbf{B}, \mathbf{C} \in \mathbb{C}^{N \times N}$, \mathbf{C} is a unitary matrix, and \mathbf{B} is a diagonal matrix—has eigenvectors $\hat{\mathbf{v}}_j = \mathbf{C}_{*,j}$ associated with eigenvalues $B_{j,j}$.*

Proof. Substitute $\mathbf{A} = \mathbf{C}^\dagger$ for \mathbf{A} in Theorem 1. Then, $\mathbf{M} = \mathbf{C}\mathbf{B}\mathbf{C}^\dagger$. Since $\hat{\mathbf{a}}_i^* = (\mathbf{A}_{i,*})^\dagger$ is an eigenvector of \mathbf{M} with eigenvalue $B_{i,i}$, and $\mathbf{A} = \mathbf{C}^\dagger$, then $\mathbf{C}_{*,i}$ is an eigenvector of \mathbf{M} with eigenvalue $B_{i,i}$. \square

Theorem 2. *Suppose one has a matrix $\mathbf{A} \in \mathbb{C}^{M \times L}$, a diagonal matrix $\mathbf{B} \in \mathbb{C}^{L \times P}$, and a matrix $\mathbf{C} \in \mathbb{C}^{P \times N}$. Then, the matrix product \mathbf{ABC} can be expressed component-wise as*

$$(\mathbf{ABC})_{i,j} = \sum_{k=1}^L A_{i,k} B_{k,k} C_{k,j}.$$

Proof. Let \mathbf{A} , \mathbf{B} , and \mathbf{C} be matrices such that $\mathbf{A} \in \mathbb{C}^{M \times L}$, $\mathbf{B} \in \mathbb{C}^{L \times P}$, $\mathbf{C} \in \mathbb{C}^{P \times N}$, and \mathbf{B} is a diagonal matrix.

The matrix product \mathbf{BC} can be expressed as

$$(\mathbf{BC})_{i,j} = \sum_{k=1}^P B_{i,k} C_{k,j}.$$

However, since \mathbf{B} is a diagonal matrix, $B_{i,k} = 0$ for all $i \neq k$. Thus, one can write

$$(\mathbf{BC})_{i,j} = B_{i,i} C_{i,j}.$$

Now, let $\mathbf{W} = \mathbf{BC}$. The matrix product $\mathbf{AW} = \mathbf{ABC}$ can be expressed as

$$\begin{aligned} (\mathbf{AW})_{i,j} &= \sum_{k=1}^L A_{i,k} W_{k,j} \\ &= \sum_{k=1}^L A_{i,k} (\mathbf{BC})_{k,j} \end{aligned}$$

Since $\mathbf{W} = \mathbf{BC}$ and $(\mathbf{BC})_{i,j} = B_{i,i} C_{i,j}$ were established earlier, it follows that

$$(\mathbf{ABC})_{i,j} = \sum_{k=1}^L A_{i,k} B_{k,k} C_{k,j}.$$

□

Theorem 3. Suppose one has a matrix $\mathbf{A} \in \mathbb{C}^{D \times N}$ and a diagonal matrix $\mathbf{B} \in \mathbb{C}^{D \times D}$. Then, the matrix product $\mathbf{A}^\dagger \mathbf{BA}$ can be expressed component-wise as

$$(\mathbf{A}^\dagger \mathbf{BA})_{i,j} = \sum_{k=1}^D A_{k,i}^* B_{k,k} A_{k,j}.$$

Proof. Suppose \mathbf{A} and \mathbf{B} are matrices where $\mathbf{A} \in \mathbb{C}^{D \times N}$, $\mathbf{B} \in \mathbb{C}^{D \times D}$. Suppose \mathbf{B} is a diagonal matrix and $D \leq N$.

Taking Theorem 2 and replacing \mathbf{A} in that theorem with \mathbf{A}^\dagger , \mathbf{B} in that theorem with \mathbf{B} , and \mathbf{C} in that theorem with \mathbf{A} gives

$$(\mathbf{A}^\dagger \mathbf{BA})_{i,j} = \sum_{k=1}^D A_{k,i}^* B_{k,k} A_{k,j}.$$

□

Corollary 3.1. Suppose one has a matrix $\mathbf{C} \in \mathbb{C}^{N \times D}$ and a diagonal matrix $\mathbf{B} \in \mathbb{C}^{D \times D}$.

Then, the matrix product $\mathbf{C}\mathbf{B}\mathbf{C}^\dagger$ can be expressed component-wise as

$$(\mathbf{C}\mathbf{B}\mathbf{C}^\dagger)_{i,j} = \sum_{k=1}^D C_{i,k} B_{k,k} C_{j,k}^*.$$

Proof. Take the result from Theorem 3 and substitute in \mathbf{C}^\dagger in for \mathbf{A} —in other words, let $\mathbf{A} = \mathbf{C}^\dagger$. After making that substitution, Corollary 3.1 follows from Theorem 3 since $A_{ij} = C_{ji}^*$. Additionally, \mathbf{C} will have dimensions $N \times D$ since $\mathbf{C} = \mathbf{A}^\dagger$ as $\mathbf{A} = \mathbf{C}^\dagger$. \square

Theorem 4. Suppose one has a matrix $\mathbf{A} \in \mathbb{C}^{D \times N}$ and a diagonal matrix $\mathbf{B} \in \mathbb{C}^{D \times D}$ where $D < N$. Suppose one has a matrix $\mathbf{A}' \in \mathbb{C}^{N \times N}$ and a diagonal matrix $\mathbf{B}' \in \mathbb{C}^{N \times N}$. Additionally, suppose that $A'_{ij} = A_{ij}$ for all $i, j \in \mathbb{Z}$ such that $(1 \leq i \leq D) \wedge (1 \leq j \leq N)$. Also suppose that $B'_{ij} = B_{ij}$ for all $i, j \in \mathbb{Z}$ such that $(1 \leq i \leq D) \wedge (1 \leq j \leq D)$, and $B'_{ij} = 0$ otherwise. Then, $\mathbf{A}^\dagger \mathbf{B} \mathbf{A} = [(\mathbf{A}')^\dagger] (\mathbf{B}') (\mathbf{A}')$.

Proof. Suppose one had the matrices \mathbf{A} , \mathbf{B} , \mathbf{A}' , and \mathbf{B}' that are as they are described in Theorem 4. Theorem 3 can be applied with matrices \mathbf{A} and \mathbf{B} , as well as with matrices \mathbf{A}' and \mathbf{B}' . This yields

$$(\mathbf{A}^\dagger \mathbf{B} \mathbf{A})_{i,j} = \sum_{k=1}^D A_{k,i}^* B_{k,k} A_{k,j}$$

and

$$\left([(\mathbf{A}')^\dagger] (\mathbf{B}') (\mathbf{A}') \right)_{i,j} = \sum_{k=1}^N (A'_{k,i})^* B'_{k,k} A'_{k,j}.$$

Since $B'_{k,k} = 0$ for $k \in \mathbb{Z}$ where $k > D$, the two summations shown above are equivalent.

Therefore, $\mathbf{A}^\dagger \mathbf{B} \mathbf{A} = [(\mathbf{A}')^\dagger] (\mathbf{B}') (\mathbf{A}')$. \square

Corollary 4.1. Suppose one has a matrix $\mathbf{C} \in \mathbb{C}^{N \times D}$ and a diagonal matrix $\mathbf{B} \in \mathbb{C}^{D \times D}$ where $D < N$. Suppose one has a matrix $\mathbf{C}' \in \mathbb{C}^{N \times N}$ and a diagonal matrix $\mathbf{B}' \in \mathbb{C}^{N \times N}$. Additionally, suppose that $C'_{ij} = C_{ij}$ for all $i, j \in \mathbb{Z}$ such that $(1 \leq i \leq N) \wedge (1 \leq j \leq D)$. Also suppose that $B'_{ij} = B_{ij}$ for all $i, j \in \mathbb{Z}$ such that $(1 \leq i \leq D) \wedge (1 \leq j \leq D)$, and $B'_{ij} = 0$ otherwise. Then, $\mathbf{C}\mathbf{B}\mathbf{C}^\dagger = (\mathbf{C}')(\mathbf{B}') [(\mathbf{C}')^\dagger]$.

Proof. Take the result from Theorem 4 and substitute in \mathbf{C}^\dagger in for \mathbf{A} —in other words, let $\mathbf{A} = \mathbf{C}^\dagger$. After making that substitution, Corollary 4.1 follows from Theorem 4. Additionally, \mathbf{C} will have dimensions $N \times D$ since $\mathbf{C} = \mathbf{A}^\dagger$ as $\mathbf{A} = \mathbf{C}^\dagger$. \square

Theorem 5. Suppose one has a matrix $\mathbf{A} \in \mathbb{C}^{M \times L}$, a diagonal matrix $\mathbf{B} \in \mathbb{C}^{L \times P}$, and a matrix $\mathbf{C} \in \mathbb{C}^{P \times N}$. Without changing the matrix product \mathbf{ABC} , the i^{th} column of \mathbf{A} , i^{th} diagonal element of \mathbf{B} , and i^{th} row of \mathbf{C} can be swapped together with the j^{th} column of \mathbf{A} , j^{th} diagonal element of \mathbf{B} , and j^{th} row of \mathbf{C} . Moreover, this “swapping” operation can be applied an arbitrary number of times without changing the matrix product \mathbf{ABC} .

Proof. In the equation given in Theorem 2, changing the order of addition in the summation does not affect the overall matrix product. It can be seen that changing the order of addition in the summation is equivalent to permuting the columns of \mathbf{A} , the diagonal entries of \mathbf{B} , and the rows of \mathbf{C} in such a way that the columns/diagonal entries/rows of those matrices are moved “together”. Specifically, if one swaps the i^{th} and j^{th} columns, diagonal entries, and rows of \mathbf{A} , \mathbf{B} , and \mathbf{C} together respectively, the overall product \mathbf{ABC} will not change. Moreover, because this “swapping” operation does not change the matrix product \mathbf{ABC} , this “swapping” operation can be applied an arbitrary number of times. \square

Theorem 6. Suppose one has diagonal matrices $\mathbf{A} \in \mathbb{C}^{M \times L}$ and $\mathbf{B} \in \mathbb{C}^{L \times N}$. Then, the matrix product \mathbf{AB} is defined element-wise as

$$(\mathbf{AB})_{i,j} = \begin{cases} A_{i,i}B_{i,i}, & \text{for } (i = j) \wedge [i, j \leq \min(M, N, L)] \\ 0, & \text{otherwise.} \end{cases}$$

Proof. Let \mathbf{A} and \mathbf{B} be diagonal matrices such that $\mathbf{A} \in \mathbb{C}^{M \times L}$, and $\mathbf{B} \in \mathbb{C}^{L \times N}$.

The matrix product \mathbf{AB} can be expressed as

$$(\mathbf{AB})_{i,j} = \sum_{k=1}^L A_{i,k}B_{k,j}.$$

Since \mathbf{A} and \mathbf{B} are diagonal matrices, the only time the term inside the summation shown above is non-zero is when $(i = k) \wedge (k = j)$. This can only be satisfied when $i = j$, and such can happen at most one time in the summation. In such a case, the summation evaluates to be $A_{i,i}B_{i,i}$.

Furthermore, since \mathbf{AB} has dimensions $M \times N$, $i = j$ can only happen for $(i = j) \wedge [i, j \leq \min(M, N)]$. Furthermore, letting $i = j$, in order for a $A_{i,i}B_{i,i}$ term to be reached, i must be less than or equal to L . This is because the summation shown earlier in this proof only goes up to $k = L$.

Therefore, in order $(\mathbf{AB})_{i,j}$ to be nonzero, the condition $(i = j) \wedge [i, j \leq \min(M, N, L)]$ must be met. In such a case, one obtains $A_{i,i}B_{i,i}$. Thus,

$$(\mathbf{AB})_{i,j} = \begin{cases} A_{i,i}B_{i,i}, & \text{for } (i = j) \wedge [i, j \leq \min(M, N, L)] \\ 0, & \text{otherwise.} \end{cases}$$

□

Appendix D

COSI Conference Paper

The paper on the next two pages was accepted to the Computational Optical Sensing and Imaging (COSI) 2023 conference. It is related to the work described in Chapter 8, although the work in the paper predates the results shown in that chapter (Chapter 8).

One thing to note is that the paper’s uses of the term “pointlike scatterer” in the last paragraph might not be correct from a semantic standpoint. Even though the simulated scatterer would look like a point, its size is larger than a wavelength—thus, it might not be correct to consider the scatterer to be “pointlike”.

SW-DORT: Imaging Through Scattering Media Using Synthetic Wavelengths with DORT

Michael Joseph Lee¹, Jipeng Sun², Oliver Cossairt²

¹ Department of Electrical and Computer Engineering, Northwestern University, Evanston, IL 60208 USA

² Department of Computer Science, Northwestern University, Evanston, IL 60208 USA

¹ michaellee2023@u.northwestern.edu

Abstract: In this paper, we proposed a robust approach to image through scattering media without explicitly modeling the aberrating media by applying synthetic wavelengths to the DORT method. © 2023 The Author(s)

Imaging through scattering media, such as biological tissues or turbid media, enables non-invasive diagnosis and monitoring in many fields including medicine, biology, and material sciences. However, modeling aberrating media can be challenging. In this paper, we propose a synthetic wavelength-based DORT (decomposition of the time-reversal operator) method to robustly image through scattering media without the need to model aberrating media.

DORT is an eigendecomposition of a matrix operator known as the time-reversal operator. In practice, DORT is performed by taking the singular value decomposition (SVD) of a transfer matrix relating the input signals at a set of transmitting transducers to the received signals at a set of receiving transducers. The information from DORT can be used in a variety of ways including selectively focusing energy on scatterers [1] and imaging [2]. In the case of “well-resolved” discrete pointlike scatterers, the right-singular vectors will take the form [2] [3]

$$v_i(\lambda) = \frac{\mathbf{g}_s^*(\vec{x}_i; \lambda)}{\|\mathbf{g}_s(\vec{x}_i; \lambda)\|} e^{j\phi_{svd,i}(\lambda)} \quad (1)$$

where $(\cdots)^*$ denotes complex conjugation. $\mathbf{g}_s(\vec{x}; \lambda)$ is a steering vector where the components are the Green’s functions going from the spatial light modulator (SLM) pixel outputs to the i -th scatterer. The $e^{j\phi_{svd,i}(\lambda)}$ term is an arbitrary phase factor that arises due to the non-uniqueness of the SVD.

Images can be obtained by numerically backpropagating right-singular vectors. However, this requires that one have a model of one’s system, something that one might not have when imaging through aberrating media. This work uses synthetic wavelengths to avoid having to explicitly model aberrating media—the resiliency of synthetic wavelengths to path length variations [4] allowed for imaging via backpropagation in this investigation.

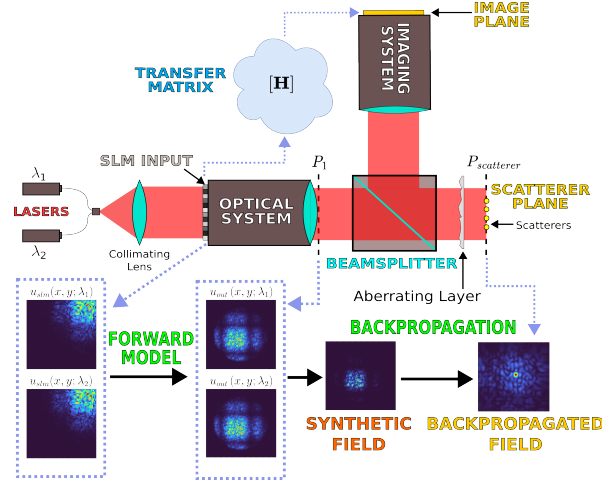


Fig. 1: Illustration of the Optical Setup and Computation Process of Proposed SW-DORT Model

The method in this investigation, henceforth referred to as “Synthetic Wavelength DORT” (SW-DORT), requires that one obtain two transfer matrices relating the fields at the SLM pixel outputs to the fields incident on the image sensor pixels. The two transfer matrices should be for two close but different wavelengths, and the wavelengths used depend on the desired synthetic wavelength. Various techniques [5] [6] exist for obtaining such transfer matrices.¹ One must also have a model for the optical path—excluding the aberrating layer, which is not

¹ [5] and [6] use the term “transmission matrix” instead of transfer matrix as those works operated in transmission mode.

modeled—going from the SLM output to the scatterer plane.

To perform SW-DORT, one takes SVDs of the two transfer matrices. This will yield two sets of right-singular vectors, one set per wavelength. The i -th right-singular vectors specify SLM output fields $u_{slm}(x, y; \lambda_1)$ and $u_{slm}(x, y; \lambda_2)$, which are fed into the system model. Using the model, the resulting fields $u_{out}(x, y; \lambda_1)$ and $u_{out}(x, y; \lambda_2)$ at plane P_1 in Fig. 1 are computed, and a synthetic field is generated at plane P_1 using the formula

$$u_{synth}(x, y; \Lambda) = u_{out}(x, y; \lambda_1) \odot u_{out}^*(x, y; \lambda_2), \quad (2)$$

where \odot denotes pointwise multiplication, $\lambda_1 < \lambda_2$, and $\Lambda = \frac{\lambda_1 \lambda_2}{|\lambda_1 - \lambda_2|}$ is the synthetic wavelength [4]. This synthetic field $u_{synth}(x, y; \Lambda)$ is then numerically backpropagated through *free space* from plane P_1 to plane $P_{scatterer}$. The wavelength of the synthetic field is the synthetic wavelength, and the aberrating layer *is not* modeled or simulated as the use of a synthetic wavelength allows one to ignore the aberrating layer.

In the experiments, the transfer matrix was obtained by simulating the entire optical path—from the SLM to the image plane, including the aberrating layer—using a modified version of Holotorch [7]. For the aberrating layer, a simple random thickness model was used: the aberrating layer was modeled as a random phase mask, with the phase shifts at each point being commensurate with the corresponding thickness [8].

Fig. 2 shows the backpropagated fields from imaging a pointlike scatterer using regular DORT methods and proposed SW-DORT. (a) and (b) show the results of backpropagating the regular (non-synthetic) fields at plane P_1 to plane $P_{scatterer}$ in Fig. 1.² It can be seen that the resulting images are aberrated and do not give a clear estimation of the pointlike scatterer's position. (c) shows the result of backpropagating the synthetic field using SW-DORT. In contrast to (a) and (b), the wave field for (c) appears unaffected by the aberrating layer due to the large magnitude of synthetic wavelength comparing with the disturbance. Note that the size of the focus spot in (c) can be further decreased by using a higher numerical aperture in the simulated setup and/or a smaller synthetic wavelength.

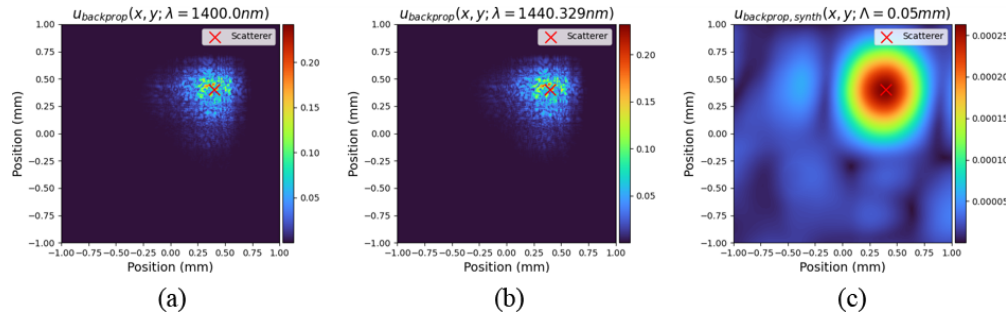


Fig. 2: The Comparison of the Backpropagated Field Results Using the Regular DORT Method and SW-DORT

References

1. Claire Prada, Sébastien Manneville, Dimitri Spoliansky, and Mathias Fink. Decomposition of the time reversal operator: Detection and selective focusing on two scatterers. *The Journal of the Acoustical Society of America*, 99(4):2067–2076, 1996.
2. Mehmet Emre Yavuz. *Time reversal based signal processing techniques for ultrawideband electromagnetic sensing in random media*. PhD thesis, The Ohio State University, 2007. Pages 35-44 and equation 3.31.
3. Mathias Fink and Claire Prada. *Detection and Imaging in Complex Media with the D.O.R.T. Method*. Springer Berlin Heidelberg, 2002. Equation 13.
4. Yicheng Wu, Fengqiang Li, Florian Wilhelmitz, Ashok Veeraraghavan, and Oliver Cossairt. Wished: Wavefront imaging sensor with high resolution and depth ranging. In *2020 IEEE International Conference on Computational Photography (ICCP)*, pages 1–10. IEEE, 2020.
5. Sébastien M Popoff, Geoffroy Lerosey, Rémi Carminati, Mathias Fink, Albert Claude Boccara, and Sylvain Gigan. Measuring the transmission matrix in optics: an approach to the study and control of light propagation in disordered media. *Physical review letters*, 104(10):100601, 2010.
6. Christopher A Metzler, Manoj K Sharma, Sudarshan Nagesh, Richard G Baraniuk, Oliver Cossairt, and Ashok Veeraraghavan. Coherent inverse scattering via transmission matrices: Efficient phase retrieval algorithms and a public dataset. In *2017 IEEE International Conference on Computational Photography (ICCP)*, pages 1–16. IEEE, 2017.
7. Florian Schifflers, Oliver Cossairt, and Nathan Matsuda. Holotorch. <https://github.com/facebookresearch/holotorch>, 2022. Commit cf1a80b3172684520b266cf03f9ba0163b5c1826.
8. Joseph W. Goodman. *Statistical Optics*. Wiley, 2nd edition, 2015. Sections 7.1.1 and 8.2.

²The backpropagation is done through free space, and the aberrating medium *is not* modeled or simulated.

Vita

Before attending Northwestern University, Michael Joseph S. Lee received a Bachelor of Science in Electrical Engineering from Rose-Hulman Institute of Technology in May of 2020. Afterwards, Michael began attending Northwestern University in January of 2022. He received his Master of Science in Electrical Engineering from Northwestern University in September of 2023.